THE ASTRONOMICAL JOURNAL VOLUME 107, NUMBER 1 JANUARY 1994

GALAXIES WITH SPECTRAL ENERGY DISTRIBUTIONS PEAKING NEAR 60 μm. II. OPTICAL BROADBAND PROPERTIES

CHARLENE ANNE HEISLER[1,2] AND J. PATRICIA VADER[3]

Department of Astronomy, Yale University, Box 6666, New Haven, Connecticut 06511
Electronic mail: cah@aaoepp.oz.au, vader@stsci.edu

Received 1993 April 5; revised 1993 August 23

ABSTRACT

In this paper (the second in a series), we present results of optical multicolor broadband CCD imaging of *IRAS* galaxies with spectral energy distributions peaking near 60 μm. As roughly two-thirds of the galaxies are previously unidentified in optical catalogues, this paper also serves as an optical catalogue for 60 μm peakers. All the 60 μm peakers are strong emission-line galaxies (Vader *et al.*) [AJ (1993), in press]. Our most striking result is that spiral structure is noticeably lacking among the 60 μm peakers, in view of the fact that *IRAS* galaxies and optically selected samples of emission-line galaxies are typically spirals. The majority of galaxies in our far-infrared (FIR) selected sample have a peculiar morphology (tidal tails, plumes, rings, shells, etc.) and the remaining galaxies have an amorphous appearance. This is reflected in a proposed morphological classification scheme consisting of four classes, ranging from amorphous to peculiar. Morphology class correlates well with optical colors and magnitudes; spectroscopic type; and FIR spectral indices. We interpret these correlations in terms of two scenarios, in which an interaction/merger is a key element that accounts for the observed morphology of the galaxies *and* the nuclear activity producing the "warm" FIR colors. Scenario A attributes the different optical morphologies of 60 μm peakers to differences in the precursor galaxies before the interaction, while scenario B attributes the morphological classification scheme to an evolutionary sequence that links galaxy morphology to nuclear activity. Both scenarios can explain the data equally well. The wide range in luminosity of our sample indicates that the short-lived phase of nuclear activity and 60 μm emission are not restricted to high luminosity galaxies.

1. INTRODUCTION

Observations at infrared wavelengths have been crucial for identifying galaxies undergoing large bursts of star formation, uncovering nuclear sources obscured by interstellar dust, and understanding the emission mechanisms present in active galactic nuclei. The Infrared Astronomical Satellite (*IRAS*), which surveyed more than 95% of the sky from 10 to 100 μm, has permitted the study of complete magnitude-limited samples of extragalactic far-infrared (FIR) sources.

Most of the galaxies detected by *IRAS* are normal disk galaxies that contain relatively large amounts of cool dust and gas. These normal disk galaxies have FIR spectral energy distributions that rise from 60 to 100 μm, with a substantial fraction of their FIR flux being emitted at wavelengths longer than the *IRAS* limit of ~120 μm (cf. Telesco & Harper 1980, Thronson & Bally 1987). The FIR spectral index $\alpha(60, 25\ \mu m)$, defined as $F_\nu \propto \nu^\alpha$, is generally quite steep ($\alpha \sim -2.5$) for the FIR detected disk galaxies, and results from dust emission in the disk, analogous to the cirrus emission from our Galaxy. Elliptical and S0 galaxies, on the other hand, were rarely detected by *IRAS* (de Jong *et al.* 1984). Due to the absence of massive disks of star formation, we expected optically selected early type (E and S0) galaxies to have relatively low FIR luminosities. Yet the strongest FIR sources associated with S0 galaxies are as powerful as the strongest FIR sources in late-type spiral galaxies (Dressel 1988). The long wavelength spectra of early and late-type normal galaxies have nearly identical shapes (Knapp *et al.* 1989), implying that the radiation has a common origin. Previously identified quasars detected by *IRAS* have spectral energy distributions that are much flatter or "warmer" than those of normal galaxies, i.e., they are strongly emitting at 12 and 25 μm (e.g., de Grijp *et al.* 1985, Miley *et al.* 1984, Neugebauer *et al.* 1984). The almost flat FIR spectral index $\alpha(60, 25\ \mu m)$ of quasars, ranging from −0.7 to −1.2 (Neugebauer *et al.* 1984), is attributed to a nonthermal component.

We have chosen to systematically study a complete sample of infrared-selected galaxies with FIR spectral indices intermediate between normal galaxies and quasars, and with spectral energy distributions (SEDs) peaking near 60 μm, hereafter referred to as 60PKs. We have defined a 60PK according to the following selection criteria: good quality detections at 25 and 60 μm in the second version of the *IRAS* Point Source Catalogue with flux density ratios

[1]Guest Investigator at Cerro Tololo Inter-American Observatory of the NOAO, operated by AURA, Inc. under contract with the NSF.
[2]Present address: Anglo–Australian Observatory, P. O. Box 296, Epping, N.S.W., Australia, 2121.
[3]Present address: Space Telescope Science Institute, 3700 San Martin Drive, Baltimore, MD, 21218.

 0004-6256/94/107(1)/35/32/$0.90

TABLE 1. Instrumental setup for observing program.

UT Dates (1)		Filters (2)	CCD Chip (3)	Gain (4)	Read Noise (5)	Scale (6)
Apr 15-19	1988	B, V, R, I	RCA #4	2.14	33.	0.495
Oct 4-6	1988	U, V	TI #1	2.23	7.09	0.494
Oct 7-10	1988	B, R, I	RCA #5	2.11	42.8	0.495
Mar 30	1989	U, B	TI #2	2.19	7.69	0.494
Mar 31-Apr 4	1989	U, B, V, R, I	TI #1	2.04	7.14	0.494
Oct 11-Oct 13	1990	U, B, V, R	TI #2	2.04	8.49	0.494

Notes to Table 1
Col.(1) Dates of Observing Run
Col.(2) Broad band filters used during observing run.
Col.(3) Type of Charged-Coupled Device used during observing run.
Col.(4) The number of photo-electrons per A/D unit as set by the electronic gain.
Col.(5) Readout noise (in units of e^-) of the CCD used for observing run.
Col.(6) Final scale of CCD in units of arcsecond/pixel.

$f_{60\ \mu m}/f_{100\ \mu m} > 1$ (including upper limits at 100 μm) and $4 > f_{60\ \mu m}/f_{25\ \mu m} > 1$ at a galactic latitude $|b| > 10°$. We consider only the extragalactic objects which satisfy the aforementioned criteria to be a 60PK (for a more detailed discussion please refer to Vader *et al.* 1993, Paper I). The scarcity of 60PKs (Paper I) suggests that they represent a transient phase of evolution for more common galaxies. This paper, the second in a series, reports on the optical broadband imaging and photometry program, and presents a catalogue of the optical broadband CCD images of 60PKs. In a paper to follow (Paper III), narrow-band Hα imaging clearly demonstrates the central concentration of activity. Paper III also contains a detailed statistical analysis which examines whether morphology or activity type is the fundamental parameter that produces the strongest segregation of the observed properties discussed in Papers I–III.

This study of the optical morphologies, colors, and magnitudes of 60PKs, all of whose optical spectra show strong emission lines characteristic of Seyfert and/or starburst galaxies, will significantly extend previous morphological studies of emission-line galaxies, most of which were based on optically selected samples (e.g., Adams 1977, Heckman *et al.* 1978, Simkin *et al.* 1980, Bothun *et al.* 1989, MacKenty 1990). The majority of 60PKs are previously unidentified in optical catalogues and most of these are too faint to classify on the POSS or ESO prints. The larger dynamic range and resolution of CCD detectors are better suited for our morphological study. Both low surface brightness features (too faint to be detected on POSS), and bright central features that may be situated in the "burnt out" portion on photographic plates can be detected on the same image. The telescope focal ratio and the pixel sizes of the CCDs used for our observations, yielded a resolution of approximately 16.67 arcsec mm^{-1}, which is four times better than that of the POSS/ESO sky surveys and allows for the detection of small scale morphological features. We present here the results of a very careful and detailed analysis of the optical images of 60PKs, including the application of various digital enhancement techniques.

This paper is organized in the following manner: CCD observations and data reductions are described in Sec. 2. Data analysis is given in Sec. 3. Our observational results are discussed in terms of a morphological sequence in Sec. 4, and are summarized in Sec. 5. On the basis of the morphological sequence of 60PKs, we propose two extreme, simple scenarios in which a tidal interaction event is crucial, and we examine the data in terms of these two scenarios in Sec. 6. We summarize conclusions in Sec. 7.

We adopt a Hubble constant $H_0 = 75$ km s^{-1} Mpc^{-1} and deceleration parameter $q_0 = 0.5$ throughout this series of papers.

2. THE DATA

2.1 Instrumental Setup

Optical imaging and photometry of 60PKs were obtained between 1988 April and 1990 October, using the 0.9 m telescope at CTIO with the Cassegrain Focus CCD Camera system, a RCA or Texas Instrument (TI) CCD, and broadband *U*, *B*, *V*, *R*, and *I* filters. Table 1 describes the instrumental setup of our optical imaging program. The TI and RCA CCDs, set at 2×2 and 1×1 pixel binning, respectively, provided a scale of approximately 0.5 arcsec/pixel for both CCDs. Compared to the RCA chip, the TI chip responds better in *U*, has a higher quantum efficiency, a much lower read out noise ($\sim$7 electrons for TI compared to $\sim$42 electrons for RCA), and a slightly smaller cosmic ray rate (by a factor of 2). The TI CCDs suffer very little fringing ($< 1\%$ of sky) in the *I* band, and none at shorter wavelengths, while *I*-band frames taken with the RCA CCDs display noticeable fringing, resulting in slightly higher errors for *I*-band photometry. The advantages of the TI CCD, and the long integration times required for our program objects in the *U* band, made the TI the ideal chip for our sample, and it was used whenever possible.

All the CCD frames were corrected for instrumental effects by subtracting an averaged bias frame. Long integration times were required for the faint galaxies in our sample, thus the CCDs were checked for possible hot spots using "dark" frames. These long dark exposures—typically

1800–3600 s—were taken for each instrumental setup, from which we typically found less than $5e^-$/h. Pixel-to-pixel variations in the sensitivity of the CCD were corrected with flatfield frames using sky flats and/or dome flats. A considerable red leak affects the dome flats (for *U* and *B* filters) at the 0.9 m telescope at CTIO (CTIO Observers Manual 1989). About 10 to 25 twilight sky frames were combined using IRAF to create a sky flat for the broadband *U* and *B* filters. Flatfielding of images was accomplished using these sky flats, yielding very flat sky backgrounds (variations $<0.6\%$). Dome flats (observations of a white spot in the dome illuminated by a quartz lamp, taken with a color balance filter that closely resembles the sky color), were sufficient for flat fielding the frames (variations $<1\%$) taken with broadband *V*, *R*, and *I* filters.

2.2 Observations

Images through optical broadband filters (*U,B,V,R,I*) were obtained for most 60PKs with $\delta<31°$. A detailed observing log including dates, exposure times, and filters used to observe each object is given in Table 2. We present a catalogue of our optical broadband CCD images of previously unidentified, and previously identified 60PKs in Figs. 1 [Plates 4–9] and 2 [Plates 10–14], respectively. We briefly discuss the individual galaxies in the Appendix. We were unable to observe 12 galaxies (IRAS 03445, 03578, 06457, 06097, 07314, 07329, 08321, 12474, 12540, 13449, 19315, 21169) from CTIO due to their northern declination. Fortunately four of these were previously well-studied galaxies (IRAS 06097≡Mkn 3; IRAS 06457≡Mkn 6; IRAS 08321≡Mkn 93; IRAS 12540≡Mkn 231), and are included in this study.

The FIR flux of a few 60PKs may have a significant contribution from a bright foreground star. Reflection rings due to a bright star contaminate the optical images of two objects: IRAS 13452 [Fig. 2(k)] and IRAS 16343. We have retained the former object in our sample because it is a relatively nearby previously identified galaxy, while we reject the latter because its faint optical counterpart is previously unidentified. Six additional previously unidentified sources are not considered in the analysis of this paper because they are too faint (even in deep exposure CCD frames) to be distinguishable from stars (IRAS 00260, 05209, 06047, 16442, 17096, 18526), and since optical spectra were not obtained for them, their nature (star or galaxy) remains unknown. Two of these (IRAS 06047 and IRAS 16442) appear to be blank fields on POSS prints. Our deep CCD exposures with broadband *V* and *R* filters have revealed a faint object for 06047, but nothing for 16442.

We retain a final sample of 46 galaxies for further analysis, half of which are previously unidentified in optical catalogues.

2.3 Photometric Calibration

After correcting for instrumental effects the frames were calibrated photometrically to account for observing time, airmass, and transformation to the standard Cousins broadband filter system (1967a,b). Instrumental magnitudes of standard stars were determined by summing the sky-subtracted intensity in concentric circular apertures of increasing radii centered on the star. Photometric standard stars from lists of Graham (1982) and Landolt (1983) were used to derive transformations from the instrumental to the standard system of Cousins. Transformation relations were defined for each night using between 10 and 18 standard stars per night.

A least-squares fitting routine was used to solve for coefficients in equations of the general form

$$M_{\lambda_0}-C_2 m_{\lambda_0}=C_0+C_1(M_{\lambda_0}-M_{\lambda_1}), \quad (1)$$

$$(M_{\lambda_0}-M_{\lambda_1})=D_0+D_1(m_{\lambda_0}-m_{\lambda_1}), \quad (2)$$

where λ refers to the wavelength band of the observations, i.e., *U,B,V,R,I*; upper-case letters M_{λ_0} and M_{λ_1} denote the magnitude in the standard Cousins photometric system; lower-case letters m_{λ_0} and m_{λ_1} denote the instrumental magnitudes corrected for exposure time and extinction due to airmass as given in Eq. (3); C_0 and D_0 denote the zero point for the best fitting line; C_1 and D_1 are the corresponding slopes; $(M_{\lambda_0}-M_{\lambda_1})$ is the standard Cousins photometric color term for the transformation

$$m_{\lambda_0}=2.5\log t_0-K_{\lambda_0}\chi_0-2.5\log I_{\lambda_0}+23.5, \quad (3)$$

where m_{λ_0} is the instrumental magnitude; t_0 is the exposure time; K_{λ_0} is the extinction coefficient; χ_0 is the airmass; I_{λ_0} is the sum of the pixel intensity.

When performing a least-squares fit on Eq. (1) the constant C_2 is initially set to one. For those cases where a least-squares fit gave a value close to zero for C_1 and a very poor correlation coefficient, the constant C_1 is set to zero and a value for C_2 (which is the slope in these cases) is then determined by a least-squares fit. Errors for the *B*, *V*, *R*, and *I* magnitudes and colors are typically less than 0.05 mag, while *U* magnitudes have slightly larger errors of 0.08 mag. The reader may refer to Heisler (1991) for a more detailed listing of the specific transformation relations for each night of observing, along with the coefficients for the zero points and slopes, and their associated errors and rms of the fit.

3. DATA ANALYSIS

3.1 Optical Morphology

3.1.1 Image enhancement

Several image enhancement techniques (unsharp masking and two-color mapping) were applied to our data to study the morphology of 60PKs. The basic idea behind the procedure of unsharp masking is to remove the large-scale brightness distribution to uncover small-scale light variations (Malin 1977; Schweizer & Ford 1985). The technique briefly outlined below has been used successfully by us (Heisler *et al.* 1989a,b,c) and others (e.g., Malin & Carter 1983; Veron-Cetty & Veron 1988; Ebneter *et al.* 1988) to reveal low surface brightness features (e.g., shells,

TABLE 2. Observing log.

IRAS (1)	OTHER NAMES (2)	U (3)	B (4)	V (5)	R (6)	I (7)
00160 − 0719		10/11/90, 1800s	10/08/88, 300s		10/08/88, 200s	
00198 − 7926		10/04/88, 3600s	10/07/88, 3600s	10/04/88, 900s	10/07/88, 1100s	
00260 − 7315		10/10/88, 2700s		10/10/88, 1800s		
00344 − 3349	ESO 350-IG38	10/06/88, 900s	10/08/88, 3x600s	10/09/88, 3x450s	10/08/88, 3x360s	10/09/88, 3x300s
00521 − 7054		10/05/88, 3600s	10/07/88, 1800s	10/05/88, 1800s	10/07/88, 600s	10/09/88, 720s
01053 + 2147		10/12/90, 3200s	10/12/90, 1600s	10/13/90, 1200s	10/10/88, 1200s	
01072 − 0348		10/06/88, 3x2000s	10/10/88, 1800s	10/06/88, 3x450s	10/08/88, 3x600s	10/09/88, 3x720s
01413 + 0205	MKN 573, M+00-05-033	10/11/90, 1200s	10/10/88, 3x300s	10/09/88, 3x240s	10/10/88, 3x240s	10/09/88, 3x240s
01475 − 0740		10/04/88, 1800s	10/07/88, 3600s	10/04/88, 900s	10/07/88, 1200s	10/09/88, 1200s
02304 + 0012	UGC 2024	10/11/90, 2100s	10/08/88, 1800s	10/09/88, 3x160s	10/08/88, 720s	10/09/88, 3x180s
02530 + 0012		10/12/90, 2400s	10/12/90, 3x600s	10/13/90, 900s	10/10/88, 900s	
03106 − 0254		10/11/90, 1800s	10/10/88, 900s	10/13/90, 600s	10/10/88, 600s	
03344 − 2103	NGC 1377, ESO 548-IG51	10/06/88, 3000s	10/08/88, 1200s	10/06/88, 900s	10/08/88, 450s	10/09/88, 500s
04259 − 0440		04/02/89, 2200s	04/02/89, 1200s	10/13/90, 600s	10/10/88, 700s	10/10/88, 600s
04385 − 0828		10/04/88, 3600s	10/12/90, 900s	10/06/88, 300s	10/13/90, 600s	
05189 − 2524		04/01/89, 600s	04/01/89, 300s	10/13/90, 600s	10/13/90, 600s	
05209 − 0107*					10/10/88, 600s	10/10/88, 600s
05530 + 0323	II Zw 40	10/05/88, 1500s	10/07/88, 1500s	10/05/88, 3x300s	10/07/88, 600s	10/09/88, 1200s
05570 − 8123		10/11/90, 2100s	04/17/88, 3x600s	04/18/88, 3x450s	04/17/88, 3x450s	
06047 − 0546*				10/13/90, 1800s	10/13/90, 900s	
06488 + 2731	MCG+05-16-010	04/02/89, 2100s	03/30/89, 1800s	04/04/89, 3x300s	04/04/89, 300s	04/04/89, 300s
08007 − 6600		04/01/89, 2400s	04/01/89, 1500s	04/15/88, 1200s	04/15/88, 1200s	
08014 + 0515	MKN 1210, UGC 4203	04/01/89, 1200s	04/01/89, 450s	04/04/89, 3x240s	04/04/89, 3x240s	04/04/89, 3x180s
08170 − 1126		04/02/89, 1800s	04/02/89, 900s	04/16/88, 3x600s	04/16/88, 3x600s	
09497 − 0122	MKN 1239, M+00-25-026	03/30/89, 3x1800s	03/30/89, 3x600s	04/18/88, 4x200s		
10567 − 3323		04/02/89, 4000s	04/02/89, 2000s	04/15/88, 3x1000s	04/16/88, 3x1500s	04/19/88, 3x900s
13329 − 3402	ESO383-G35, MCG-6-30-15	03/30/89, 3x1800s	03/30/89, 600s	04/17/88, 3x240s	04/17/88, 3x240s	
13370 − 3123	NGC 5253, ESO 445-IG4	04/01/89, 3x300s	04/17/88, 3x180s	04/17/88, 3x180s	04/17/88, 3x180s	
13452 − 4155	ESO 325-IG22	04/01/89, 3x240s	04/18/88, 3x300s	04/18/88, 3x200s	04/19/88, 3x300s	04/19/88, 3x300s
13536 + 1836	MKN 463, UGC 8550	04/02/89, 1200s	04/02/89, 600s	04/18/88, 3x180s	04/03/89, 600s	04/03/89, 300s
14082 + 1347	CGCG Zwicky	03/30/89, 3600s	03/30/89, 1800s	04/03/89, 900s	04/03/89, 780s	04/03/89, 720s
14167 − 7236		04/01/89, 2400s	04/01/89, 1200s	04/15/88, 3x600s	04/16/88, 3x600s	04/19/88, 3x600s
15295 + 2414	3C321, PKS 15295	04/02/89, 2700s	04/02/89, 1200s	04/17/88, 3x300s	04/17/88, 3x300s	
16343 − 1023*			04/18/88, 3x450s	04/18/88, 3x450s	04/19/88, 3x300s	04/19/88, 3x300s
16380 − 8123	ESO 023-IG03	03/30/89, 1500s	03/30/89, 600s	04/16/88, 3x300s	04/16/88, 3x300s	04/19/88, 3x300s
16442 − 0930*				04/18/88, 3000s	04/19/88, 2100s	
17096 − 1524*			04/15/88, 3x600s	04/15/88, 3x600s	04/15/88, 3x500s	
18333 − 6528	ESO 103-G35	10/06/88, 3600s	10/07/88, 600s	10/06/88, 1800s	10/07/88, 600s	10/09/88, 3x300s
18526 − 2445*		04/01/89, 1800s	04/01/89, 600s	04/18/88, 3x180s		
19245 − 4140	ESO338-IG04, Tololo19245	04/02/89, 1000s	10/08/88, 3x500s	10/10/88, 3x450s	04/17/88,600s	10/10/88, 3x300s
19370 − 0131		10/04/88, 2000s	10/07/88, 2000s	10/04/88, 1200s	10/07/88, 600s	10/09/88, 1200s
20210 + 1121		10/06/88, 2400s	10/08/88, 900s	10/06/88, 900s	10/08/88, 3x300s	
20253 − 8152		10/05/88, 3600s	10/07/88, 2400s	10/05/88, 1200s	10/07/88, 900s	10/09/88, 600s
20460 + 1915		10/11/90, 3600s	10/11/90, 1500s	10/13/90, 1200s	10/12/90, 900s	10/10/86,
20481 − 5715	IC 5063, PKS20481	10/05/88, 1800s	10/08/88, 3x600s	10/05/88, 900s	10/08/88, 3x300s	10/10/88, 3x450s
21062 + 1752		10/12/90, 2100s	10/08/88, 900s	10/09/88, 600s	10/08/88, 2x600s	10/09/88, 600s
23060 + 0505		10/11/90, 3600s	10/11/90, 2400s	10/13/90, 1200s	10/13/90, 1200s	
23446 + 1519	MCG+02-60-017	10/12/90, 1800s	10/08/88, 450s	10/09/88, 300s	10/08/88,3x300s	10/09/88, 300s
23547 − 1914		10/12/90, 2700s	10/12/90, 900s	10/13/90, 1200s	10/13/90, 900s	

Notes to Table 2

Col. (1) IRAS Name - an * denotes those galaxies that are not considered in the analysis of this paper because we are uncertain as to the nature (star or galaxy) of IRAS source, due to lack of spectra and/or the sources have stellar-like light profiles on CCD images.

Col. (2) Other names for previously catalogued galaxies.

Col. (3) - (6) Date (month/day/year), exposure time (in seconds) of images taken with broad band filters: U, B, V, R, and I, respectively.

ripples, dust features) that are normally hidden by the strong intensity gradient of the galaxy itself.

We take the following steps when constructing an unsharp masked image. First, the original CCD frame is Gaussian smoothed by convolving the image with a Gaussian kernel having a circular cross section and a Gaussian profile with values of sigma ranging from 3 to 10 pixels. This procedure in essence creates an "out-of-focus" mask. We next divide the original frame by this mask to produce an unsharp masked image. A two-color map ($B-R$ and/or $B-I$ and/or $U-V$) is constructed in a similar manner, following a technique tantamount to that described by Sparks *et al.* (1985). Regions of enhanced star formation have very blue colors relative to the background galaxy and appear as relatively darker regions on our grey-scale images of the two-color processed CCD frame. Dust lanes and patches have red colors and appear as lighter regions compared to the background galaxy on two-color maps. We display digitally enhanced images (i.e., unsharp masked images, and two-color maps) for some previously unidentified and identified 60PKs in Figs. 3 [Plates 15 and 16] and 4 [Plates 17–19], respectively. We use these digitally enhanced images in conjunction with the original CCD frames to morphologically classify the 60PKs, as discussed in Sec. *3.1.2*.

3.1.2 Morphological classification

Sorting galaxies by morphology can be an ambiguous and complicated task. Morphological classification depends on many parameters: the bandpass of the filter used for the observation (effective wavelength and bandwidth), the resolution of the pixel elements of the CCDs, the seeing conditions at the time of the observations, and the distance of the object. A striking result is the absence of prominent spiral structure in 60PKs. Only four galaxies display spiral structure (IRAS 21062, 02304, 08321, 23446), and all of these also possess a faint outer envelope extending beyond the spiral arms that is not a common characteristic of normal spiral galaxies. Most of the 60PKs have smooth global light distributions with rather inconspicuous nuclei compared to optically selected Seyferts. We refer to the galaxies with smooth global light distributions as amorphous and discuss them in more detail below. The remaining objects appear disturbed or peculiar—they have multiple nuclei, tails, "jets," plumes, etc. Digital masking techniques enhance these features, and more importantly, uncover low surface brightness features which are not obvious on the original CCD images of many of the otherwise featureless amorphous galaxies.

Two-thirds of 60PKs have optical spectra characteristic of Seyfert galaxies (Paper I). In general, Seyfert galaxies have many features that are not well described by the Hubble sequence. The first attempts to fit Seyferts into the standard morphological classification system revealed that Seyfert 2 galaxies tended to have spiral structure, while Seyfert 1 galaxies were more likely to have an amorphous form, typical of S0 galaxies (Khachikian & Weedman 1971). A generalized description of Seyfert galaxies proposed by Simkin *et al.* (1980), and based on the morphological description given by Khachikian & Weedman (1971), involved three components: an inner disk; an intermediate envelope, bar, or lens; and a faint outer envelope or bar. The distinction between these three components was first noted by Sandage (1961) for the active galaxy NGC 1068. The amorphous class was originally defined by Sandage & Brucato (1979) as follows: a smooth unresolved, high surface brightness background of light with no spiral structure evident, sometimes with embedded star formation, dust lanes or irregular dust patches, emission lines in optical spectra, and a strong underlying A star absorption spectrum. We take from above the elements appropriate for our sample and adopt the following simple classification scheme.

Class 0. Amorphous: a galaxy with a smooth global light distribution; totally featureless morphology.

Class I. Amorphous+Features: a galaxy whose main body is amorphous, upon which low surface brightness features (shells, rings, tails, dust lanes) are superposed.

Class II. Spiral: a galaxy with prominent spiral arms.

Class III. Peculiar: a galaxy with prominent peculiar features such as multiple nuclei, tails, plumes, jets, etc.

The basic characteristics of the amorphous classes are the same as those specified by Sandage & Brucato (1979), except that we distinguish two categories of amorphous galaxies: class 0 and class I. Class 0 galaxies appear completely featureless (even on digitally enhanced images), while class I galaxies contain hot spots of star formation, and/or low surface brightness features such as dust lanes or patches, and/or shells or faint rings. IRAS 09497 [Fig. 2(h)] is a prototype class 0 galaxy, while IRAS 14082 [Fig. 2(m)] typifies a class I galaxy in our sample. The main bodies of both class 0 and class I 60PKs possess a smooth global light distribution on the original CCD frames, and we distinguish between these two classes using digitally enhanced frames that clearly reveal peculiar features for the class I galaxies [e.g., Fig. 4(l)]. Both of the amorphous classes (0 and I) may contain S0 and/or elliptical galaxies, as emphasized by Gallagher & Hunter (1989) in the case of optically selected amorphous galaxies. In fact, some of the previously identified galaxies in our sample are labeled as all three types by various authors (e.g., Sandage & Brucato (1979) classify NGC 5253 as a prototype amorphous galaxy, while Tully (1988) classifies it as an E/S0). In this paper we make no attempt to distinguish between amorphous, elliptical, or lenticular galaxies, and we group them all into the amorphous category. In a subsequent paper (Paper IV) we investigate whether the amorphous galaxies (classes 0 and I) are disk-dominated or bulge-dominated systems, through a detailed examination of the axial ratio distributions, degree of light concentration, and surface brightness profiles (cf. Heisler 1991). The class II morphology is self-explanatory. An example is IRAS 02304 [Fig. 15(f)], one of the four spiral galaxies in our sample, all of which are characterized by a faint outer envelope. These faint outer envelopes are similar to lenses described by Kormendy (1979), although such lenses preferentially occur in later-type barred galaxies that contain a nearly complete central ring encircling the bar (Sandage & Bru-

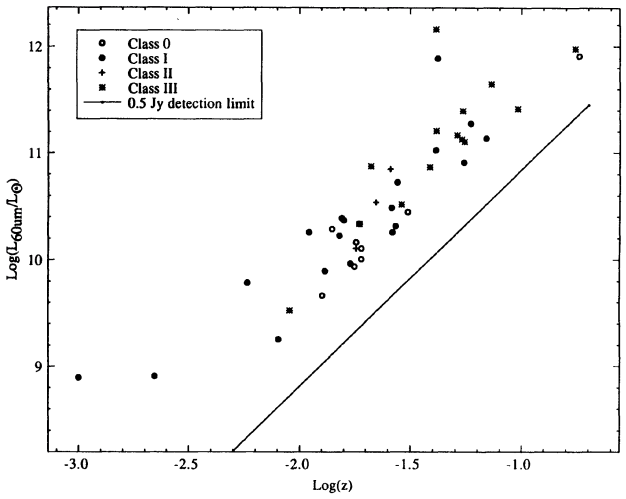

FIG. 5. Redshift vs 60 μm luminosity (in units of solar luminosity). The symbols have the following meaning: open circles—class 0; filled circles—class I; plus signs—class II; stars—class III. The solid line represents the detection limit of 0.5 Jy at 60 μm.

cato 1979). Only one of the spirals in our sample (IRAS 23446) contains a bar. Class III galaxies have obvious peculiar features that are clearly visible on CCD frames and a main body that appears chaotic (bright knots, multiple nuclei, dust patches). The major distinctions between class III and class I are the surface brightness of the peculiar features, and the light distribution of the main body of the galaxy. An example of class III is IRAS 00198 [Figs. 1(b) and 15(a)] which has multiple nuclei, tidal extensions, and an overall chaotic appearance.

Morphological classification depends on the limiting sensitivity of the observations and the resolution. The ability to resolve features on our CCD images is a function of seeing conditions and distance of the object. The average seeing for the morphological classes ranges from 1.2 ± 0.2 to 1.4 ± 0.2 arcsec, so that there is no systematic dependence of morphological classification on seeing. We examine the possibility that distance affects our classification scheme by investigating the plot of redshift vs 60 μm luminosity (Fig. 5). In Fig. 5 the symbols have the following meaning: open circles—class 0; filled circles—class I; plus signs—class II; stars—class III. The solid line represents the detection limit of 0.5 Jy at 60 μm. This diagram demonstrates that the lack of observed features in the class 0 60PKs is not a resolution problem due to distance, because we resolve features in other galaxies (classes I–III) over the range of redshifts covered by class 0 galaxies. The only possible exception being IRAS 20460, which has the highest redshift among the sample of 60PKs. Structure is just barely resolved in IRAS 23060, which has the second largest redshift among 60PKs. Similarly, the difference in classes I and III is not due to a bias in redshift, because the redshift range is similar for both classes. Given that the four morphology classes are not segregated with respect to redshift, we conclude that the morphological classification scheme we have adopted for the 60PKs is not resolution biased due to distance.

The classification scheme may be biased as a result of the bandpass through which the image is observed. For example, a blue filter will be sensitive to young star formation, while a red filter will be more sensitive to the older underlying stellar population. CCD frames and digitally enhanced images (masked and two-color frames), have been carefully examined for each galaxy over a wide range in optical wavelengths (U, B, V, R, and I). Our morphological classes may not hold up in other passbands (i.e., near IR, UV, x-ray, etc.), but in the optical range considered here the classification scheme is valid.

We have confirmed that our classification scheme does not show a bias with respect to optical bandpass or resolution (due to distance or seeing). Table 3 lists the morphological class assigned to each galaxy.

3.2 Optical Colors and Magnitudes

3.2.1 Integrated colors

Integrated magnitudes and colors were determined from curves of growth. The sum of sky-subtracted pixel intensities in concentric circular apertures centered on the galaxy were calculated as a function of aperture radii. The total magnitude was determined from the asymptotic limit of the curves of growth. The galaxies in this sample have a small angular diameter relative to the size of the CCD (with the exception of IRAS 13370 and 03344), thus determination of sky is relatively straightforward. A modal value for the local sky level is calculated within an annulus centered on the galaxy. The inner radius of the sky annulus is chosen such that contamination due to light from the galaxy is negligible. Table 4 gives the integrated apparent magnitudes and colors.

3.2.2 Nuclear and annular colors

Our sample of 60PKs contains galaxies that span a large range in luminosity and sizes. We define the "nucleus" as the central region containing 1/4 of the total blue light. This blue quarter-light radius, $r_{1/4}$, is the aperture size used for determining the "nuclear" magnitudes and colors (Table 4). A nuclear magnitude is not given for six galaxies because their blue quarter-light radius is within their seeing disk as measured from the full width at half-maximum (FWHM) of several stars on the CCD frames. One-third of our sample of 60PKs consist of multiple galaxies or nuclei. The nuclear magnitudes of these multiple nuclei 60PKs are measured within small apertures (Table 5).

Annular magnitudes and UBV colors were derived for the outer region of the galaxies (disk or faint outer envelope). For all 60PKs, we chose an annulus with an inner radius equal to the blue quarter-light radius and an outer radius that contains the entire galaxy as determined by curves of growth. Annular colors could not be calculated for those galaxies whose blue quarter-light radius is within their seeing disk or 60PKs which consist of closely separated multiple nuclei.

TABLE 3. Morphological classification of 60 μm peakers.

IRAS NAME (1)	REDSHIFT (2)	MORPH. (3)	COMMENTS (4)
00160–0719	0.018	0	featureless, smooth
00198–7926	0.0728	III	mncl, tails
00260-7315	*	rejected	stellar radial profile
00344–3349	0.0210	III	mncl , tails
00521–7054	0.0689	I	asymmetrical isophotes
01053+2147	0.0550	III	mncl, tails
01072–0348	0.0546	I	shells
01413+0205	0.0170	I	ring
01475–0740	0.0177	0	many fuzzy patches
02304+0012	0.0221	II	knots, faint outer envelope
02530+0211	0.0276	I	shells
03106–0254	0.0272	I	ring caused by inner dust
03344–2103	0.0058	I	dust lane along minor axis
04259–0440	0.0155	I	shells
04385–0828	0.0151	I	knots, faint inner arms
05189–2524	0.0419	I	tails, off-centre nucleus
05209–0107	*	rejected	stellar radial profile
05530+0323	0.0022	I	mncl, tails, knots
05570–8123	0.0126	0	featureless, smooth
06047–0546	*	rejected	stellar radial profile
06097+7103	0.014	0	1
06457+7429	0.019	0	1
06488+2731	0.0410	I	shells
07314+6207	0.1207	rejected	no CCD images
08007–6600	0.0412	III	mncl, tails
08014+0515	0.013	I	shells
08170-1126	0.0535	III	mncl, tails
08321+6624	0.0180	II	2, faint outer envelope
09497–0122	0.019	0	featureless
10567–3323	0.0586	I	3 knots in tidal extension
12474+4345	0.0622	rejected	no CCD images
12540+5708	0.041	III	3
13329–3402	0.008	I	disk? on masked frame
13370–3123	0.001	I	dust lanes, patches, knots
13449+3511	0.0539	rejected	no CCD images
13452–4155	0.0386	III	tail
13536+1836	0.051	III	mncl, tails
14082+1347	0.0158	I	shells
14167–7236	0.0261	I	tails, off-centre nucleus
15295+2414	0.096	III	DG, tail
16343–1023	*	rejected	stellar radial profile
16380–8120	0.0290	III	DG, disk+dwarf
16442–0930	*	rejected	blank field
17096+1524	*	rejected	stellar radial profile
18333–6528	0.013	0	featureless, smooth
18526–2445	*	rejected	stellar radial profile
19245–4140	0.0090	III	mncl, tails
19370–0131	0.0186	III	elongated due to 2nd nucl
20210+1121	0.0541	III	ring, DG
20253–8152	0.0309	0	featureless, smooth
20460+1925	0.1810	0	featureless, smooth
20481–5715	0.011	I	mncl, dust, central knots
21062+1752	*	II	spiral, faint outer envelope
23060+0505	0.1738	III	tails, central knots
23446+1519	0.0258	II	bar, faint outer envelope
23547+1914	0.0263	I	shells

TABLE 3. (continued)

Notes to Table 3

Col.(1) IRAS Name

Col.(2) Redshift based on optical spectroscopy (paper I). An * in this column indicates that redshift is unknown, so their nature (star versus galaxy) is unclear. All these objects (with the exception of IRAS 21062) are too faint for morphological classification using our deep exposure CCD frames, and are rejected from analysis in this paper.

Col.(3) Optical Morphological Class:

Class 0	Amorphous
Class I	Amorphous + Features
Class II	Spirals
Class III	Peculiar

Col.(4) Comments regarding morphology. Abbreviations have the following meaning:

DG	Double Galaxy
mncl	multiple nuclei
dust	dust patches or dust lanes
knots	bright knots (relatively blue in colour)
ring	complete or partial ring encircling main body of galaxy
no CCD images	optical CCD images were not obtained of galaxy

A number in this column refers to the reference used to classify morphology of previously identified galaxy when a CCD image was not obtained by us:

1. Neff *et al.* 1990, and references therein
2. Mazzarella and Balzano 1986 and references therein
3. Sanders *et al.* 1988 a,b and references therein

3.2.3 Foreground extinction and reddening corrections

The colors and magnitudes were corrected for foreground extinction using maps of Burstein & Heiles (1982). As the redshifts are relatively small ($z<0.18$) we assumed a linear dependence of redshift and used k corrections based on tabulations by Pence (1976). This yields the following equation for the final corrected colors:

$$(M_{\lambda_1}-M_{\lambda_2})_{\rm corr}=(M_{\lambda_1}-M_{\lambda_2})_0-E(M_{\lambda_1}-M_{\lambda_2}) -(k_{M_{\lambda_1}-M_{\lambda_2}})z, \quad (4)$$

where $(M_{\lambda_1}-M_{\lambda_2})_{\rm corr}$ is the final reddening and redshift corrected color; $(M_{\lambda_1}-M_{\lambda_2})_0$ is the observed color; $E(M_{\lambda_1}-M_{\lambda_2})$ is the reddening; z is the redshift, and $k_{M_{\lambda_1}-M_{\lambda_2}}$ is the k-correction coefficient. We adopt $E(U-B)=0.78E(B-V)$. The k-correction coefficients, derived as a function of intrinsic color rather than morphological type from Pence's (1976) data, are approximated by

$$k_B=5.96(B-V)_c-0.64, \quad (5a)$$

$$k_{B-V}=2.44(B-V)_c+0.74, \quad (5b)$$

$$k_{U-B}=-0.96(U-B)_c-0.38 \quad (5c)$$

for redshifts $z<0.2$, and extinction-corrected colors $(B-V)_c$ and $(U-B)_c$.

Table 6 lists the absolute blue magnitudes and the $(U-B)_0$ and $(B-V)_0$ colors corrected for galactic reddening $E(B-V)$ and redshift for: the total galaxy; the nucleus; and the outer annular region.

3.3 Blue Surface Brightness

We calculate the effective blue surface brightness—defined as the average surface brightness through a blue broadband filter within the half-light radius (as specified by curves of growth), corrected for foreground extinction and redshift—according to

$$\langle {\rm SBe}\rangle = m_B+5\log(r_e)+2.5\log(2\pi)-A_B-k_Bz, \quad (6)$$

where m_B is the apparent total blue magnitude, r_e the half-light radius, A_B the extinction in $B[A_B=4.1E(B-V)]$, and k_B the k correction as given by Eq. (5a). The half-light radii and corresponding effective blue surface brightness corrected for galactic extinction and redshift are given in Table 6.

The nuclear surface brightness $\langle {\rm SB}_{1/4}\rangle$ is calculated in a similar manner using the quarter-light radius, $r_{1/4}$, instead of r_e. The quarter-light radius and corresponding nuclear blue surface brightness are also listed in Table 6.

4. RESULTS

4.1 Morphology

An unusual aspect of this sample is the apparent lack of spiral structure (cf. Table 7). The near absence of prominent spiral structure among 60PKs is in sharp contrast to the preponderance of spirals ($>65\%$) in FIR-selected galaxy samples (e.g., Armus *et al.* 1987) and in optically selected samples of emission-line galaxies (e.g., Adams 1977, Bothun *et al.* 1989). The faint outer envelope, characteristic of the four spirals in our sample, is uncommon in "normal" spirals [i.e., non-(r)-type spirals], supposedly due to the fact that the arms generally obliterate the boundary of

TABLE 4. Apparent optical magnitudes and colors.

IRAS NAME	m_b	$(u-b)_{tot}$	$(b-v)_{tot}$	$(v-r)_{tot}$	$(r-i)_{tot}$	$(u-b)_{nuc}$	$(b-v)_{nuc}$	$(v-r)_{nuc}$
(1)	(2)	(3)	(4)	(5)	(6)	(7)	(8)	(9)
00160–0719	14.77	0.30	—	—	0.60	0.59	1.10	0.42
00198–7926	16.30	−0.33	0.82	0.46	—	0.33	1.03	0.26
00344–3349[a]	14.56	−0.77	0.53	0.29	0.26	—	—	—
00521–7054	17.18	0.08	1.02	0.43	—	0.57	1.02	0.72
01053+2147	16.76	0.04	0.93	0.30	—	0.08	0.90	0.31
01072–0348	16.59	0.00	1.08	0.18	0.69	0.48	1.21	0.14
01413+0205	14.22	0.21	1.09	0.46	0.55	0.38	0.71	1.27
01475–0740	16.68	0.04	0.92	0.59	0.66	0.36	1.24	0.29
02304+0012	14.92	0.20	1.04	0.28	0.34	0.51	1.24	1.08
02530+0211	16.90	0.15	1.23	0.22	—	0.24	1.18	0.58
03106–0254	15.26	0.13	1.25	0.15	—	0.51	1.31	0.34
03344–2103	13.64	0.44	0.81	0.70	0.45	0.98	0.84	0.72
04259–0440	15.81	0.15	0.86	0.43	0.76	0.15	0.89	0.46
04385–0828	15.73	0.45	0.87	0.59	—	0.94	1.21	0.74
05189–2524	15.25	0.22	0.80	0.46	—	−0.30	1.13	0.53
05530+0323[b]	16.08	0.38	1.58	0.39	0.60	—	—	—
05570–8123	16.46	0.09	0.95	0.62	—	0.20	0.50	—
06097+7103*	14.49	0.10	1.15	—	—	—	—	—
06457+7429*	15.16	0.18	0.97	—	—	—	—	—
06488+2731	15.02	0.40	0.92	0.54	0.50	0.10	0.93	0.76
08007–6600[a]	16.18	−0.39	0.65	0.52	—	—	—	—
08014+0515	14.52	−0.04	0.86	0.47	0.49	−0.62	0.85	0.66
08170–1126[a]	16.96	−0.41	0.77	0.25	—	—	—	—
08321+6624*	15.7	—	—	—	—	—	—	—
09497–0122[c]	15.19	−0.15	0.79	—	—	—	—	—
10567–3323	17.86	−0.19	0.57	0.33	0.53	−0.34	0.51	0.61
12540+5708*	14.68	0.15	0.84	—	—	—	—	—
13329–3402	14.40	0.35	0.95	0.87	—	0.95	1.06	0.62
13370–3123[b]	11.29	−0.33	0.49	0.67	—	—	—	—
13452–4155[a]	15.60	0.21	0.61	0.80	0.65	—	—	—
13536+1836[a]	15.01	−0.18	0.89	0.34	0.57	—	—	—
14082+1347	15.44	0.29	0.84	0.55	0.57	0.16	0.94	0.63
14167–7236	16.35	0.33	0.94	0.49	0.77	0.07	0.70	0.91
15295+2414[a]	16.71	0.03	0.99	0.58	—	—	—	—
16380–8120[a]	15.91	0.29	1.06	0.70	0.75	—	—	—
18333–6528	14.92	0.40	1.07	0.57	0.62	0.93	1.21	0.68
19245–4140[a]	14.44	−0.56	0.55	0.15	0.02	—	—	—
19370–0131[c]	17.82	0.11	1.40	0.67	0.89	—	—	—
20210+1121[c]	15.79	0.04	0.50	0.54	—	—	—	—
20253–8152[c]	17.50	0.02	0.64	0.94	0.63	—	—	—
20460+1925[c]	18.21	0.15	1.25	0.74	—	—	—	—
20481–5715	13.62	0.28	1.13	0.72	0.59	0.56	1.37	0.41
21062+1752	17.04	−0.15	0.53	0.87	0.52	0.14	0.84	0.71
23060+0505[c]	17.73	−0.04	1.16	0.56	—	—	—	—
23446+1519	15.35	0.20	0.98	0.37	0.68	0.20	0.72	0.41
23547–1914	17.00	0.08	1.09	0.66	—	0.58	1.14	0.73

Notes to Table 4

Col.(1) IRAS Name. The magnitude was taken from Veron-Cetty and Veron (1987) for those galaxies denoted by a superscript *.
A superscript letter following the IRAS name has the following meaning:

a. These 60PKs consist of multiple nuclei or double galaxies. Nuclear magnitudes were not measured within the blue quarter-light radius. Instead, the 'nuclear' magnitudes and colours are measured within small apertures that are centered on the individual components (Table 5).

b. Numerous bright central knots prevented the determination of a precise centre, thus the quarter-light radius and corresponding magnitudes and colours can not be measured.

c. The blue quarter-light radius is within seeing disk, thus we were unable to determine the corresponding nuclear magnitudes and colours.

Col.(2) Apparent integrated optical blue magnitude.

Col.(3)-(6) Apparent (u-b), (b-v), (v-r) and (r-i) integrated colours, respectively.

Col.(7)-(9) Apparent (u-b), (b-v), (v-r) nuclear colours, respectively, as measured within the blue quarter-light radius.

TABLE 5. Separation and colors of multiple nuclei.

IRAS NAME	ANGULAR SEPARATION	LINEAR SEPARATION	Nucleus II / I	Aperture Size(")	m_b	(u - b)	(b - v)	(v - r)
(1)	(2)	(3)	(4)	(5)	(6)	(7)	(8)	(9)
00344-3349 n1-n2	3.26 arcsec	1.3 kpc	n1 / A	2.96	15.61	-0.80	0.43	0.28
			n2 / B	2.96	15.82	-1.16	0.81	0.32
00344-3349 n2-n3	3.16 arcsec	1.3 kpc	n3 / C	2.96	15.99	-1.07	0.85	-0.09
08007-6600	6.13 arcsec	5.0 kpc	n1 / A	3.96	16.79	-0.47	0.63	0.59
			n2 / B	1.98	18.00	-0.40	0.61	0.38
08170-1126	3.25 arcsec	3.4 kpc	n1 / A	2.96	17.46	-0.56	0.68	0.14
			n2 / B	1.98	19.26	*	1.05	0.31
13452-4155	7.55 arcsec	5.7 kpc	G1 / A	4.94	16.71	-0.03	0.64	0.56
			G2 / B	4.94	17.18	*	0.58	0.76
13536+1836	4.25 arcsec	4.2 kpc	n1 / A	2.48	16.93	-0.38	0.61	0.04
			n2 / B	2.48	16.86	-0.13	1.29	0.44
15295+2414	3.09 arcsec	5.9 kpc	n1 / A	2.48	17.89	0.01	1.20	0.60
			n2 / B	1.98	18.72	0.06	1.20	0.02
16380-8120	6.20 arcsec	3.5 kpc	G1 / A	4.46	17.23	0.53	1.24	0.78
			G2 / B	2.97	17.43	-0.02	0.78	0.65
19245-4140	3.04 arcsec	0.5 kpc	n1 / A	3.95	15.07	-0.70	0.48	---
			n2 / B	2.96	15.68	-0.67	0.47	---

Notes to Table 5

Col.(1) IRAS Name
Col.(2) Angular separation of nuclei or galaxies in arcseconds.
Col.(3) Linear projected seaparation of nuclei or galaxies in kiloparsecs.
Col.(4) Identification of nuclei in this paper II and in paper I, respectively.
Col.(5) Size of aperture (in arcseconds) within which magnitudes were measure.
Col.(6) Apparent blue magnitude within small aperture (size given in column 5) of each component.
Col.(7)-(9) Apparent colours of each component within aperture whose size is given in Col. 2. An * denotes a nuclear component that is very faint. Photometry in the U filter was unreliable for these nuclei, thus a (u-b) colour could not be determined.

the envelope (Sandage & Brucatto 1979). Faint outer envelopes have been observed in Seyfert galaxies (e.g., Sandage 1961, Burbidge *et al.* 1963, Adams 1977) and have been incorporated into the generalized morphological description proposed by Simkin *et al.* (1980). The existence of the faint outer envelope is consistent with numerical simulations involving the perturbation of self-gravitating disk galaxies by the tidal force of another galaxy. *N*-body simulations by Noguchi (1987, 1988a,b) demonstrate that prominent spiral structure develops within a faint envelope as a result of a tidal interaction. On the other hand, the fraction (18%) of 60PKs with an amorphous appearance (class 0) is similar to that found for the optically selected Seyferts studied by MacKenty (1990). Galaxies with peculiar features (classes I and III) dominate our sample. Three such galaxies (IRAS 01413, 03106, 20210) have rings surrounding the central nucleus. Rings of this type have been explained by either the dynamical response of a disk to a compact intruder, that generates an outward propagating kinematic density wave (cf. Athanassoula & Bosma 1985, and references therein); or alternatively, as the result of a gravitational perturbation due to an instability that produces a gas flow toward the nucleus and a concentration of gas into rings at Linblad resonances (cf. Simkin *et al.* 1980). Seven class I galaxies have bright arcs or shells surrounding the main body of the galaxy. Models which have been proposed to account for the properties of the shells can be divided into two classes according to whether the origin of the stars forming the shells is internal or external. Internal scenarios invoke either star formation in gas intrinsic to the galaxy (e.g., Fabian *et al.*, 1980, Williams & Christiansen 1985), or density waves in a thick disk population of dynamically cold stars induced by a tidal distortion caused by a weak interaction (e.g., Schombert & Wallin 1987, Thomson 1991). External scenarios invoke a merger event which gives rise to shells as the result of material from a companion galaxy (or even a whole galaxy itself) falling into a galaxy during a close passage (e.g., Schweizer 1980, Dupraz & Combes 1986, Hernquist & Quinn 1988, 1989). In either case (internal or external) a galactic encounter (be it a weak interaction or a full blown merger) is a crucial element to the formation of shells surrounding galaxies.

Our CCD imaging reveals that 12 class III galaxies contain multiple nuclei or double galaxies. Digital enhancement has further uncovered possible multiple nuclei in the centers of two class I galaxies (IRAS 05530 and 20481). These multiple nucleus galaxies are interesting in light of the ongoing controversy concerning the relationship between ultraluminous infrared galaxies and interactions and mergers (e.g., Joseph 1986), and the possible connection between nuclear activity and interactions (e.g., Heckman

et al. 1986; De Robertis 1985). It is difficult to ascertain the nature of bright condensations observed within many 60PKs based only on optical CCD images and optical spectroscopy. These bright components may be either giant H II regions belonging to the galaxy itself, or the nuclei of separate galaxies in the process of merging. Optical observations alone cannot distinguish between a galactic starburst nucleus and a giant extranuclear H II region. High resolution imaging in the near infrared may be useful, and even necessary for distinguishing between these alternatives (cf. Telesco *et al.* 1985; Joseph *et al.* 1988). For the time being, we retain the "peculiar" classification (class III) for the 60PKs that clearly show multiple nuclei on the original broadband optical images.

We adopt a morphology-based analysis, and examine the dependence of morphological class on nuclear-activity type, optical colors and magnitudes, FIR luminosities and flux ratios, $L_{60\ \mu m}/L_B$, for the 60PKs. The nuclear-activity type as derived from optical spectroscopy may be misleading for 60PKs due to the dust enshrouded nature of their nuclei. Several 60PKs that have Seyfert 2 nuclear activity (based on optical spectroscopy) have much broader lines (typical of Seyfert 1 or quasars) when viewed in polarized light (Miller & Goodrich 1990) or with near-infrared spectroscopy (Hines 1991). Thus, in this paper we adopt the morphology class as the fundamental parameter and investigate how observable properties depend on it. In Paper III of this series we examine the validity of such a morphology-based analysis using multivariate statistical tests. We do not include IRAS 20460 in the following calculations of the average properties of each morphological class, because its amorphous morphology may be attributed to the fact that it is the furthest object in our sample (Sec. *3.1.2*). This is the only dubious morphological classification for the 60PKs. Deeper exposures at higher resolution are required to rectify this case.

4.1.1 Optical nuclear activity

All of the galaxies in our FIR-selected sample for which optical spectra are available are strong emission-line galaxies—ranging from H II (30%) to Seyfert 2 (58%) to Seyfert 1 (12%) (Paper I). The dependence of morphological class on nuclear activity is presented in Fig. 6. It is clear that the peculiar class III and the amorphous class 0 follow nearly opposite trends while the class I galaxies are roughly evenly divided between H II and Seyfert 2 nuclear activity. The 60PKs with predominantly nonthermal nuclear activity (Seyfert 1) tend to have a class 0 morphology, with the exception of the unusual galaxy Mkn 231, while those with predominantly thermal nuclear activity (H II regionlike) tend to have a class III morphology. The 60PKs which are classified as Seyfert 2 according to optical spectroscopy are primarily those with a class I optical morphology. The few spirals (class II) in our sample show no preference for a particular type of optical nuclear activity. Table 8 clearly displays the number of galaxies of each nuclear-activity type vs morphological class. We note that there are only five Seyfert 1 galaxies in our sample, and caution must be taken when drawing conclusions from

TABLE 6. Optical photometric properties of 60 μm peakers.

IRAS NAME)	$M_{B_{total}}$	$(U-B)_{tot}$	$(B-V)_{tot}$	$(U-B)_{nuc}$	$(B-V)_{nuc}$	$(U-B)_{ann}$	$(B-V)_{ann}$	r_e	<SBe>	$r_{1/4}$	$<SB_{1/4}>$
(1)	(2)	(3)	(4)	(5)	(6)	(7)	(8)	(9)	(10)	(11)	(12)
00160–0719	−19.68	0.30	0.79	0.59	1.03	0.21	0.70	4.61	20.00	3.50	20.16
00198–7926	−21.50	−0.38	0.57	0.28	0.78	−0.54	0.51	6.52	22.14	3.75	21.66
00344–3349[a]	−20.20	−0.79	0.47	n1 −0.82	0.37	---	---				
				n2 −1.18	0.75	---	---				
				n3 −1.12	0.79	---	---				
00521–7054	−20.53	0.07	0.76	0.56	0.76	−0.06	0.76	2.62	21.04	1.46	20.53
01053+2147	−20.35	0.04	0.73	0.07	0.70	0.02	0.88	5.32	22.21	2.12	20.96
01072–0348	−20.47	0.00	0.88	0.48	1.01	−0.12	0.84	2.69	20.64	1.15	19.54
01413+0205	−20.13	0.21	1.02	0.37	0.63	0.15	1.11	6.22	20.10	4.33	20.07
01475–0740	−17.73	0.03	0.85	0.35	1.17	−0.06	0.72	2.37	20.48	1.38	20.05
02304+0012	−20.02	0.20	0.95	0.51	1.19	0.11	0.88	6.52	20.90	3.66	20.40
02530+0211	−18.73	0.12	1.07	0.21	1.02	0.09	1.08	3.58	21.42	2.19	21.10
03106–0254	−20.23	0.12	1.12	0.50	1.18	0.02	1.10	6.54	21.21	3.10	20.34
03344–2103	−18.34	0.43	0.77	0.96	0.80	0.29	0.75	13.47	21.16	7.36	20.60
04259–0440	−18.35	0.13	0.79	0.14	0.82	0.14	0.78	6.19	21.64	3.20	20.96
04385–0828	−18.49	0.42	0.77	0.91	1.11	0.29	0.63	6.18	21.43	3.30	20.82
05189–2524	−21.50	0.14	0.58	−0.37	0.91	0.40	0.45	4.55	20.04	2.00	19.01
05530+0323[b]	−15.87	−0.04	1.03	---	---	---	---				
05570–8123	−17.72	−0.02	0.77	0.09	0.32	−0.06	0.88	3.24	20.36	1.52	19.47
06097+7103*	−19.78	0.02	0.99	---	---	---	---				
06457+7429*	−19.66	0.13	0.84	---	---	---	---				
06488+2731	−21.94	0.29	0.64	−0.01	0.65	0.41	0.63	4.09	19.33	2.04	18.57
08007–6600[a]	−20.62	−0.51	0.42	n1 −0.59	0.40	---	---				
				n2 −0.52	0.38	---	---				
08014+0515	−19.16	−0.04	0.81	−0.62	0.80	0.25	0.82	5.95	20.35	2.50	19.22

TABLE 6. (continued)

08170–1126[a]	−20.11	−0.46	0.58	n1 −0.61	0.49	---	---	2.78	20.93	1.70	20.62
				n2 ---	0.86	---	---				
08321+6624*	−18.78	---	0.70	---	---	---	---				
09497–0122[c]	−19.42	−0.17	0.71	---	---	---	---	2.50	19.05		
10567–3323	−19.44	−0.24	0.38	−0.40	0.32	−0.18	0.39	2.19	21.22	1.40	21.00
12540+5708*	−21.57	0.17	0.73	---	---	---	---				
13329–3402	−18.53	0.28	0.84	0.88	0.95	0.14	0.80	5.19	19.60	2.42	18.70
13370–3123[b]	−17.09	−0.40	0.40	---	---	---	---				
13452–4155[a]	−20.73	0.17	0.46	G1 −0.06	0.49	---	---				
				G2 ---	0.43	---	---				
13536+1836[a]	−21.76	−0.18	0.74	n1 −0.37	0.46	---	---				
				n2 −0.12	1.14	---	---				
14082+1347	−18.64	0.30	0.80	0.17	0.90	0.35	0.76	6.69	21.56	3.64	20.99
14167–7236	−19.78	0.16	0.65	−0.10	0.40	0.27	0.71	4.94	20.87	2.70	20.31
15295+2414[a]	−21.63	0.06	0.68	n1 0.04	0.89	---	---	3.21	21.17	2.04	20.93
				n2 0.09	0.89	---	---				
16380–8120[a]	−20.05	0.21	0.86	G1 0.45	1.03	---	---	5.28	21.02	3.40	20.82
				G2 −0.10	0.57	---	---				
18333–6528	−19.02	0.36	0.96	0.88	1.10	0.22	0.91	6.72	20.76	3.20	19.90
19245–4140[a]	−18.69	−0.63	0.45	n1 −0.76	0.38	---	---				
				n2 −0.73	0.38	---	---				
19370–0131[c]	−17.88	−0.12	1.04	---	---	---	---	4.26	21.73		
20210+1121[c]	−21.58	−0.06	0.27	−0.39	0.89	---	---	7.03	21.40		
20253–8152[c]	−18.53	−0.06	0.45	---	---	---	---	2.69	21.14		
20460+1925[d]	−22.02	0.15	0.51	---	---	---	---				
20481–5715	−19.87	0.25	1.04	0.53	1.28	0.17	0.95	13.58	21.07	6.73	20.30
21062+1752[e]	---	−0.24	0.41	0.05	0.72	−0.32	0.28	2.70	20.70	1.24	19.76
23060+0505[c]	−22.15	−0.01	0.52	---	---	---	---	1.25	19.97		
23446+1519	−20.01	0.18	0.86	0.18	0.60	0.18	0.93	8.80	21.90	4.28	21.09
23547+1914	−18.38	0.07	0.97	0.57	1.02	−0.06	0.96	5.28	22.48	3.11	22.08

Notes to TABLE 6

Col. 1 IRAS name, superscripts have the following meaning.

[a] Nuclear colors of multiple nuclei—derived from a small aperture (Table 5)—do not refer to color within the blue quarter-light radius. Annular colors are not relevant in these instances. ⟨SBe⟩ and ⟨$SB_{1/4}$⟩ are not given due to the nearly equal contribution to the optical brightness and/or small separation of the nuclei. The exceptions (IRAS 08170, 15295, and 16380) consist of one very bright component that completely dominates the optical emission.

[b] Numerous central bright knots prevented the accurate determination of the center of the galaxy, thus ⟨SBe⟩ and ⟨$SB_{1/4}$⟩, nuclear and annular colors could not be calculated.

[c] The blue quarter-light radius is within seeing disk. This prevented the calculation of nuclear and annular magnitudes, $r_{1/4}$ and ⟨$SB_{1/4}$⟩.

[d] The effective blue half-light radius is within seeing disk. This prevented the calculation of nuclear and annular magnitudes, ⟨SBe⟩ and ⟨$SB_{1/4}$⟩.

[e] The absolute magnitude is not given because the redshift for object is unknown. The colors are not corrected for redshifted spectral energy distribution, they are only corrected for galactic extinction.

* Magnitude and/or colors taken from Veron-Cetty & Veron (1987).

Col. 2 Absolute blue magnitude for total galaxy assuming a Hubble constant of $H_0=75$ km/s/Mpc and $q_0=0.5$.

Cols. 3, 4 *UBV* colors for the total galaxy (including all multiple nuclei and galaxy components). All colors in this table are corrected for galactic reddening and redshifted spectral energy distribution.

Cols. 5, 6 *UBV* colors for the nuclei of 60 PKs. These colors were determined within a region corresponding to the blue quarter-light radius for galaxies with single nuclei, or within small apertures for multiple nuclei galaxies (see the text for explanation).

Cols. 7, 8 *UBV* colors for annular regions of 60PKs.

Col. 9 Effective blue half-light radius in arcseconds.

Col. 10 Effective blue surface brightness in mag arcsec^{-2}.

Col. 11 Blue quarter-light radius in arcsec.

Col. 12 Blue quarter-light (nuclear) surface brightness in mag arcsec^{-2}.

such a small number of objects. In Paper III of this series we present a detailed multivariate analysis which addresses the question of whether morphology class or nuclear-activity type is the fundamental parameter that produces the strongest segregation of properties.

4.1.2 FIR colors and luminosity

In Fig. 7 we display plots of the dust temperature-sensitive FIR flux ratios, $f_{60\ \mu m}/f_{25\ \mu m}$ against $f_{25\ \mu m}/f_{12\ \mu m}$. Figure 7(a) displays all 60PKs with respect to morphology class, including those with upper limits to

TABLE 7. Mean properties for the morphological classes of 60 μm peakers.

QUANTITY (1)	CLASS 0 (2)	CLASS I (3)	CLASS II (4)	CLASS III (5)
% of total sample	18%	42%	9%	31%
$\langle f_{60}/f_{25}\rangle$	1.63 ± 0.63	2.57 ± 1.01	3.16 ± 0.26	3.13 ± 0.87
$\langle f_{25}/f_{12}\rangle$	3.05 ± 0.99	3.82 ± 0.87	---	4.33 ± 0.99
$\langle f_{60}/f_{100}\rangle$	1.25 ± 0.30	1.21 ± 0.16	1.10 ± 0.13	1.17 ± 0.16
$\langle \log(L_{60\mu m}/L_S)\rangle$	10.08 ± 0.24	10.32 ± 0.78	10.50 ± 0.37	11.10 ± 0.67
$\langle \log(L_B/L_\odot)\rangle$	9.55 ± 0.34	9.65 ± 0.59	9.81 ± 0.29	10.22 ± 0.49
$\langle \log(L_{60\mu m}/L_B)\rangle$	0.53 ± 0.30	0.66 ± 0.44	0.69 ± 0.17	0.87 ± 0.37
$\langle M_B\rangle$	− 18.94 ± 0.86	− 19.24 ± 1.45	− 19.60 ± 0.71	− 20.63 ± 1.22
$\langle \log(M_g/L_B)\rangle$	− 2.18 ± 0.31	− 1.88 ± 0.38	− 1.78 ± 0.20	− 1.61 ± 0.46
$\langle$SBe$\rangle$ (Bmag/arcsec^2)	20.30 ± 0.72	20.89 ± 0.80	21.40 ± 0.71	21.32 ± 0.73
$\langle r_e\rangle$ (kpc)	1.28 ± 0.42	2.19 ± 1.07	3.62 ± 1.14	3.76 ± 2.50
$\langle$B-V$\rangle_{total}$	0.80 ± 0.17	0.81 ± 0.21	0.73 ± 0.24	0.61 ± 0.20
$\langle$B-V$\rangle_{nucl}$	0.91 ± 0.40	0.87 ± 0.26	0.84 ± 0.31	0.79 ± 0.10
$\langle$B-V$\rangle_{annul}$	0.80 ± 0.11	0.80 ± 0.20	0.70 ± 0.36	0.69 ± 0.26

Notes to TABLE 7

Summary of average properties for each morphological class of 60PKs. The number of galaxies used for calculating the average properties of each morphological class are often not the same, and depend on the property being measured.

Col. 1 Mean Property: fraction of total sample; FIR flux ratios $f_{60\ \mu m}/f_{25\ \mu m}$, $f_{25\ \mu m}/f_{12\ \mu m}$, $f_{60\ \mu m}/f_{100\ \mu m}$ (galaxies with upper limits at 12 or 100 μm were not included (cf. Table 1 of Paper I; 60 μm luminosity in units of solar luminosity; blue optical luminosity in units of solar luminosity; 60-μm-to-blue luminosity ratio; absolute blue magnitude; effective blue surface brightness in mag/arcsec^2; effective radius (in kpc); integrated (B-V); nuclear (B-V) (within blue quarter-light radius); annular (B-V).

Col. 2 Class 0 (amorphous) {IRAS 20460 was excluded when caclulating mean properties of class 0 60PKs. This source has the largest redshift in our sample, thus the classification is somewhat dubious—see the text}.

Col. 3 Class I (amorphous+features).

Col. 4 Class II (spiral).

Col. 5 Class III (peculiar).

the 12 μm flux (as indicated by arrows next to data point). Figure 7(b) displays the mean values of the FIR flux ratios for each morphological class, and excludes those sources with upper limits at 12 μm. The error bars in Fig. 7(b) refer to the standard deviation of mean value. We find a correlation between the FIR flux ratios and optical morphology in the sense that the FIR flux ratios for 60PKs tend to become "cooler" along the morphology sequence 0–I–III (Fig. 7). This dependence of optical morphology on FIR flux ratios is not surprising considering the correlation between optical morphology and optical nuclear-activity type discussed above. In Paper I we established that 60PKs follow the well-known segregation of FIR flux ratios with respect to nuclear-activity type—namely that starburst galaxies tend to have cooler FIR flux ratios compared to Seyferts [cf. Fig. 5(a) in Paper I].

The 60PKs display a morphological segregation with respect to 60 μm luminosity (Fig. 8): all 60PKs with $L_{60\ \mu m} > 10^{11} L_\odot$ show peculiarities in their optical morphology (class I or class III)—a trait commonly found for FIR-selected samples of galaxies (e.g., Sanders *et al.* 1988a,b). As the optical morphology becomes more peculiar along the morphological sequence 0–I–II–III, the mean luminosities $\langle \log(L_{60\ \mu m})\rangle$ increase from 10.1 to

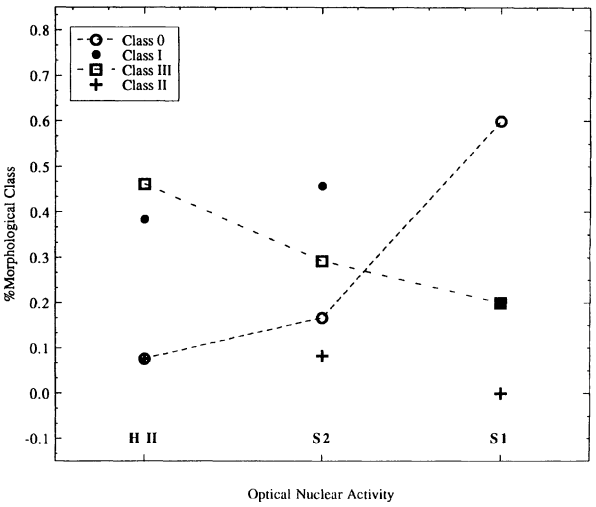

FIG. 6. The population frequency of optical morphological class vs the type of optical nuclear activity. The amorphous class is represented by open circles; the peculiar class by open boxes; the amorphous+features class by filled circles, and the spirals class by plus signs. The dashed lines connecting the amorphous and peculiar classes emphasize the opposite trends followed for each of these classes with respect to nuclear-activity type. The total number of H II, Seyfert 2, and Seyfert 1 galaxies being plotted is 13, 23, and 5, respectively (see the text).

TABLE 8. Numbers of galaxies of each activity type vs morphological class.

Nuclear Activity Type*	Morphological Class				
	CLASS 0	CLASS I	CLASS II	CLASS III	Total
Seyfert 1	3	1	0	1	5
Seyfert 2	3	11	2	7	23
HII	1	5	1	6	13
unknown	1	2	1	0	4
Total	8	19	4	14	45

Notes to TABLE 8.

* Nuclear Activity Type is taken from paper I and refers to the optical spectroscopic type based on emission line ratio diagnostics. (see Sec. 4.1.1 of paper I for more details)

11.0 (Table 7). However, since the mean optical luminosities increase likewise, we need to consider a dimensionless quantity such as $L_{60\ \mu m}/L_B$.

4.1.3 FIR-to-optical luminosity ratios

The ratio of 60-μm-to-blue luminosity is calculated according to

$$\frac{L_{60\ \mu m}}{L_B}=\frac{F_{60\ \mu m}}{4.4\times 10^{(-0.4m_B-8.17)}}, \quad (7)$$

where the blue luminosity was derived from the quasibolometric flux given by $F_B=\nu f_\nu$ at 4400 Å, assuming a calibration of 4300 Jy at 0 mag (Allen 1973); m_B is the apparent blue magnitude corrected for galactic reddening; and $F_{60\ \mu m}$ is the 60 μm flux in units of (W m^{-2}). In general, galaxies have a very wide range of $L_{60\ \mu m}/L_B$, from less than 0.1 to over 100. For 60PKs $L_{60\ \mu m}$ always exceeds L_B (Fig. 9), and the median value of $L_{60\ \mu m}/L_B=7$ is three times larger than that of randomly selected IRAS galaxies (Soifer *et al.* 1987a). As apparent in Fig. 9 the mean blue luminosity is significantly lower than the 60 μm luminosity, while the dispersion in the blue luminosities, $\sigma[\log(L_B)]=0.56$, is about 75% of the 60 μm luminosity, $\sigma[\log(L_{60\ \mu m})]=0.77$. The ratio $L_{60\ \mu m}/L_B$ correlates well with $L_{60\ \mu m}$ [Fig. 9(a)], while there is apparently no correlation between $L_{60\ \mu m}/L_B$ and L_B [Fig. 9(b)]. Therefore larger $L_{60\ \mu m}/L_B$ ratios imply larger $L_{60\ \mu m}$ rather than smaller L_B, so that the 60 μm luminosity and the blue luminosity components are essentially independent. Thus, the correlation of $L_{60\ \mu m}/L_B$ with $L_{60\ \mu m}$ is mainly a result of increasing FIR emission in the more FIR-luminous galaxies, rather than a result of de-

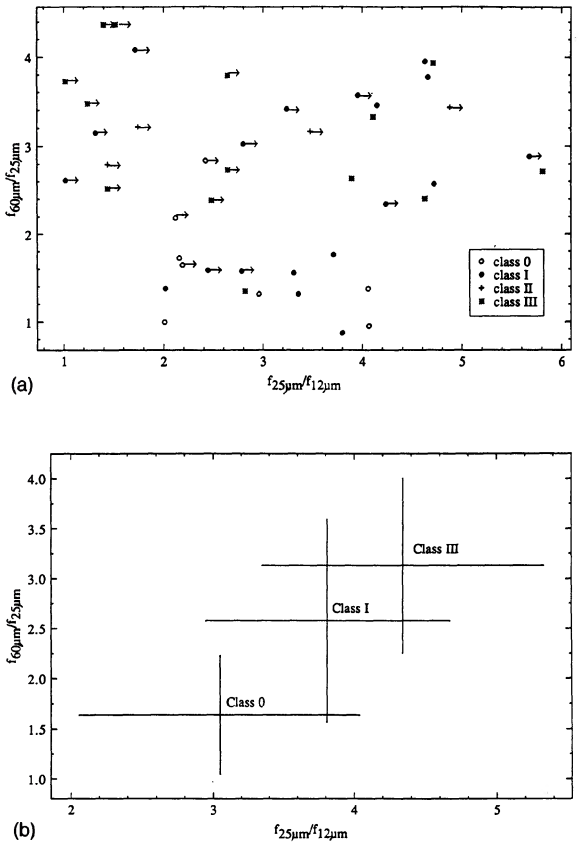

FIG. 7. (a) Plot of $f_{25\ \mu m}/f_{12\ \mu m}$ vs $f_{60\ \mu m}/f_{25\ \mu m}$ for all 60PKs, including those with upper limits at 12 μm. It is evident from this graph that the amorphous galaxies tend to have warmer FIR colors while the peculiar galaxies tend to have cooler FIR flux ratios. (b) Plot of the mean of $f_{25\ \mu m}/f_{12\ \mu m}$ vs the mean of $f_{60\ \mu m}/f_{25\ \mu m}$ for each morphological class, excepting class II as none of the objects from this class of 60PKs was detected at 12 μm. All 60PKs with upper limits at 12 μm were omitted in this plot. The error bars refer to the standard deviation of the mean values for each class. It is evident from this graph that as the morphology becomes amorphous the FIR colors become cooler.

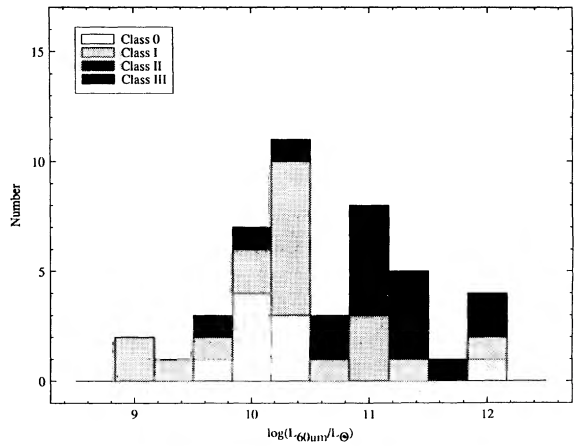

FIG. 8. Histogram of the logarithm of the 60 μm luminosity in units of solar luminosity for 60PKs with respect to morphological class.

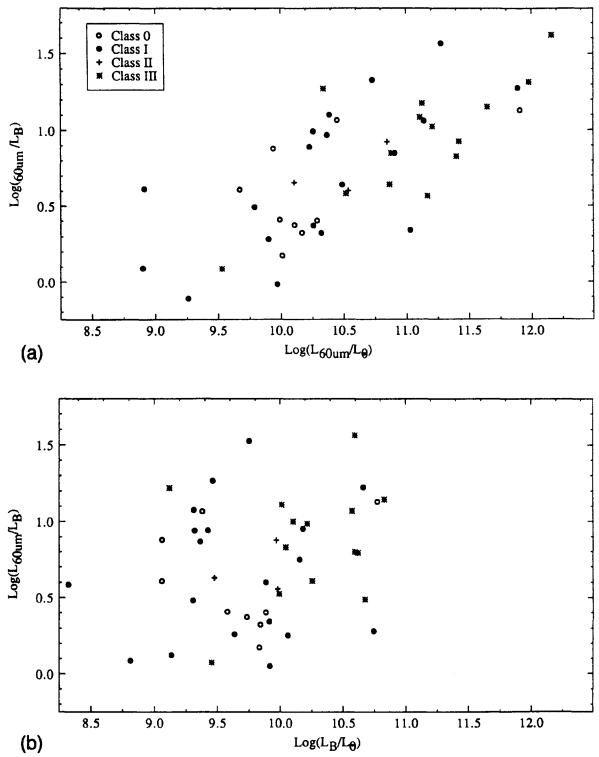

FIG. 9. (a) Plot of the logarithm of 60-μm-to-blue luminosity ratio vs the logarithm of the 60 μm luminosity in units of solar luminosity. The symbols are the same as in Fig. 5. There is a clear trend for increasing $L_{60\ \mu m}/L_B$ with increasing $L_{60\ \mu m}$. (b) Plot of the logarithm of 60-μm-to-blue luminosity ratio vs the logarithm of the blue luminosity in units of solar luminosities. There is no trend of $L_{60\ \mu m}/L_B$ with $L_{60\ \mu m}$. Comparison of this plot with (a) clearly shows that the blue luminosity does not extend as high as the 60 μm luminosity.

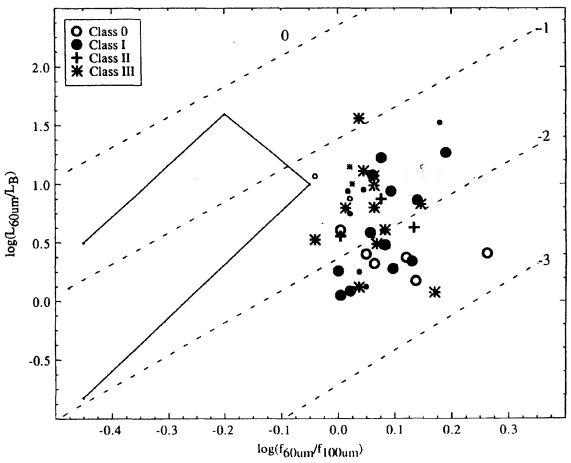

FIG. 10. Plot of the 60-μm-to-blue luminosity ratio vs the 100-μm-to-60-μm spectral index. As discussed in Paper I, the 60-μm-to-blue luminosity ratio can be interpreted as a measure of the ratio of the gas mass-to-blue luminosity. The dashed lines represent lines of constant ratio of gas mass-to-blue luminosity, labeled in units of $\log(\mathcal{M}_\odot/L_\odot)$. The rectangular region outlined in this plot is populated by FIR-selected galaxies (without color restrictions) (e.g., Soifer *et al.* 1987a,b, Wolstencroft *et al.* 1986). The symbols have the same meaning as in Fig. 5, with the smaller symbols representing 60PKs with upper limits for $f_{100\ \mu m}$.

creasing visible radiation. A morphological segregation is apparent, with $L_{60\ \mu m}/L_B$ increasing from class 0 to class III galaxies (see also Table 7), i.e., galaxies with morphologies indicative of a recent interaction have a larger FIR emission per unit blue luminosity than galaxies whose morphology is apparently relaxed. Similar trends have been observed for both optically selected and FIR-selected galaxies (e.g., Lonsdale *et al.* 1984).

4.1.4 Gas mass-to-blue luminosity ratio

The mass of FIR-emitting dust and of the associated gas, $\mathcal{M}_g$, was estimated in Paper I. Millimeter wave CO observations of some of the galaxies in our sample (e.g., Scoville *et al.* 1989, Sanders *et al.* 1986) yield molecular gas (H_2) masses that are only slightly larger than the gas masses we infer (10^6–$10^{10}\mathcal{M}_\odot$) from their FIR properties, indicating that the latter masses are fair estimates of the total gas mass. There is a weak tendency for the gas mass-to-blue luminosity ratio to decrease as the morphological type changes from peculiar (class III) to amorphous (class 0) (Table 7).

The 60-μm-to-blue luminosity ratio is plotted against the FIR spectral index in Fig. 10, where the symbols refer to morphological class as described for Fig. 5 (Sec. 3.1.2)—the larger symbols refer to good quality detections at 60 and 100 μm and the correspondingly smaller symbols refer to upper limits at 100 μm. On this same diagram are drawn lines of constant ratio of gas mass to blue luminosity for $\log(\mathcal{M}_g/L_B)=0$, -1, -2, and -3, where $\mathcal{M}_g$ is in units of solar masses and L_B is in units of solar luminosity. The 60PKs cover nearly two orders of magnitude in $\mathcal{M}_g/L_B$, with the majority in the range $-1<\log(\mathcal{M}_g/L_B)<-2$. For comparison, FIR-selected galaxies (without color restrictions) populate the rectangular region between the -2 and 0 lines (Soifer *et al.* 1987a, Wolstencroft *et al.* 1986). Although our FIR-selection criteria has singled out galaxies with dust temperatures that are larger than randomly selected IRAS galaxies, the dust and gas contents are similar to those of other IRAS galaxies. Thus, the 60PKs are able to heat more than 10^6–$10^{10}\mathcal{M}_\odot$ of gas and dust to temperatures which are significantly greater than those found in other samples of galaxies. The high dust temperatures for the 60PKs presumably result from the concentration of dust and gas in the nuclear regions of the galaxies, where it is exposed to a more intense radiation field, while the relatively cooler dust temperatures of randomly selected IRAS galaxies result from dust and gas that is dispersed throughout the galaxies, where it is heated by the general interstellar radiation field.

4.1.5 Integrated optical magnitudes and colors

The absolute B magnitudes of 60PKs span a large range, from values typical of dwarf galaxies to values characteristic of the brightest normal galaxies [cf. Fig. 9(b)]. The $(B-V)$ colors cover a similarly wide span, from values typical of late-type dwarfs to values characteristic of

giant ellipticals (Fig. 11 and Table 7). The V magnitude was not available for IRAS 00160, but we obtain $B-V$ from the $B-R$ color using the transformation

$$(B-V)_c=0.59(B-R)_c. \quad (8)$$

This transformation is obtained from the foreground extinction corrected colors of galaxies in our sample with available B, V, and R magnitudes. It is similar to other determinations (e.g., Salzer *et al.* 1989). The integrated $(B-V)_c$ colors of 60PKs are comparable to those of other FIR-selected samples of galaxies (e.g., Armus *et al.* 1987, Vader & Simon 1987).

The dependence of optical luminosities and colors on morphological class is weak. The peculiar galaxies in our sample tend to have larger integrated B luminosities and bluer $(B-V)$ colors, while the amorphous galaxies are intrinsically fainter and redder (Table 7). Similar results have been found for other FIR flux-limited samples of galaxies (e.g., Armus *et al.* 1987) as well as for optically selected Seyferts (e.g., MacKenty 1990). The large range in colors of 60PKs is illustrated in the two-color UBV diagram (Fig. 11), where the solid line represents the observed average locus of normal galaxies which has a narrow width ($\sigma<0.5$ mag). This locus of normal galaxies is well explained in terms of theoretical stellar population models with standard stellar mass functions, and a variety of star-formation histories, but excluding strong bursts of star formation in the last 5×10^8 yr (Larson & Tinsley 1978). The 60PKs show a much larger scatter than normal galaxies, which we attribute to a combination of nuclear activity due to recent ($<5\times10^8$ yr) bursts of star formation and/or a nonthermal source, and internal extinction. The upper short-dashed line in Fig. 11 shows the effect of ongoing starbursts of variable strength. The lower dotted line represents the evolutionary track after the cessation of a single strong burst. The upper short-dashed line and lower dotted line define an area that encompasses about 50% of the sample of 60PKs. The remaining galaxies have redder $(B-V)$ for a given $(U-B)$, as would be expected from internal reddening. We show this effect by superposing an internal reddening of $E(B-V)=0.4$ on the variable starburst locus (long-dashed line in Fig. 11). It is clear that a combination of starburst and/or active nucleus and such internal reddening can account for the UBV colors of the 60PKs with only a few exceptions. One of these exceptions is IRAS 19370 which is a very red Seyfert 2 galaxy whose UBV colors suggest an internal reddening of the order of $E(B-V)=1$, which is as large as the nuclear reddening inferred from its optical spectrum (Paper I). Two other exceptions (IRAS 00344 and 19245) are H II regionlike galaxies that have very blue $(U-B)$ colors for their $(B-V)$ colors. These colors may be explained by a blue contribution of gaseous emission. Gaseous emission is also apparent from the flat continua of their optical spectrum and their blue near-infrared colors (Paper I). At redshifts $z<0.2$ the effect of emission lines in the U and B passbands is negligible, but the V passband is contaminated by the [O III] lines at ~5000 Å (and the R passband by the Hα+[N II] lines). Using the observed line strengths from optical spectra we estimate that the line emission contributes up to 20% to the total flux in the V passband, and can cause a reddening in $B-V$ of up to 0.2 mag. Hence the integrated UBV colors indicate a global internal extinction of order $E(B-V)=0.2$, which is considerably smaller than the nuclear values inferred from the Balmer decrement (Paper I), but similar to the global internal extinction of other IRAS-selected Seyfert galaxies (e.g., Goudfrooij & de Grijp 1990).

We conclude that nuclear activity, starburst or nonthermal, of the 60PKs, combined with central dust obscuration can account for the large scatter of the integrated UBV colors. One would therefore expect the nuclear colors to show an even larger scatter with respect to the locus of normal galaxies, as is indeed shown in Fig. 11(b).

4.1.6 Nuclear and annular optical colors

The colors of the nuclei and annular regions of 60PKs are shown in Figs. 11(b) and 11(c), respectively. These two figures are incomplete with respect to Fig. 11(a) because nuclear and/or annular colors are missing for those objects with integrated colors taken from the literature (Table 6), with seeing limitations, and with multiple nuclei (Table 5). For the case of double galaxies (e.g., IRAS 13452, 16380, 20210) we have adopted as the IRAS source the galaxy with the reddest near-infrared colors (cf. Table 5 of Paper I). The nuclei of the 60PKs extend to much redder colors [Fig. 11(b)] than their outer annular regions [Fig. 11(c)]. This must be due to unusually strong internal reddening, in support of our view that the FIR emission of 60PKs is due to an often heavily obscured central source. On the other hand, about one-third of the nuclei have bluer $U-B$ than their annular regions, sometimes in spite of significantly redder $B-V$ [a good example is 05189 (Table 6)]. This is explained by the fact that the active nucleus significantly contributes to the V passband flux by [O III] emission lines at ~5000 Å, which is negligible within the U and B passbands. The colors of the nuclei, by themselves or relative to their annular regions, are not related to morphological class.

The scatter displayed by the annular colors of class I and class III objects [Fig. 11(c)] indicates that the main bodies of these galaxies have also been significantly perturbed in their star-formation histories by the interaction/merger event that we believe is at the origin of their perturbed morphology and the 60PK phenomenon. The few class 0 objects have relatively red annular colors typical of normal optically selected amorphous galaxies.

4.2 Blue Surface Brightness

Both ⟨SBe⟩ and $\langle SB_{1/4}\rangle$ span a range of 3 mag/arcsec^2. They are well correlated, with a slope of 1 and an average difference of 0.7 mag arcsec^{-2}. The trends or absence thereof described below for ⟨SBe⟩ also hold for $\langle SB_{1/4}\rangle$. A plot of ⟨SBe⟩ against M_B is a scatter diagram (Fig. 12). For comparison we also show the relationship between M_B and ⟨SBe⟩ for Virgo ellipticals (Vader 1986). The range and average value of the effective surface brightness for all

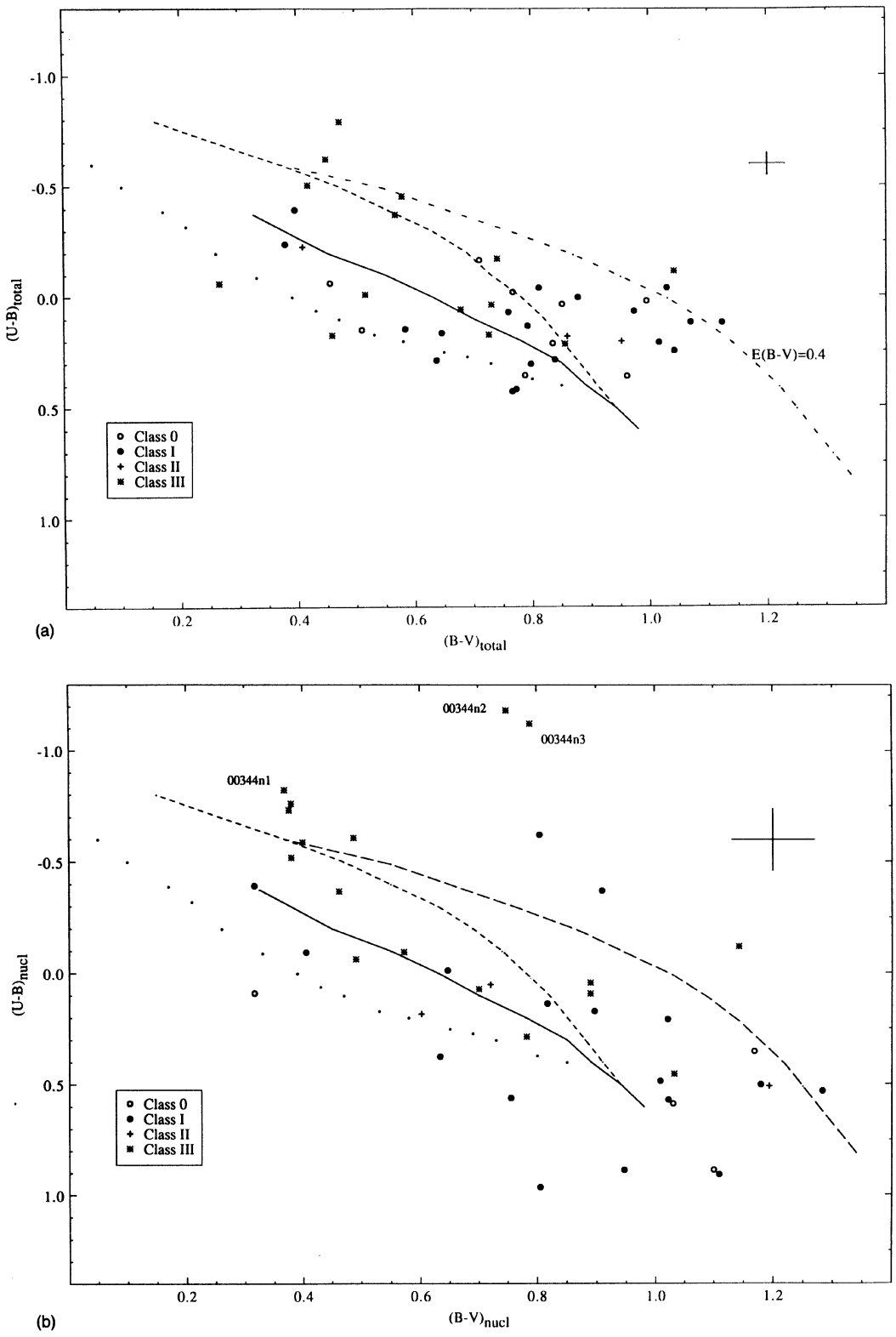

FIG. 11. *UBV* diagram of integrated colors of 60PKs corrected for galactic reddening and redshifted spectral energy distribution. The solid line represents the locus of normal galaxies which is well explained in terms of theoretical stellar population scenarios with standard stellar mass functions, and a variety of star-formation histories excluding strong bursts of star formation in the last 5×10^8 yr (Larson & Tinsley 1978). The upper short-dashed line is the locus of different burst strengths, and the lower dotted line represents the evolutionary track after the cessation of a strong burst. The long-dashed line represents the short-dashed line with an internal reddening of $E(B-V)=0.4$. The symbols have the same meaning as in Fig. 5. (b) The same as (a) except that the *UBV* colors represent the nuclei of the 60PKs. (c) The same as (a) except the *UBV* colors are for the annuli of the 60PKs whose inner boundary is defined by their blue quarter-light radii and outer boundary is defined by the extent of their curves of growth.

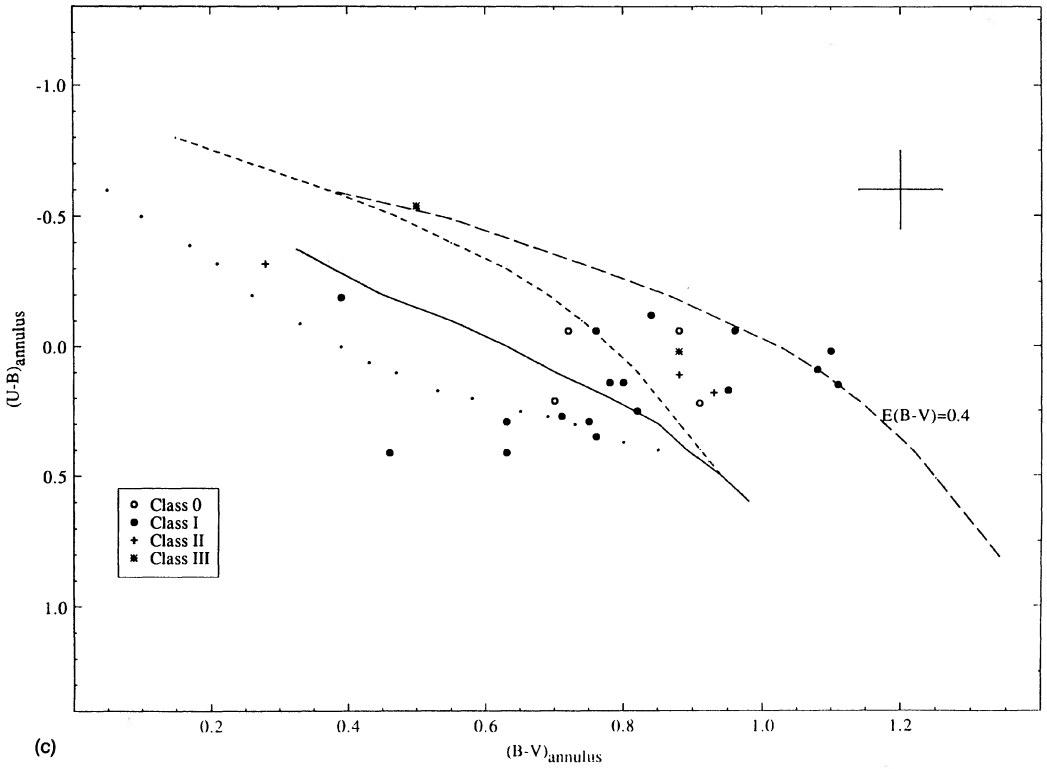

FIG. 11. (continued)

60PKs of 20.94 ± 0.81 is almost identical to that found for normal early type galaxies in the same absolute magnitude range (e.g., Sandage 1983, Binggeli *et al.* 1984), and 1 mag brighter than for later-type galaxies. This implies that 60PKs and normal early type galaxies also have similar optical sizes. Since 60PKs are expected to become normal early type galaxies after the cessation of nuclear activity, the above suggests that on average the optical surface brightness will remain the same. This is consistent with our proposition that the central source in 60PKs is heavily obscured (Paper I), and therefore contributes little to the optical emission of the galaxy. A plot of ⟨SBe⟩ against $L_{60\ \mu m}$ is also a scatter diagram (not shown). Finally, surface brightness is not correlated with optical color. The effective surface brightness of the peculiar 60PKs (class III) is thus presumably a result of their distended morphology, independent of optical or FIR luminosity.

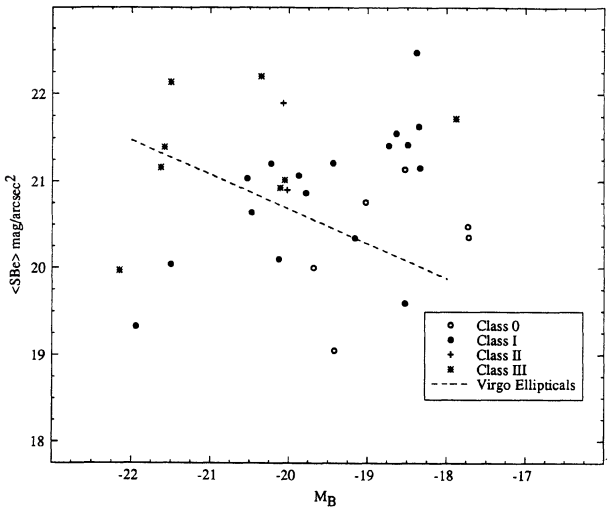

FIG. 12. Plot of effective blue surface brightness ⟨SBe⟩ against the absolute blue magnitude M_B.

The effective blue surface brightness of the 60PKs is not correlated with either $L_{60\ \mu m}$ or L_B individually, but a weak trend appears with $L_{60\ \mu m}/L_B$ in the sense that fainter ⟨SBe⟩ is associated with larger values of $L_{60\ \mu m}/L_B$ (Fig. 13). This result is interesting since both quantities considered are distance independent. It is most likely due to dust extinction in the central region: the systems with faintest surface brightness have the most heavily obscured central regions. This global trend is reflected in the fading of ⟨SBe⟩ with increasing $\langle L_{60\ \mu m}/L_B \rangle$ along the morphological sequence 0–I–III. This trend can be attributed to the more disturbed objects having a larger internal extinction, while the active central region contributes an increase in ⟨SBe⟩ in the undisturbed amorphous systems with relatively small $L_{60\ \mu m}/L_B$. An opposite global trend has been observed for optically selected normal spirals (Phillipps & Disney 1988) and irregulars (Hunter *et al.* 1989), and is attributed to enhanced star formation that causes both brighter ⟨SBe⟩ and larger $L_{60\ \mu m}$, i.e., extinction ef-

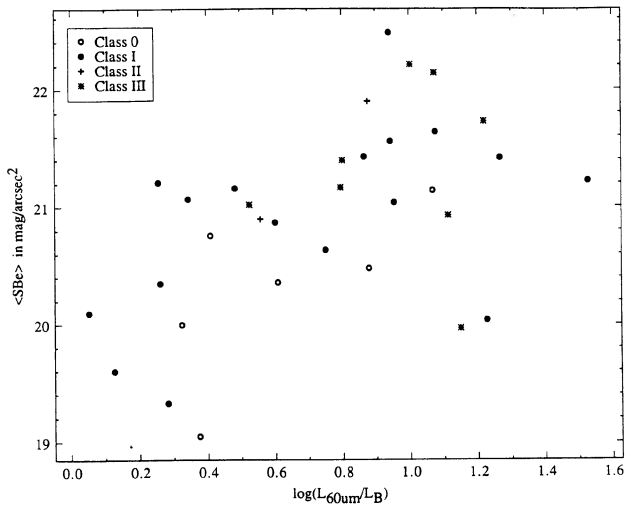

FIG. 13. Plot of effective blue surface brightness ⟨SBe⟩ vs the 60-μm-to-blue luminosity ratio.

fects are not important. To the best of our knowledge, studies of this correlation do not exist in the literature for other IRAS-selected samples of galaxies.

The effective blue surface brightness shows a weak dependence on the FIR flux ratio $f_{60\ \mu m}/f_{25\ \mu m}$. The 60PKs with the warmest $f_{60\ \mu m}/f_{25\ \mu m}$ colors have brighter ⟨SBe⟩, while those with the coolest FIR flux ratios $f_{60\ \mu m}/f_{25\ \mu m}$ tend to have fainter ⟨SBe⟩ (Fig. 14). No trend is observed for the ratio of $f_{60\ \mu m}/f_{100\ \mu m}$ with ⟨SBe⟩.

5. SUMMARY OF OBSERVATIONAL RESULTS

In contrast to randomly selected IRAS galaxies, which are mostly spirals, the morphology of the 60PKs is predominantly amorphous or peculiar. This has led us to adopt a morphological classification scheme consisting of four classes: 0—amorphous; I—amorphous + features; II—spirals; III—peculiar. The relative population frequencies and mean characteristics of the morphological classes are given in Table 7. The usefulness of our classification depends on its ability to discriminate between and single out physically meaningful characteristics particular to each class. We summarize the many properties that are indeed dependent on optical morphological class.

(1) The 60PKs, all of which are strong emission-line galaxies, show a dependence of optical nuclear activity with morphology in the sense that the nuclear activity tends to change from starburst to Seyfert 2 to Seyfert 1 along the morphological sequence III–I–0.

(2) The 60PKs show a dependence of morphology on both $L_{60\ \mu m}$ and $L_{60\ \mu m}/L_B$. All galaxies with peculiarities in their morphology tend to have relatively large values of $L_{60\ \mu m}$ (another well-known result, e.g., Sanders *et al.* 1988a,b), while those galaxies with a smooth global light distribution are less luminous in the FIR. The luminosity ratio $L_{60\ \mu m}/L_B$ tends to decrease along the morphological sequence III–I–0.

The FIR flux ratios $f_{60\ \mu m}/f_{25\ \mu m}$ and $f_{25\ \mu m}/f_{12\ \mu m}$ also vary with morphology. The class 0 galaxies tend to have warmer FIR colors, while the class III objects tend to have cooler FIR flux ratios, and the class I galaxies have intermediate FIR flux ratios. This trend is a direct result of the dependence between morphology and nuclear activity, and the well-known dependence of FIR spectral slopes with nuclear activity (i.e., which are steepest for starburst galaxies, flattest for Seyfert 1's, and intermediate for Seyfert 2's).

(3) The absolute blue magnitudes of the 60PKs cover a wide range ($-22 < M_B < -16$) similar to other FIR-selected samples. The integrated $(B-V)$ colors have values that range from those typical of late-type dwarf galaxies to those typical of giant ellipticals. Both the integrated and annular broadband colors tend to become redder along the sequence III–I–0. The colors of the nuclei do not depend on morphological class, and can be extremely red, presumably as a result of internal extinction.

(4) The mean effective blue surface brightness and the optical sizes of our sample of 60PKs are similar to those obtained for normal early type galaxies.

A new and intriguing result of our observations is the trend of increasing 60-μm-to-blue luminosity ratio with decreasing effective blue surface brightness, which is most likely due to internal extinction. This is reverse to the trend obtained for optically selected normal galaxies, which is attributed to enhanced star formation. If internal extinction effects prevail, this reinforces our suggestion (Paper I) that 60PKs are good candidates for containing dust-obscured Seyfert 1 nuclei.

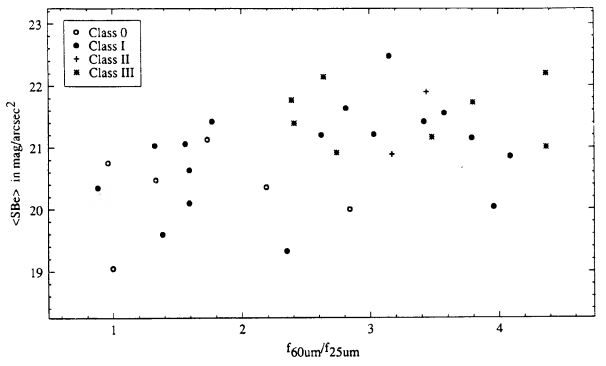

FIG. 14. Plot of the effective blue surface brightness ⟨SBe⟩ vs the FIR flux ratio $f_{60\ \mu m}/f_{25\ \mu m}$.

6. DISCUSSION OF RESULTS

6.1 Interpretation of Classification Scheme

One of the major goals of our observing program was to determine the morphology of the 60PKs, roughly half of which were previously unidentified in optical catalogues. We have proposed a morphological classification system and argued that the differences between the four morphological classes are related to fundamental differences in the galaxies themselves, and are not an artifact of observa-

tional limitations. One of the interesting findings of this investigation is the paucity of spiral structure among the galaxies in our sample. We find an unusual preponderance of amorphous galaxies on the one hand, and a large fraction of peculiar galaxies on the other hand.

The morphological characteristics described in this paper and the highly centrally concentrated activity of 60PKs (Paper I) strongly favor the hypothesis that 60PKs are the product of galaxy interactions. The peculiarities of class I and class III galaxies, the faint outer envelopes of the few spirals in our sample (class II), as well as the amorphous appearance of class I galaxies can all be attributed to interactions. In the case of spiral galaxies, the interaction was strong enough to create an outer envelope but too weak to fully destroy the disk or clear it of its gas and spiral structure. In the case of amorphous galaxies, the interaction was strong enough to funnel the gas to the central region and erase any existing spiral structure without necessarily destroying the disk. For many of the peculiar galaxies, the interaction has been strong enough to fully destroy the disk. Furthermore, the observational results summarized in Sec. 5 suggest that galaxy interactions and nuclear activity are closely linked for 60PKs. A connection between nuclear activity and interactions has often been proposed. For example, Gunn (1979) suggested that an interaction may be an effective means for supplying the nucleus of an active galaxy with fuel. Recent numerical simulations clearly demonstrate that galactic interactions are indeed an effective means for transporting gas and dust to the center of a galaxy (e.g., Noguchi 1988, Hernquist 1989, Barnes & Hernquist 1991). Assuming that 60PKs are the product of interactions, we propose two simple scenarios to explain their phenomenology. Scenario A suggests that the morphological classes reflect differences in the precursor galaxies, while scenario B interprets the morphology classification scheme as an evolutionary sequence.

We describe each of these two extreme scenarios and discuss how they fare in terms of the observational results.

6.1.1 Scenario A: The classification scheme reflects differences in the precursors of 60PKs

Scenario A proposes that the optical morphologies of 60PKs reflect the nature and relative disk and gas masses of the precursor galaxies. There is no evolution from one morphological class to another during a given 60PK phase. In this scenario class III 60PKs result from the interaction/merging of precursor galaxies with massive star-forming disks (such as gas-rich spirals) that generate typical signs of the interaction in the form of luminous bridges and tails of stars (Toomre & Toomre 1972), and supply large amounts of gas and dust to the central regions on short time scales (Barnes & Hernquist 1991). If a broadline region already exists, the gas and dust will act to obscure it, giving rise to optical spectra characteristic of Seyfert 2 or starburst galaxies. Precursor galaxies with less prominent disks (or no disks at all) would generate less obvious signatures of the interaction and produce 60PKs with a class 0 or class I optical morphology, and they would have less gas and dust available to funnel to the central region, thus the dust shroud will not be as thick as in the case of class III 60PKs. In all cases the interaction was strong enough to funnel all the gas to the center, by destroying the disk or depleting it of its gas, so that any existing spiral structure is erased. Class II galaxies represent those rare cases whose spiral structure survived an interaction strong enough to produce the observed nuclear activity. These requirements, and the limited duration of the central activity phase, explains the scarcity of 60PKs. This scenario precludes evolution from one class to another with the implication that the central activity ceases before the supply of gas and dust is exhausted, so that a given galaxy could have recurrent 60PK phases, and thus undergo a progressive change in morphology.

6.1.2 Scenario B: The classification scheme represents an evolutionary sequence

Scenario B proposes that the morphological sequence of 60PKs represents a time sequence following an interaction/merger event involving at least one galaxy with a prominent star-forming disk. In this case class III galaxies represent the relatively early stage of an interaction with prominent tidal features, class I galaxies depict a later stage of the interaction event where evidence for the past interaction is revealed through low surface brightness features, while class 0 galaxies represent the latest stages after an interaction event with no visible fossil records of this event except for the active central source. Class II galaxies do not fit into this scheme.

In this scenario the appearance of the central source evolves along with the morphology. During the class III phase, the channeling of gas and dust toward the central regions has produced a starburst and a thick circumnuclear dust shroud that would obscure any previously existing nuclear source. The starburst subsides and the dust shroud is depleted due to radiation pressure and evaporation by the hard radiation field of the active galactic nucleus (AGN), supernovae winds, etc., so that the narrow-line region surrounding the AGN (Seyfert 2) becomes visible in class I galaxies and finally as the central dust is exhausted the broadline region (Seyfert 1) becomes apparent in class 0 galaxies. This evolution of central activity has been proposed by many workers (e.g., Norman & Scoville 1988, Sanders *et al.* 1988a,b). For 60PKs, the last stage would be an amorphous Seyfert 1 galaxy.

6.2 Confrontation with Observational Results

Scenario B is more restrictive in terms of precursor galaxies, all of which should be gas-rich disk systems. In contrast to scenario A, scenario B allows for only one 60PK phase during the lifetime of a given galaxy. Since the difference among precursor galaxies in scenario A can, in principle, be construed as due to recurrent 60PK phases resulting in a morphological evolution similar to that described in a single such phase by scenario B, it is obvious that our observations do not allow us to discriminate between the two scenarios. Whether the 60PK stage can be recurrent or not, depends on the efficiency of central gas

depletion by a central starburst or AGN on the one hand, and on the possibility of a nucleus that is dormant though embedded in a large central gas concentration on the other hand.

6.2.1 Optical nuclear activity

The observed dependence of nuclear activity with morphology (Fig. 6) is consistent with both scenarios, although the underlying cause for the relationship between morphology and nuclear activity is fundamentally different for the two scenarios. Both scenarios predict a decreasing amount of circumnuclear dust and gas along the morphological sequence III–I–0. According to scenario A, the precursor galaxies of class III objects have more dust and gas than the class I and class 0 galaxies, respectively. This results in complete obscuration at optical wavelengths of any pre-existing nonthermal source in class III galaxies, and to a lesser degree for class I and class 0 galaxies, respectively. According to scenario B, the nuclear activity becomes more apparent along this morphological sequence (III–I–0) due to the depletion of circumnuclear dust with time; the circumnuclear dust has just formed in the class III galaxies, while the dust shroud has depleted with time for the older class 0 galaxies.

6.2.2 FIR properties

The FIR colors ($f_{60\ \mu m}/f_{25\ \mu m}$ and $f_{25\ \mu m}/f_{12\ \mu m}$) for the 60PKs become cooler along the morphological sequence 0–I–III (Fig. 7). Galaxies with nuclei obscured by a very thick, dust shroud have relatively cool FIR colors, because the emission from the hotter, inner layers has been absorbed by the cooler outer layers of dust. The central luminosity source will destroy the inner dust component quite rapidly (e.g., Sanders *et al.* 1988b), while at the same time the cooler dust will move inwards so that the amount of cool dust effectively decreases. As the central dust decreases, the dust shroud will cease to be optically thick at these mid-infrared wavelengths, resulting in warmer FIR flux ratios, because we are detecting hotter dust located closer to the active nucleus/starburst. Further support for our claim that the circumnuclear dust has very large extinctions and opacities is given by Krolik & Lepp (1989), who studied the physical state of obscuring material in (AGN), and find that it is possible to have radiation at only relatively long FIR wavelengths $\geqslant$50–100 μm leaving the central region. We conclude that both scenarios A and B can equally well account for the observed mean FIR colors of the 60PKs, because both scenarios attribute the increasing FIR color temperature along the morphological sequence III–I–0, to a decreasing mass of circumnuclear dust along this same sequence. We observe a weak morphological dependence with respect to the luminosity ratio $L_{60\ \mu m}/L_B$, in the sense that $L_{60\ \mu m}/L_B$ decreases along the sequence III–I–0 (Table 7). This is consistent with a decrease in the circumnuclear dust content along the morphological sequence III–I–0.

The fate of the circumnuclear dust in the 60PKs is an interesting question to consider. Due to several mechanisms such as radiation pressure and evaporation by the hard radiation field of the central source, the dust shroud will be depleted with time. An order of magnitude estimate for the lifetime of the dust shroud is $< 10^7$ yr (e.g., Sanders *et al.* 1988b). The relatively short lifetime for the circumnuclear dust is a plausible explanation for the paucity of galaxies with FIR spectral energy distributions that peak near 60 μm, and is consistent with both scenarios.

6.2.3 Optical colors

The annular *UBV* colors, which represent the outer regions of the galaxy free of contamination by the nucleus, are slightly redder for the amorphous 60PKs compared to the peculiar 60PKs. An older stellar population is presumably responsible for the redder annular colors of the amorphous galaxies. Scenario B predicts that the annular galaxy colors will evolve from blue to red as the morphology of the galaxies evolve from class III to class 0, due to an aging stellar population. According to scenario A the class 0 galaxies have relatively red annular colors because the galaxies were initially red, lenticular galaxies, while the class III galaxies are bluer because they were formerly later-type spirals with younger disk populations. The segregation of annular colors with respect to morphology is consistent with both scenarios.

6.2.4 Effective blue surface brightness

The global properties associated with the effective blue surface brightness of 60PKs are similar to that obtained for normal early type galaxies. Both scenarios incorporate an interaction/merger event as a key element, and according to numerical simulations the end product of such an event is a galaxy with the overall properties of an elliptical galaxy, thus qualitatively, both scenarios are consistent with the observed surface brightness of 60PKs. We would expect that the amorphous 60PKs become normal early type galaxies, once their nuclear activity ceases.

The trend of effective blue surface brightness ⟨SBe⟩ becoming fainter with increasing $L_{60\ \mu m}/L_B$ (Fig. 13) for the 60PKs is exactly reverse of that found for optically selected normal spiral galaxies (Phillipps & Disney 1988), and blue irregulars (Hunter *et al.* 1989). This is presumably attributed to the fact that the 60PKs have centrally concentrated dust that is heated by a central luminosity source (an active nucleus and/or starburst), while normal spirals have dust which is intimately related to star-forming regions located throughout their disks.

7. CONCLUSIONS

We have adopted a morphological classification scheme to describe the optical appearance of 60PKs. The four classes, amorphous (class 0), amorphous with features (class I), spirals (class II), and peculiar (class III), contain 18%, 42%, 9%, 31% of our sample, respectively. We have inspected the relationship of optical morphology to many other properties of 60PKs. Along the morphological sequence III–I–0 the nuclear activity tends to change from starburst to Seyfert 2 to Seyfert 1; the FIR colors become warmer, the FIR-to-blue luminosity ratio decreases, the

optical colors of the outer regions (excluding the nucleus) tend to become redder, and the effective blue surface brightness tends to increase. In Paper III we present a multivariate analysis to determine the relative importance of morphological class and nuclear-activity type for producing the strongest segregation of observable properties. The morphological properties of 60PKs and their dependence on manifestations of nuclear activity strongly suggest that the 60PK phenomenon is due to galaxy interactions. Such interactions would be responsible for funneling gas to the center of the galaxy and, with few exceptions, erasing any existing spiral structure. The cases of 60PKs whose spiral structure survived an interaction strong enough to trigger nuclear activity are in the minority. We have proposed two extreme scenarios (A and B) to explain the morphological classification scheme adopted for 60PKs and its relation to interactions and nuclear activity. Scenario A attributes the morphological differences among 60PKs to differences in the precursor galaxies, allowing no abrupt evolution from one morphology to another during a 60PK phase, though such evolution may occur progressively if the 60PK phenomenon is a recurrent one. Scenario B proposes an evolution through classes III, I, and 0 during a single 60PK event and does not account for class II. While both scenarios can equally well explain the trends of dimensionless quantities such as luminosity ratios or colors with morphological class, scenario B is more contrived in that it would also have to explain a strong evolution in the sense of decreasing optical luminosity, as well as optical size along the evolutionary sequence III–I–0, which cannot be reconciled with a simultaneous increase in optical surface brightness. It therefore seems that these latter properties are at least partly intrinsic to the precursor galaxies. The properties of 60PKs are therefore best explained by a mixture of scenarios A and B, with morphologically different precursor galaxies, possible morphological evolution during the 60PK phase, and one or more 60PK phases which are not expected to outlast the dust-obscured nuclear phase. This is certainly consistent with an estimated lifetime of the 60PK phase of a few times 10^8 yr assuming that any 60 μm selected galaxy can become a 60PK once, and a shorter lifetime in the case of recurrency (Paper I). Examples of morphologically different precursors are the merging of two spiral galaxies of comparable mass, the end product of which would be an elliptical galaxy (scenario B like), and a lenticular galaxy that recurrently accretes a much smaller gas-rich companion (scenario A like). This leaves open a whole variety of possible precursors of 60PKs, including elliptical and disk galaxies, as well as dwarf and giant galaxies. We will further address the nature of the precursors with an analysis of the surface brightness profiles (Paper IV) and an inspection of the environment of 60PKs (Paper V). We conclude that the 60PK phenomenon does not appear to be restricted to a particular class of galaxies, but can result from any interaction involving at least one gas-rich object and strong enough to funnel gas to the central region and create a dominant central source. The scarcity of 60PKs is due to the short lifetime of this phenomenon.

We gratefully acknowledge CTIO and Yale for the generous allocation of telescope time which allowed completion of this project. We thank the entire staff at CTIO for their excellent support of the observations. It is with great pleasure that C.A.H. acknowledges her thesis advisor J. P. Vader for her constant encouragement, direction, and friendship during the course of this dissertation project. C.A.H. would also like to thank Gary Da Costa for many helpful discussions on photometric reduction techniques, and J. A. Frogel, M. M. De Robertis, and A. Oemler for reading and commenting on earlier versions of her thesis manuscript. This research has been supported in part by NASA Grant No. JPL 958027 to J.P.V.

APPENDIX: COMMENTS ON INDIVIDUAL GALAXIES THAT PEAK NEAR 60 μm

00160-0719. This galaxy morphologically resembles a typical S0 galaxy, it is almost perfectly round with no observable features on optical broadband frames or on digitally enhanced color maps. A small detectable radio flux at 6 cm of ~0.9 mJy has been observed for this galaxy.

00198-7926. A large tail with an almost 90° bend, extends to the northwest of the main body of this very peculiar galaxy. A contour plot suggests that either a second nucleus or a large extranuclear region of star formation is present [Fig. 15(a)]. A masked B image, and a $B-R$ color map reveal many knots which are presumably H II regions embedded in the tails of this galaxy.

00344-3349 (ESO 350-G38). Three nuclei are clearly visible in this peculiar galaxy [Fig. 15(b)]. Spectra of the nuclei confirm that they are all at the same distance (Paper I), and all three nuclei have emission lines characteristic of H II regionlike galaxies. Magnitudes for the individual nuclei [labeled n1, n2, n3 in Fig. 15(b)] were measured within an aperture having a radius of 3 arcsec, and are given in Table 5. Nucleus n2 was assumed to be the dominant IRAS source in Paper I. A low surface brightness plume extends to the east of the galaxy and is clearly revealed on a masked frame. A ($B-R$) color map uncovers dust patches, along with low surface brightness plumes surrounding the galaxy.

00521-7054. This faint galaxy which lies behind the Small Magellanic Cloud, has peculiar isophotes that display a slight twisting and become rectangular as you reach the outer isophotes [Fig. 15(c)]. The galaxy has an asymmetrical, trapezoidal appearance presumably due to the tail feature uncovered in a $B-R$ color map. A detailed discussion of this object is given by Frogel & Elias (1987), who propose that this galaxy may be in the process of developing into a classical quasar. The 25–100 μm colors lie at the extreme warm end of the range occupied by objects with the highest degree of nuclear activity—namely Seyfert 1's and quasars.

01053+2147. Two tails extend straight out from the central nucleus at roughly 130° to each other. At the radio wavelengths of 6 and 20 cm this galaxy was found to be a weak radio emitter with fluxes of 1.0 and 4.8 mJy, respectively.

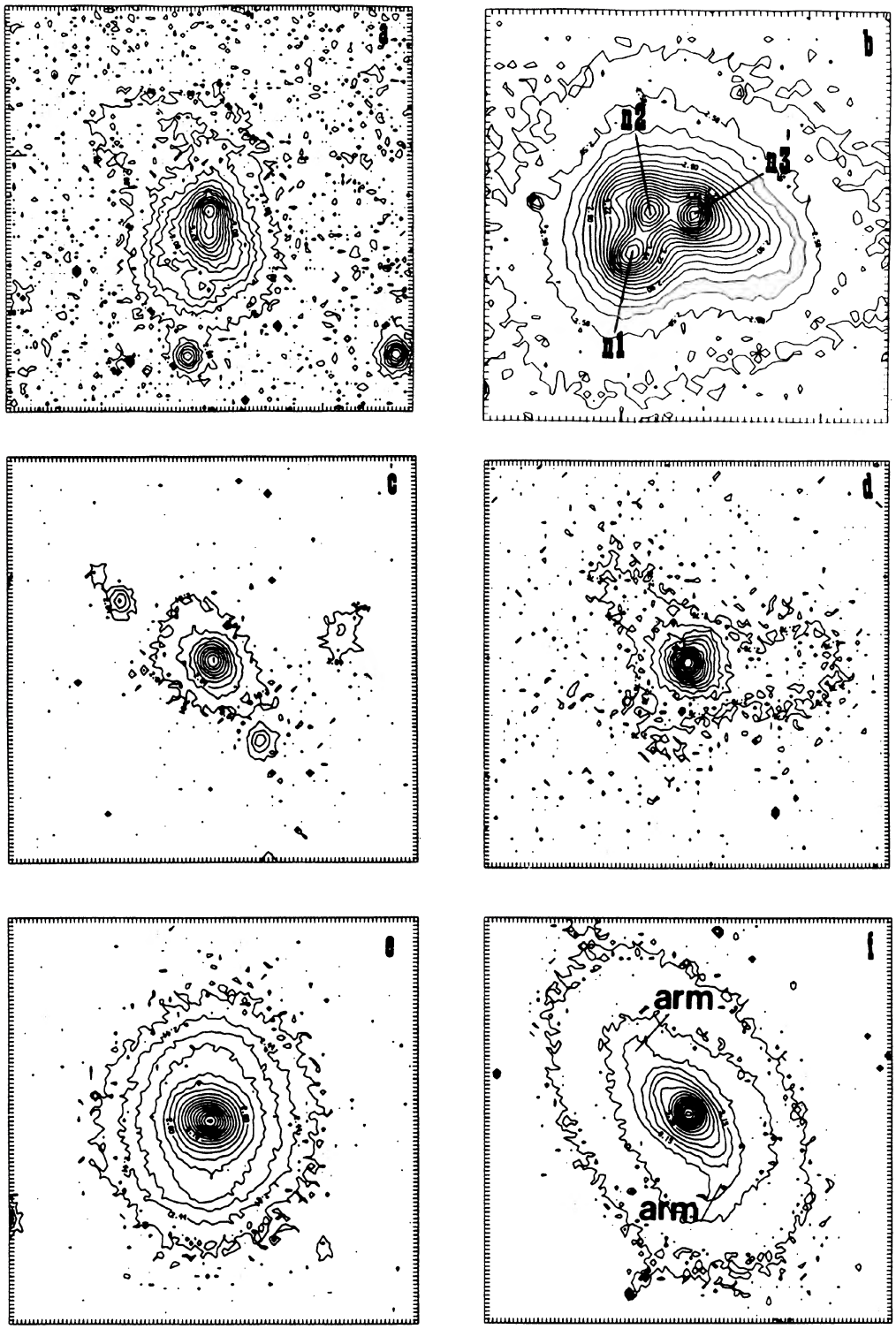

FIG. 15. For the contour plots ($a-z$) the spacing between tickmarks is 1 pixel (corresponding to 0.5 arcsec). North is to the top and east is to the right. (a) 00198-7926, 1100 s in R; (b) 00344-3345, average of three 450 s exposures in V; (c) 00521-7054 600, s in R; (d) 01053+2147, 1600 s in B; (e) 01413+0250, average of three 600 s exposures in R; (f) 02304+0012. 1800 s in B. (g) 03106-0254, 600 s in R; (h) 03344-2103, 1200 s in B; (i) 04385-0828, 600 s in V; (j) 05189-2524, 600 s in V; (k) 05530+0323, 600 s in R; (l) 06488+2731, 300 s in R. (m) 08007-6600, 1200 s in V; (n) 08170-1126, average of three 600 s exposures in B; (o) 14082+1347, 720 s in I; (p) 14167-7236, 1200 s in B; (q) 15295+2414, 2700 s in U filter; (r) 18333-6528, 600 s in B. (s) 19245-4140, average of three 450 s exposures in V; (t) 19370-0131, 1200 s in V; (u) 20210+1121, 900 s in B; (v) 20481-5715, average of three 600 s exposures in B; (w) 21062+1752, average of three 600 s exposures in R; (x) 23060+0505, 1200 s in R. (y) 23446+1519, 450 s in B; (z) 23547+1914, 1200 s in I.

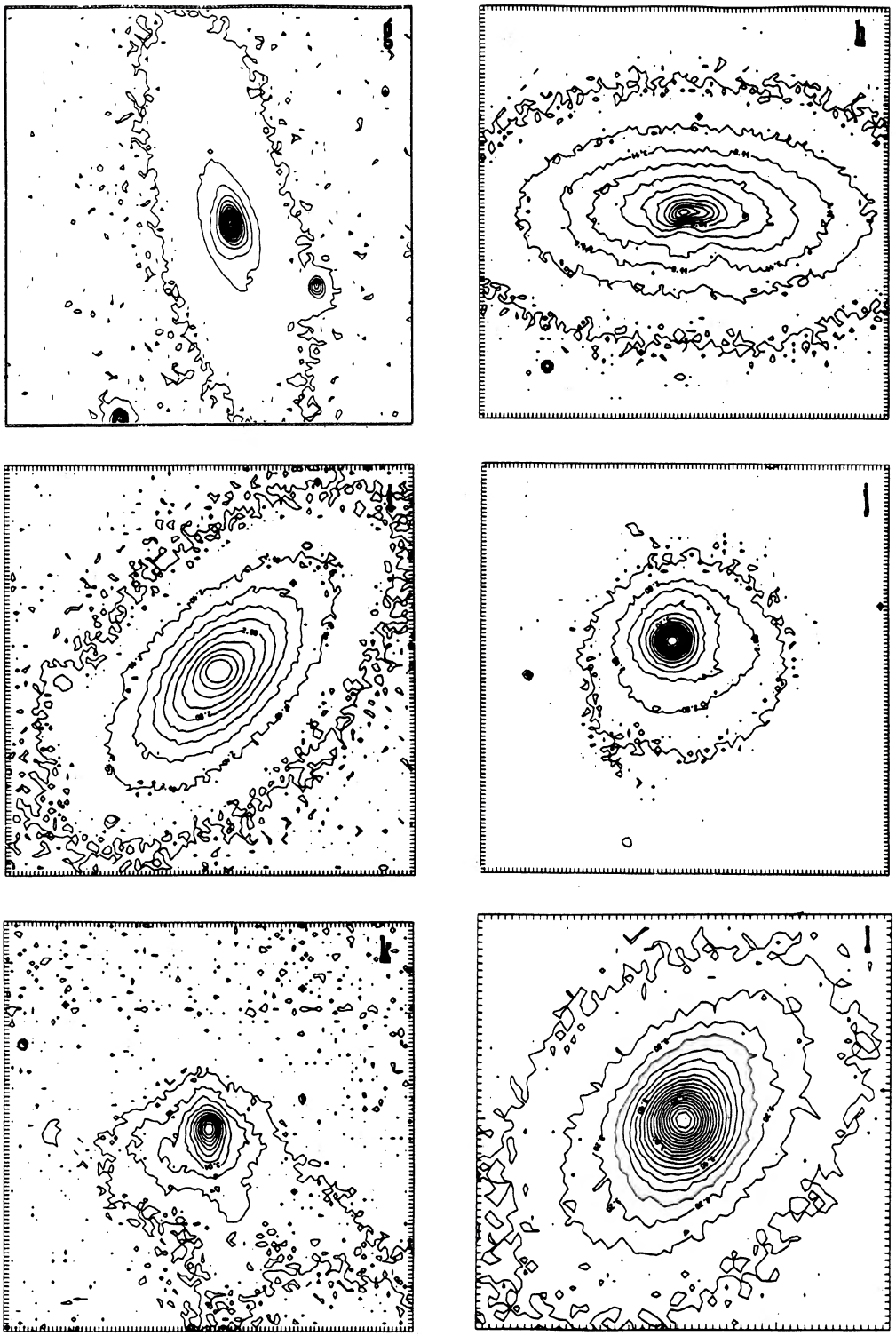

FIG. 15. (continued)

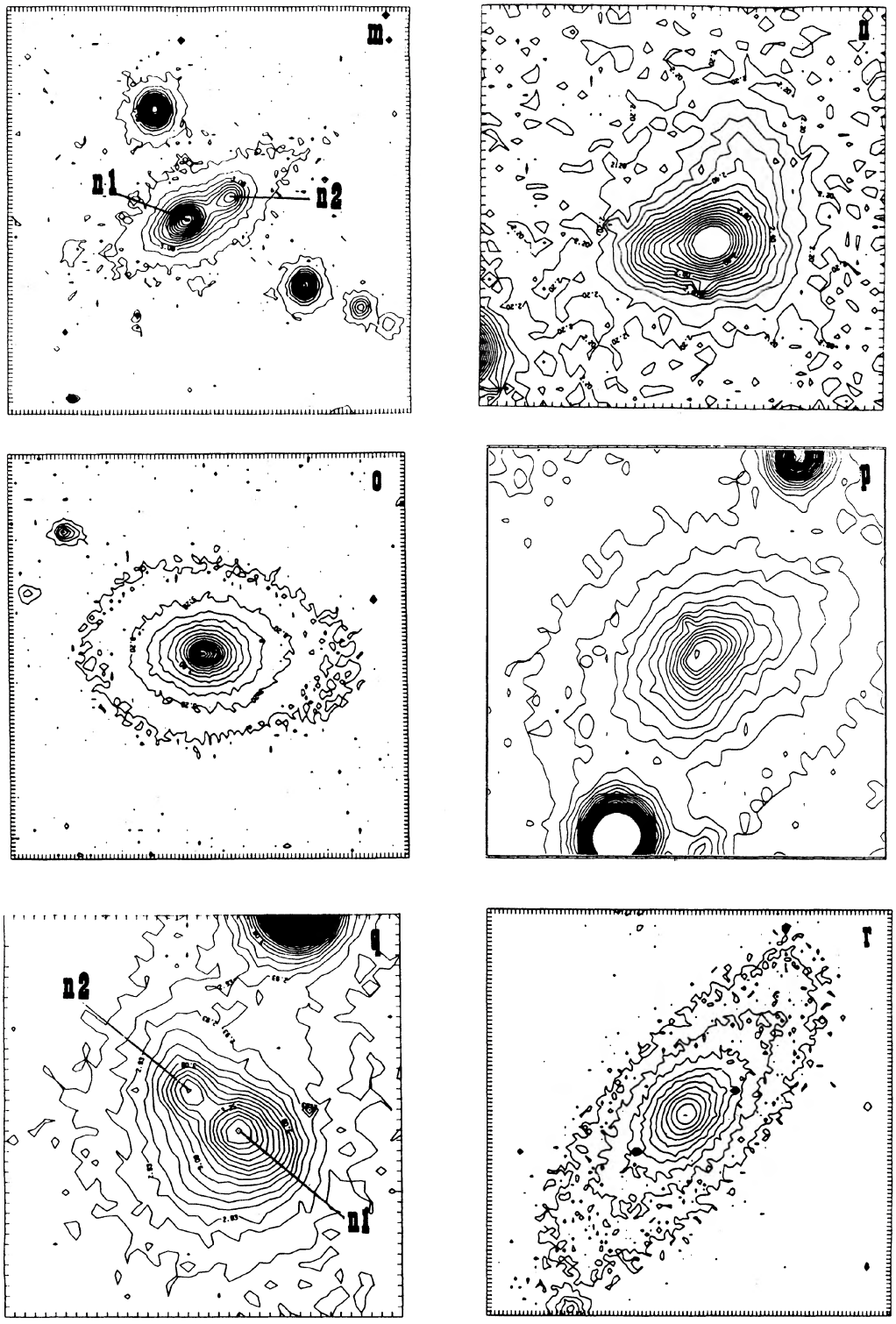

FIG. 15. (continued)

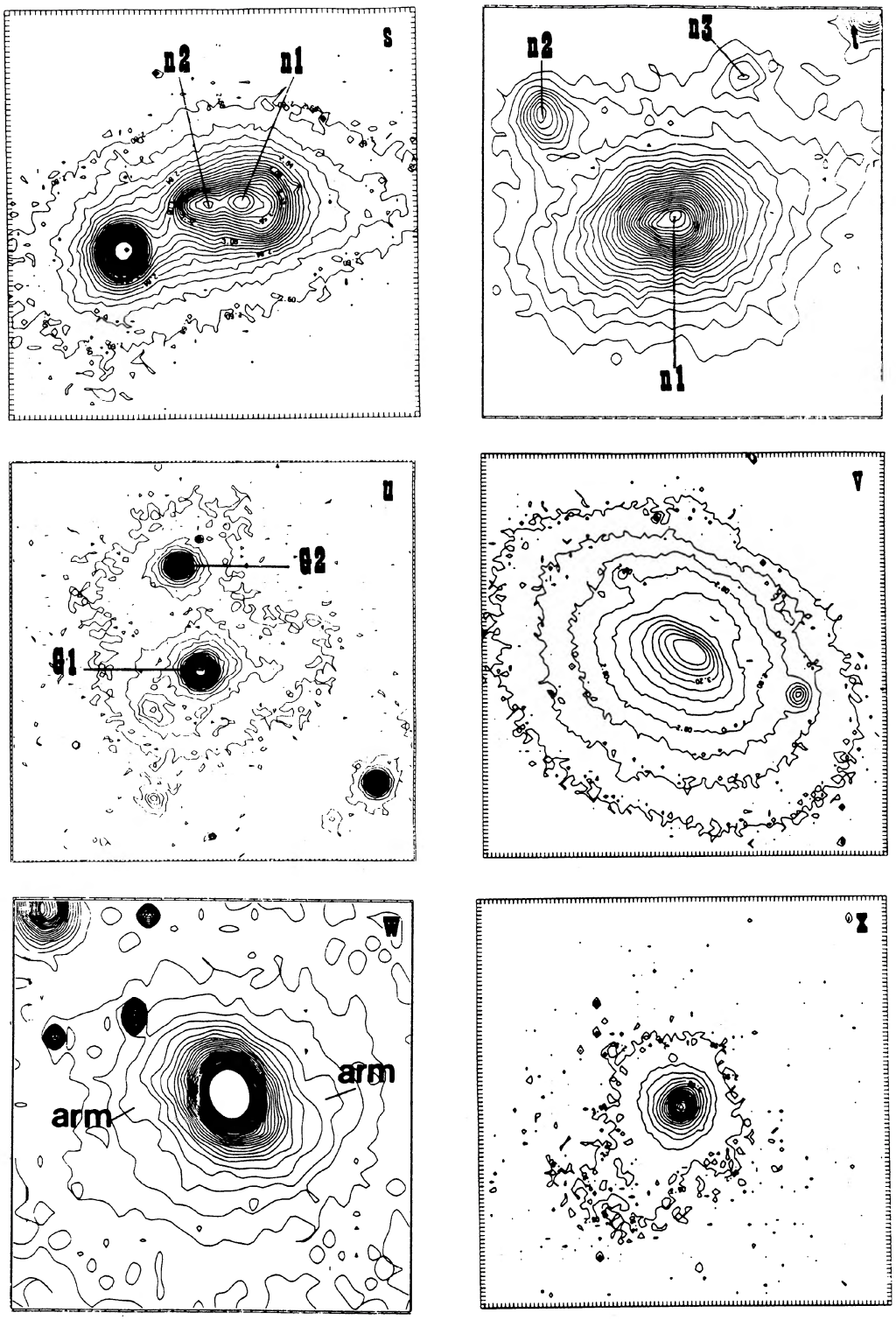

FIG. 15. (continued)

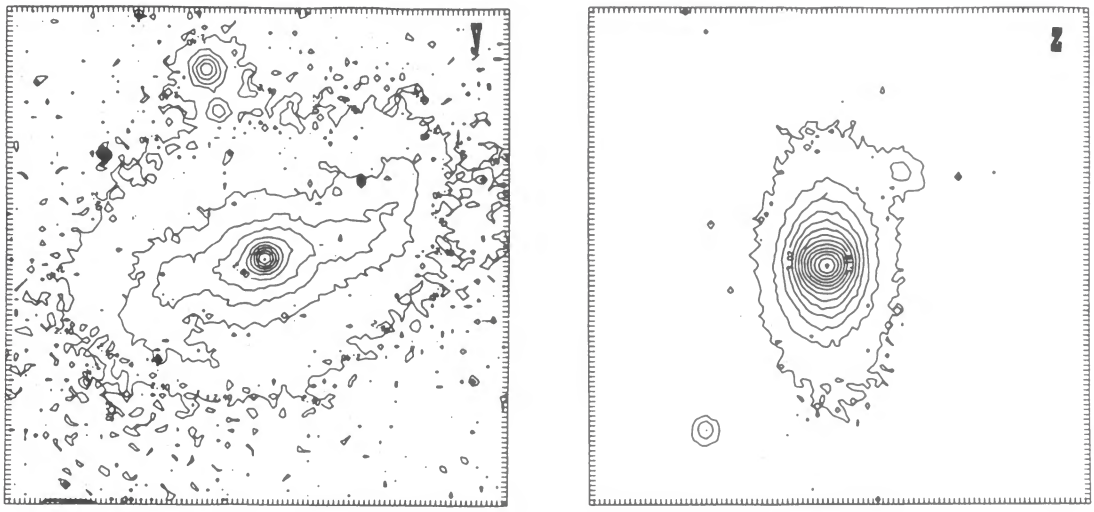

FIG. 15. (continued)

01072-0348. A ridgelike feature is visible in the NE portion of this IRAS galaxy on deep exposure CCD images. A masked frame reveals that there are bright arcs or shells surrounding this galaxy. The isophotes of the main body of the galaxy are smooth and regular. This is one of the stronger radio sources in our sample and it has a radio jet (Paper I). An apparently flat edge-on galaxy [labeled G2 in Fig. 1(e)] is located ~39 arcsec to the north of IRAS 01072 (labeled G1). We have not obtained a redshift for this edge-on galaxy G2. There are many fuzzy patches around IRAS 01072, but they are too faint for reliable photometry. We do not have enough information to determine if these faint patches are a group of background galaxies or faint companions or dwarf galaxies of IRAS 01072.

01413+0205 (Mkn 573). The isophotes for this amorphous galaxy are peculiar in the sense that the major axes of the ellipses in the central regions are aligned in an east–west direction, while the major axes of the outer isophotes appear to be aligned in a north–south direction [Fig. 15(e)]. Adjusting the contrast level so that the central portion of the galaxy is visible uncovers bright condensations (presumably of star formation) embedded in a ring that almost completely surrounds the galaxy, which is clearly visible on a masked image [Fig. 4(c)] of the galaxy. Mkn 573 is a relatively high ionization Seyfert 2 with narrow emission-line profiles that are believed to have resulted from optically thick emission-line clouds in high density regions (De Robertis & Osterbrock 1986). It contains a compact triple radio source that extends ~1 kpc (Ulvestad & Wilson 1984), and is nearly symmetric with the optical center.

01475-0740. Deep CCD frames and digitally enhanced frames show that this amorphous, nearly round galaxy lacks any distinguishing features. There are many faint patches surrounding this galaxy and we label them in Fig. 16. We estimate that the errors associated with $U-B$ and

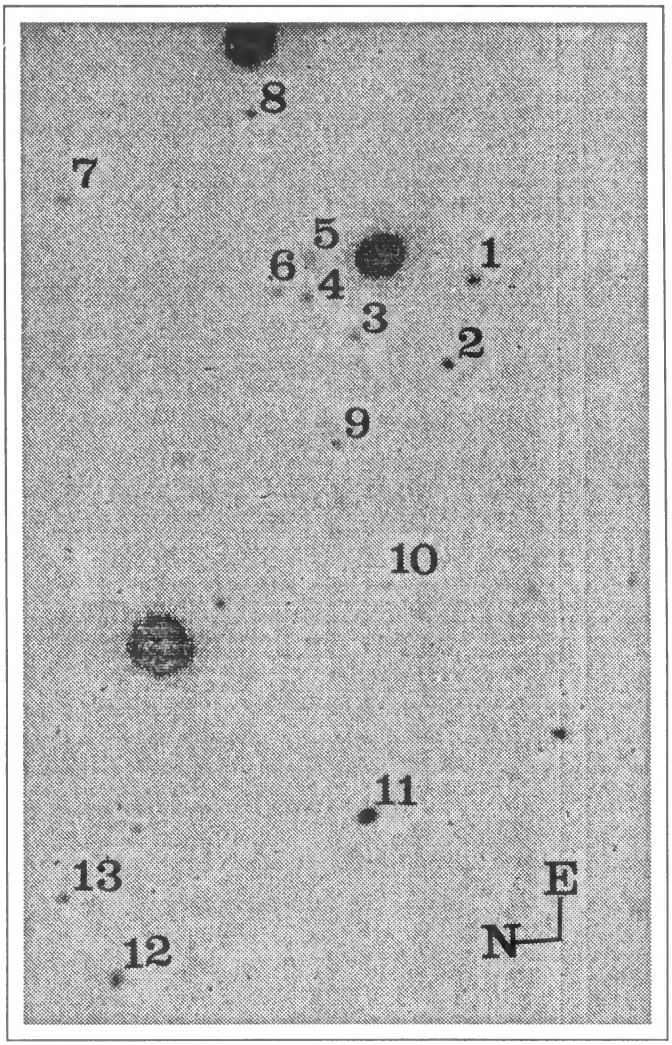

FIG. 16. CCD frame of a 3600 s exposure in *R* filter of IRAS 01475-0740, with faint patches that are believed to represent a background group of galaxies. Colors and apparent magnitudes are given for objects listed in Table 9.

TABLE 9. Photometry of faint objects surrounding 01475.

Object #	B	U-B	B-V	B-R
(1)	(2)	(3)	(4)	(5)
1	20.75	-0.44	0.94	1.37
2	20.91	-0.18	1.26	2.04
3	21.45	-0.67	0.77	0.94
4	21.47	-0.65	0.65	1.30
5	21.94	-0.41	1.58	2.54
6	31.36	0.35	0.58	0.14
7	21.48	-0.82	0.87	0.87
8	21.27	0.16	1.41	1.30
9	21.20	0.24	0.71	1.06
10	22.34	--	--	1.87
11	19.78	--	--	1.68
12	20.60	--	--	1.53
13	21.20	--	--	1.82

Notes to TABLE 9.

Col. (1) The identification number of object labeled in Fig. 16.
Col. (2) Apparent blue magnitude (not corrected for extinction nor redshift) of the faint object.
Col.(3)-(5) Apparent colors (U-B), (B-V), (B-R), respectively of faint objects. A dash indicates that a reliable magnitude could not be obtained with the data available.

$B-V$ colors of these faint patches to be roughly ± 0.20 and ± 0.10, respectively. The measured colors of these faint patches (Table 9) are too blue to be typical globular clusters. If these faint objects are companions at the same redshift as IRAS 01475, they are intrinsically faint (absolute blue magnitudes fainter than -13), and cover a radius of only ~ 40 kpc, making them unlikely candidates for companion dwarf galaxies. If, on the other hand, we assume that they are normal galaxies with absolute blue magnitudes of roughly -21 to -22, then their apparent magnitudes would place them at a redshift of $z \sim 0.4$, and they would cover a projected radius of ~ 1 Mpc, which is the typical size of a group of galaxies. We conclude that these faint patches surrounding IRAS 01475 have magnitudes and colors that are consistent with them being a background group of galaxies.

02304+0012 (UGC 2024). A faint halo surrounds the relatively large, bright nucleus of this disk galaxy. Small spiral arms emerge from the nucleus in the east and west directions, and are labeled on a contour plot [Fig. 15(f)] as arm1 and arm2, respectively. The spiral arms clearly extend into the faint outer halo of the galaxy. An unsharp masked image and $B-R$ color image reveals many knots, and dust patches.

02530+0211. A faint, fuzzy tail-like feature is visible to the SW of the main body of this amorphous galaxy. The isophotes are regular and smooth. A masked image reveals inner shell-like features within this galaxy [Fig. 3(d)].

03106-0254. This galaxy looks like an amorphous disk galaxy without spiral arms [Fig. 15(g)]. There appears to be dust surrounding the central bulge. A masked image clearly reveals a central ring surrounding the nucleus.

03344-2103 (NGC 1377). This galaxy looks normal on deep exposure CCD images, however when one examines a contour plot an interesting feature is revealed, namely an indentation in the southern portion of the central region gives rise to the kidney-bean appearance of the inner isophotes of this galaxy [Fig. 15(h)]. A $B-R$ color map [Fig. 4(e)] reveals a central dust patch along the minor axis direction, corresponding to the "indented" region in the contour plot of the broadband B CCD image.

04259-0440. This amorphous galaxy looks like a typical S0 galaxy on deep exposure CCD frames. Shells are visible on a masked image of this galaxy. The serendipitous discovery of a companion galaxy on Hα images (Paper III), has given us the opportunity to examine optical properties of the apparent "companion." This companion appears almost stellar with no nebulosity apparent on the CCD images, but a radial profile reveals that it has extended structure. We have labeled this probable companion G2 in Fig. 1(i).

04385-0254. A deep CCD image of this galaxy does not reveal any peculiar characteristics in this galaxy. A contour plot gives no indication of structure as the isophotes are smooth, regular ellipses [Fig. 15(i)]. An unsharp masked image however uncovers some interesting features: two bright condensations (presumably H II regions) on either side of the nucleus, which is suggestive of a bar, as galactic bars typically have H II regions at either end; and an arc extending from this barlike feature almost completely encompasses the central nucleus. This galaxy was detected at 6 and 20 cm with corresponding fluxes of 11.9 and 14.3 mJy, respectively.

05189-2524. An off-center nucleus is visible in deep exposure CCD frames of this amorphous galaxy [Fig. 15(j)]. The outer part of this galaxy appears distorted, with ridges. A masked image uncovers a very low surface brightness tail which forms an arc surrounding the galaxy. This galaxy is one of the ultraluminous FIR galaxies discussed in detail by Sanders *et al.* (1988a,b), and has been detected in the radio at 6 and 20 cm with fluxes of 12.7 and 28.3 mJy, respectively.

05530+0323 (II Zw 40). This peculiar galaxy is a well-studied blue compact dwarf galaxy, and is a prototype extragalactic H II region (Baldwin *et al.* 1982, Brinks 1988). The main body of the galaxy displays elliptical isophotes with an off-center nucleus, and a fainter second nucleus directly south of the central nucleus [Fig. 15(k)]. There are two long tails or plumes extending to the S and SE of the main body of the galaxy in which are embedded numerous knots. In addition there is a low surface brightness feature which extends in the western direction from the galaxy. A color map reveals dust patches and areas of presumably enhanced star formation. This galaxy has a large infrared excess and extended radio continuum emission with a flat spectral index (Jaffe *et al.* 1978), presumably of nonthermal origin.

05570-8123. This amorphous galaxy has regular, smooth isophotes. Unsharp masked images and two-color maps do not reveal any additional structure.

06097+7103 (Mkn 3). This well-studied galaxy was not observed by us, but it has been discussed in detail by others (e.g., Neff & Ulvestad 1988). It has a small broadline region < 1 pc and narrow-line region of ~ 1 kpc in radius. It is a strong double radio source, that is one of the strongest

for Seyfert galaxies, and does not coincide and is asymmetric with respect to the optical nucleus. Each component of the double radio source is slightly extended and separated by ~1.5″ (~600 pc) (Wilson *et al.* 1980).

06457+7429 (Mkn 6). This well-known galaxy was not observed by us, but it has been discussed by others (e.g., Neff & Ulvestad 1988). It is a strong double radio source with components separated by ~1″ (570 pc) at 6 cm (Ulvestad *et al.* 1981).

06488+2731 (MCG+05-16-010). This amorphous galaxy has smooth, very elongated elliptical isophotes [Fig. 15(l)]. Deep exposure CCD frames reveal a low surface brightness envelope surrounding the galaxy, and a faint tail or plume extending from the galaxy. A ($B-R$) two-color frame uncovers dust patches, and shells or arcs surrounding the main body of the galaxy. Very low surface brightness plumes or tails covering a large area on the frame become apparent in the color images.

08007-6600. The two nuclei in this galaxy are almost circular, and possess regular, smooth isophotes [labeled n1 and n2 in Fig. 15(m)], and have a projected separation of 6.1 arcsec (~5 kpc). Faint, straight, narrow jetlike plumes extend in the NE and SW direction, along the same line as the nuclei. Nucleus n1 has been identified as the IRAS source (component A in Paper I).

08014+0515 (Mkn 1210). This almost circular, amorphous galaxy morphologically resembles a typical elliptical galaxy. Masked frames display arcs or shells surrounding the main body of the galaxy. This galaxy has been detected at 22 and 5 GHz, and at these frequencies the flux is 17 ±2.3 and 66±9 mJy, respectively (Malkan 1990).

08170-1126. This peculiar galaxy contains two separate nuclei, one (n1) of which is ~1 mag brighter in the blue than the other (n2). A low surface brightness tail extends toward the north, and appears to emanate from nucleus n1 [Fig. 15(n)]. At 6 cm this galaxy remains unresolved with a flux of 3.6 mJy, but at 20 cm it is slightly resolved with a FWHM of between 1 and 2 beam diam with a flux of 23.8 mJy. Nucleus n1 has been identified as the IRAS source (component A in Paper I).

08321+6624 (Mkn 93). This previously identified galaxy was not observed by us, but it has been discussed by Mazzarella & Balzano (1986).

09497-0122 (Mkn 1239). This amorphous galaxy has very smooth, regular isophotes, and resembles an elliptical galaxy. Careful examination of masked frames and two-color maps do not reveal any low surface brightness features nor dust patches. This galaxy has one of the warmest FIR colors in our sample, and has an optical-to-near-infrared spectral energy distribution indicative of hot dust (~1000 K) and/or synchrotron radiation (Rafanelli & Bonoli 1984, Rudy *et al.* 1982).

10567-3323. A low surface brightness feature extends to the east of this amorphous galaxy. Digital enhancement reveals three bright knots within this extension. This galaxy was detected at 6 cm with a flux of 2.0 mJy, but not at 20 cm, and it has been previously discussed in detail by Heisler *et al.* (1989a).

12540+5708 (Mkn 231). This very extraordinary galaxy was not observed by us, but it has been extensively studied by others (e.g., Sanders *et al.* 1988a,b). It is a FIR-ultraluminous galaxy believed to be in an advanced stage of a merger. Mkn 231 has a strong, nonthermal nuclear source surrounded by an unusually young, stellar population (Hamilton & Keel 1987). The observed x-ray luminosity is lower than that found for Seyferts 1's and quasars, with similar bolometric luminosities (Eales & Arnaud 1988), but comparable to those of Seyfert 2's.

13329-3402 (MCG-6-30-15, ESO 383-G35). This galaxy resembles a very elongated lenticular galaxy, with smooth, regular isophotes and a bright, circular nucleus. The bright source south of the nucleus, within the galaxy, is a foreground star. The detailed study by Pineda *et al.* (1980) shows that it has a typical Seyfert 1 spectrum. It is an unresolved radio source at 6 and 20 cm with a size <80 pc (Ulvestad & Wilson 1984). There are no features apparent on the deep exposure CCD images, but digitally enhanced images reveal elongated, almost straight features on either side of the nucleus. These features may be indicative of a nearby edge-on disk, although no spiral structure is evident.

13370-3123 (NGC 5253). This well-studied galaxy has been classified as a prototype amorphous galaxy (Sandage & Brucato 1979). There are many bright knots embedded in what appears to be a lenticular galaxy. A ($B-R$) two-color map better illustrates these bright knots, and also reveals dust patches and lanes in this galaxy.

The optical spectrum shows high excitation emission lines and a blue optical continuum, with a remarkably flat spectral index ($\alpha=-0.25$). These properties are indicative of very young, hot stars, and gas with negligible internal reddening and normal abundances (Osmer *et al.* 1974). A molecular hydrogen mass of $\approx 10^6 \mathcal{M}_\odot$ has been deduced from CO measurements (Wikland & Henkel 1989). The gas content is small and in the form of neutral and ionized hydrogen, which is typical for early type galaxies (Knapp *et al.* 1989, Sadler *et al.* 1985). An unresolved 6″ diam emission region in the near infrared has colors indicative of dust with temperatures up to 1000 K (Glass 1973). The near-infrared emission lines indicate the presence of the highest excitation gas observed thus far in starburst galaxies with a temperature of ~50 000 K ionizing spectrum, equivalent to an average spectral type of 04 (Moorwood & Glass 1982), which together with the compact size suggest that a very young compact starburst nucleus is responsible for the very hot dust (Roche 1987). This near-infrared line-emitting region is completely obscured visually ($A_v>8$ mag), and is estimated to contain a central source with a luminosity comparable to that of II Zw 40 (Aitken *et al.* 1982). Such a nucleus is short lived which is consistent with the suggestion that the 60PKs are in a rapid phase of evolution. The peculiar morphology and enhanced star formation are strongly suggestive of a recent accretion event, presumably as a result of a recent encounter ($<10^9$ yr) with the nearby gas-rich spiral M83 (van den Bergh 1980).

13452-4155 (ESO 325-IG22). The *IRAS Point Source Catalogue* (Second Version) flagged this galaxy as a point source within a complex field. As evident on optical CCD

images [Figs. 2(k) and 4(j)] a bright foreground star lies very close to this IRAS galaxy, with the result that IRAS 13452 is contaminated by rings due to internal reflections in the telescope from this bright star. Three galaxies lie within the IRAS position error ellipse, but spectra were obtained for only the brightest one (identified as the IRAS source in Paper I). This galaxy appears to be a peculiar disk galaxy and we label it as G1 in Fig. 2(k). A masked image reveals a long tail extending in the north direction from this galaxy [Fig. 4(j)]. This peculiar galaxy is resolved at 6 and 20 cm with a FWHM of ~2 and 7 arcsec, respectively, and fluxes of 9.9 and 38.1 mJy, respectively. The morphology of the other two objects (labeled as G2 and G3) is less clear—they have no peculiar characteristics.

13536+1836 (Mkn 463). This well-studied double-nucleus galaxy (e.g., Kollatschny & Fricke 1984, Hutchings & Neff 1988, Neff & Ulvestad 1988, Mazzarella *et al.* 1991) has three low surface brightness tails as revealed by deep exposure CCD images. The optical nuclei are separated by approximately 4 arcsec corresponding to ~4 kpc. Each nucleus has optical emission lines typical of Seyfert type 2 galaxies, but when viewed in polarized light this galaxy has the spectrum of a Seyfert 1 (Miller & Goodrich 1987). A two-color map uncovers many bright knots, arcs, and dust patches. This galaxy has a double radio source separated by 1.3″ at 6 cm (Ulvestad & Wilson 1984).

14082+1347 (CGCG Zwicky). Shells surround the amorphous main body of this galaxy [Fig. 15(o)], and are clearly visible in a masked frame [Fig. 4(l)]. The shells around this galaxy are the most prominent of the shell galaxies in our FIR-selected sample.

14167-7236. This amorphous galaxy is located in a very crowded field. It has a relatively large, bright nucleus which appears to be off center with respect to its fainter surrounding halo [Fig. 15(p)]. The two bright objects on either side of the galaxy are foreground stars. A masked image reveals a plume extending to the SW of the main body of the galaxy.

15295+2414 (3C 321). The double nuclei of this well-studied galaxy (e.g., Filippenko 1987) have optical spectra characteristic of Seyfert type 2 galaxies. The nuclei are separated by 3.1 arcsec, corresponding to a linear projected separation of ~6 kpc [Fig. 15(q)]. The brighter nucleus n1 is a flat-spectrum compact radio source with a one-sided jet containing a steep spectrum radio knot near the second nucleus (Kuhr *et al.* 1981). A low surface brightness tail extends to the south of the galaxy, and the object to the north is a foreground star. 3C 321 is the most distant galaxy among the previously identified 60PKs.

16380-8120 (ESO 023 IG03). There are two galaxies located within 6.20 arcsec of each other within the IRAS error ellipse in position. The galaxy to the west appears to be a disk galaxy and the smaller galaxy to the east appears to be an early type or amorphous galaxy, we have labeled these as G1 and G2, respectively, in Fig. 4(m). This masked image reveals that G1 contains a tidal tail emerging straight out in the southern direction and another tail with a slight warp extending in the northern direction. The brighter galaxy G1 was assumed to be the IRAS source in Paper I. A redshift for the small apparently nearby galaxy (G2) was not obtained, but in light of the results of our Hα emission mapping program (Paper III), we believe it lies at approximately the same distance as the disk galaxy, and may be a satellite or companion galaxy. G2 exhibits no structure in optical broadband images or digitally enhanced images, but it has an integrated Hα flux that is at least four times larger than G1, and is possibly the major contributor to the IRAS emission (this is discussed in more detail in Paper III of this series).

18333-6528 (ESO 103-G35). This galaxy has smooth, regular, elongated isophotes [Fig. 15(r)], and has drawn attention as the optical counterpart of a HEAO-A2 x-ray source (Phillips *et al.* 1979). These authors have suggested that it may be an S0 galaxy. The eccentricity of the isophotes is indicative of a disk galaxy, yet there is no evidence for spiral arms. This Seyfert 1 galaxy is among the warmest FIR emitters in the sample. It has a very high excitation emission-line spectrum similar to broadline radio galaxies, superposed on a red stellar continuum with absorption lines. There appears to be an amorphous satellite galaxy to the NW at a projected distance of ~30″.

19245-4140 (ESO 338-IG04, TOLOLO 19245). This is a well-studied blue compact galaxy (e.g., Iye *et al.* 1987). A contour plot of a deep exposure CCD image [Fig. 15(s)] suggests the presence of two nuclei separated by ~3.04 arcsec, labeled as n1 and n2, and an unsharp masked image clearly reveals the two nuclei, along with a bright arc to the east of the brighter nucleus n1 [Fig. 4(n)].

19370-0131. An apparent second nucleus or a tidal extension, labeled as n2, is visible to the NW of the central nucleus of IRAS 19370, labeled n1 [Fig. 15(t)]. There is also a fainter knot (possibly an H II region), labeled as n3, to the NE of n1. The central nucleus itself appears elongated in the E–W direction relative to the stellar profiles. Optically, this is one of the reddest galaxies in our sample. At radio wavelengths of 6 and 20 cm, this galaxy has fluxes of 5.4 and 15.5 mJy, respectively.

20210+1121. This IRAS source, labeled as G1 in Fig. 15(u), displays low surface brightness plumes. This is one of the strongest radio sources measured in the sample with flux densities at 6 and 20 cm of 15.9 and 44.5 mJy, respectively. There is an apparent companion (G2) ~7 arcsec to the north of the IRAS galaxy (G2) [with IRAS coordinates of $\alpha(1950)=20\ 21\ 02.1$, $\delta(1950)=11\ 21\ 49$]. The companion G2 is also a weak radio source with a flux at 6 cm of 1.4 mJy. An arc or tidal tail, within which a bright knot (k1) is embedded, extends in the SW direction from this IRAS galaxy, and a second bright knot (k2) is located east of IRAS 20210. We have also included a peculiar object in our CCD frame [Fig. 1(s)], labeled as G3, because this object may be interacting with the system IRAS 20210 and G2 (projected linear separation of approximately ~0.1 Mpc).

20253-8152. This amorphous galaxy has smooth, regular isophotes, and lacks any distinctive features even when carefully examined using digitally enhanced images.

20460+1925. This galaxy has the largest redshift

among the galaxies measured in our sample, and its bolometric luminosity of 7×10^{12} $L_{\odot}$, makes it one of the two most luminous galaxies known (Frogel *et al.* 1989). Optical spectra show line ratios characteristic of a Seyfert type 2, but the permitted and forbidden lines are broader than most other Seyfert 2's. In fact, it has been demonstrated that this galaxy has broad Paα lines characteristic of Seyfert 1 type galaxies (Hines 1991). This amorphous galaxy has smooth, regular isophotes with no visible structure even when examined using digitally enhanced images.

20481-5715 (IC 5063, PKS 20481). Numerous dust lanes are clearly visible in the NE section of this well-studied peculiar galaxy (e.g., Caldwell & Phillips 1981, Danziger *et al.* 1981). It has been previously classified as both an elliptical and an S0 galaxy. A contour plot of the original CCD image displays smooth, elliptical isophotes [Fig. 15(v)], while a masked image clearly delineates the dust lane structure, and reveals a peanut-shaped nucleus, which has been proposed to be the result of multiple nuclei (Heisler *et al.* 1989a). Our Hα imaging has indeed revealed that there are three nuclei (Heisler *et al.* 1989b), which is discussed in more detail in Paper III of this series. The radio source is weaker than for typical radio galaxies, but unusually strong for Seyfert galaxies. A 21 cm radio continuum map reveals an extended source ($\sim$8 kpc) coinciding with the optical center of the galaxy, and a small mass of ionized and neutral hydrogen which is characteristic of early type galaxies (Danziger *et al.* 1981). This galaxy has a very red near-infrared nuclear source ($K-L=2.1$) and a high polarization (17%), which requires a contribution from a nonthermal synchrotron source (Hough *et al.* 1987). The presence of an active nucleus is supported by a very high excitation emission-line spectrum (Bergeron *et al.* 1983).

21062+1725. This face-on galaxy has central smooth, regular isophotes with small faint spiral arms [Fig. 15(w)]. There are no dust patches or peculiar features evident on masked or two-color frames. At radio wavelengths of 6 and 20 cm this galaxy has fluxes of 2.0 and 4.3 mJy, respectively.

23060+0505. This faint galaxy is one of the more distant objects in the sample, and has been extensively studied by others (e.g., Hutchings & Neff 1988; Hill *et al.* 1987), who find bright knots embedded in the central body of the galaxy. Near-infrared spectroscopy has demonstrated that this galaxy has broad Paα lines characteristic of Seyfert 1 type galaxies (Hines 1991). A tidal tail or plume extends in the SW direction [Fig. 15(x)]. This source is unresolved at 6 cm but resolved at 20 cm with fluxes of 3.0 and 13.5 mJy, respectively.

23446+1519 (MCG+02-60-01). This galaxy is one of the few prominent spirals in the sample of 60PKs. The spiral arms appear to emanate from a barlike feature [Fig. 15(y)]. Similar to the few other spirals in our sample, a faint outer envelope surrounds the galaxy. Inspection of an unsharp masked frame reveals a low surface brightness tail extending from the eastern arm from the point at which the bar and the arm connect.

23547+1914. This galaxy has a smooth global light distribution with rather elongated isophotes [Fig. 15(z)]. A bright arc or shell feature (S1) lies along the minor axis direction, just north of the galaxy [Fig. 1(w)], while an unsharp masked image uncovers more shells [Fig. 3(l)], and an asymmetry in the central region, which may be due to a second nucleus.

REFERENCES

Adams, T. F. 1977, ApJS, 33, 19
Aitken, D. K., Roche, P. F., Allen, M. C., & Phillips, M. M. 1982, MNRAS, 199, 31P
Allen, C. W. 1973, Astrophysical Quantities, 3rd ed. (Athlone, London)
Armus, L., Heckman, T., & Miley, G. 1987, AJ, 94, 831
Athanassoula, E., & Bosma, A. 1985, ARA&A, 23, 147
Baldwin, J. A., Spinrad, H., & Terlevich, K. 1982, MNRAS, 198, 535
Barnes, J. E., & Hernquist, L. E. 1991, ApJ, 370, L65
Bergeron, J., Durret, F., & Bokensberg, A. 1983, A&A, 127, 322
Binggeli, B., Sandage, A., & Tarenghi, M. 1984, AJ, 89, 64
Bothun, G. D., Halpern, J. P., Lonsdale, C. J., Impey, C., & Schmitz, M. 1989, ApJS, 70, 271
Brinks, E., & Klein, U. 1988, MNRAS, 231, 63P
Burbidge, G. R., Burbidge, E. M., & Sandage, A. R. 1963, Rev. Mod. Phys., 35, 947
Burstein, D., & Heiles, C. 1982, AJ, 87, 1165
Caldwell, N., & Phillips, M. M. 1981, ApJ, 244, 447
Cousins, A. W. J. 1967a, MRAS, 81, 25
Cousins, A. W. J. 1967b, MRASSoAfrica, 35, 70
CTIO Observers Manual 1989
Danziger, I. J., Goss, W. M., & Wellington, K. J. 1981, MNRAS, 196, 845
de Grijp, M. H. K., Miley, G. K., Lub, J., & de Jong, T. 1985, Nature, 314, 240
de Jong, T., *et al.* 1984, ApJ, 278, L67
De Robertis, M. M. 1985, AJ, 90, 998
De Robertis, M. M., & Osterbrock, D. E. 1986, ApJ, 301, 727
Dressel, L. L. 1988, ApJ, 329, L69
Dupraz, C., & Combes, F. 1986, A&A, 166, 53
Eales, S. A., & Arnaud, K. A. 1988, ApJ, 324, 193
Ebneter, K., Djorgovski, S., & Davis, M. 1988, AJ, 95, 422
Fabian, A. C., Nulsen, P. E. J., & Stewart, G. C. 1980, Nature, 287, 613
Filippenko, A. V. 1987, in Observational Cosmology, IAU Symposium No. 124, edited by A. Hewitt, G. Burbidge, and L. Z. Fang, p. 761
Frogel, J. A., & Elias, J. H. 1987, ApJ, 313, L53
Frogel, J. A., Gillett, F. C., Terndrup, D. M., & Vader, J. P. 1989, ApJ, 343, 672
Gallagher, J. S., & Hunter, D. A. 1989, AJ, 98, 806
Glass, I. S. 1973, MNRAS, 164, 155
Goudfrooij, P., & de Grijp, M. H. K. 1990, preprint
Graham, J. A. 1982, PASP, 94, 244
Gunn, J. E. 1979, in Active Galactic Nuclei, edited by C. Hazard and S. Mitton (Cambridge University Press, Cambridge), p. 213
Hamilton, D., & Keel, W. C. 1987, ApJ, 321, 211
Heckman, T. M., Balick, B., & Sullivan, W. T. 1978, ApJ, 224, 745
Heckman, T. M., *et al.* 1986, ApJ, 311, 526
Heisler, C. A. 1991, Ph.D. thesis, Yale University, New Haven
Heisler, C. A., & Vader, J. P. 1993, in preparation (Paper III)
Heisler, C. A., & Vader, J. P. 1993, in preparation (Paper IV)
Heisler, C. A., & Vader, J. P. 1989b, BAAS, 20, 1000

Heisler, C. A., Vader, J. P., & Frogel, J. A. 1989a, in Active Galactic Nuclei, IAU Symposium No. 134, edited by D. E. Osterbrock and J. S. Miller (Kluwer,), p. 55
Heisler, C. A., Vader, J. P., & Frogel, J. A. 1989c, AJ, 98, 986
Hernquist, L. 1989, Nature, 340, 687
Hernquist, L., & Quinn, P. J. 1989, ApJ, 342, 1
Hernquist, L., & Quinn, P. J. 1988, ApJ, 331, 682
Hill, G. J., Wynn-Williams, C. G., & Becklin, E. E 1987, ApJ, 316, L11
Hines, D. C. 1991, ApJ, 374, L9
Hough, J. H., Brindle, C., Axon, D. J., Bailey, J., & Sparks, W. B. 1987, MNRAS, 224, 1013
Hunter, D. A., Gallagher, J. S., Rice, W. C., & Gillett, F. C. 1989, ApJ, 336, 152
Hutchings, J. B., & Neff, S. G. 1988, AJ, 96, 1575
IRAS Catalogues and Atlases: Explanatory Supplement 1985, edited by C. A. Beichman, G. Neugebauer, H. J. Habing, P. E. Clegg, and T. J. Chester (GPO, Washington, DC)
IRAS Point Source Catalogue, 2nd Version 1988, Joint IRAS Science Working Group, (GPO, Washington, D.C.)
Iye, M., Ulrich, M.-H., & Peimbert, M. 1987, A&A, 186, 84
Jaffe, W. J., Perola, G. C., & Tarenghi, M. 1978, ApJ, 224, 808
Joseph, R. D. 1986, in Light on Dark Matter, edited by F. P Israel (Reidel, Dordrecht), p. 447
Joseph, R. D., Wright, G. S., James, P. A., & McLean, I. S. 1988, MNRAS, 232, 7P
Khachikian, E. Ye., & Weedman, D. W. 1971, Afz, 7, 389
Knapp, G. R., Guhathakurta, P., Kim, D.-W., & Jura, M. 1989, ApJS, 70, 329
Kollatschny, W., & Fricke, K. 1984, in Proceedings of 4th International Ultraviolet Explorer Conference, edited by E. Rolfe and B. Battrick, ESA Spec. Publ., ESA SP-218, p. 91
Kormendy, J. 1979, ApJ, 227, 714
Krolik, J. H., & Lepp, S. L. 1989, ApJ, 347, 179
Kuhr, H., Pauliny-Toth, I. I. K., Witzel, A., & Schmidt, J. 1981, AJ, 86, 854
Landolt, A. U. 1983, AJ, 88, 439
Larson, R. B., & Tinsley, B. M. 1978, ApJ, 219, 46
Lonsdale, C. J., Persson, S. E., & Mathews, K. 1984, ApJ, 287, 95
MacKenty, J. W. 1990, ApJS, 72, 231
Malin, D. F. 1977, AASPhB, 16, 10
Malin, D. F., & Carter, D. 1983, ApJ, 274, 534
Malkan, M. 1990, private communication
Mazzarella, J. M., Gaume, R. A., Soifer, B. T., Graham, J. R., Neugebauer, G., & Matthews, K. 1991, AJ, 102, 1241
Mazzarella, J. M., & Balzano, V. A. 1986, ApJS, 62, 751
Miley, G. K., Neugebauer, G., Clegg, P. E., Harris, S., Rowan-Robinson, M., Soifer, B. T., & Young, E. 1984, ApJ, 278, L79
Miller, J. S., & Goodrich, B. F. 1990, ApJ, 355, 456
Miller, J. S., & Goodrich, B. F. 1987, BAAS, 19, 695
Moorwood, A. F. M., & Glass, I. S. 1982, A&A, 115, 84
Neff, S. G., & Ulvestad, J. S. 1988, AJ, 96, 841
Neugebauer, G., *et al.* 1984, ApJ, 278, L83
Noguchi, M. 1988a, A&A, 201, 37
Noguchi, M. 1988b, A&A, 203, 259
Noguchi, M. 1987, MNRAS, 228, 635
Norman, C., & Scoville, N. Z. 1988, ApJ, 332, 124
Osmer, P. S., Smith, M. G., & Weedman, D. W. 1974, ApJ, 192, 279
Pence, W. 1976, ApJ, 203, 39
Phillipps, S., & Disney, M. 1988, MNRAS, 231, 359
Phillips, M. M., Feldman, F. R., Marshall, F. E., & Wamsteker, W. 1979, A&A, 76, L14
Pineda, F. J., Delvaille, J. P., Grindlay, J. E., & Schnopper, H. W. 1980, AJ, 237, 414
Rafanelli, P., & Bonoli, C. 1984, A&A, 131, 106
Roche, P. L. F. 1987, in Polycyclic Aromatic Hydrocarbons and Astrophysics, edited by A. Leger, L. d'Hendecourt, and N. Boccara, p. 307
Rudy, R. J., LeVan, P. D., & Rodriquez-Spinoza, J. M. 1982, AJ, 87, 598
Sadler, E. M., & Gerhard, O. E. 1985, MNRAS, 214, 177
Salzer, J. J., MacAlpine, G. M., & Boroson, T. A. 1989, ApJS, 70, 447
Sandage, A. 1961, in Hubble Atlas of Galaxies (Carnegie Institute, Washington)
Sandage, A. 1983, in Internal Kinematics and Dynamics of Galaxies, IAU Symposium No. 100, edited by E. Athanassoula (Reidel, Dordrecht), p. 367
Sandage, A., & Brucato, R. 1979, AJ, 84, 470
Sanders, D. B., Scoville, N. Z., Young, J. S., Soifer, B. T., Schloerb, F. P., Rice, W. L., & Danielson, G. E. 1986, ApJ, 305, L45
Sanders, D. B., Soifer, B. T., Elias, J. H., Madore, B. F., Matthews, K., Neugebauer, B., & Scoville, N. Z. 1988a, ApJ, 325, 74
Sanders, D. B., Soifer, B. T., Elias, J. H., Neugebauer, G., & Matthews, K. 1988b, ApJ, 328, L35
Schombert, J. M., & Wallin, J. F. 1987, AJ, 94, 300
Schweizer, F. 1980, ApJ, 237, 303
Schweizer, F., & Ford, W. K. Jr. 1985, in New Aspects of Galaxy Photometry, edited by J. L. Nieto (Springer, Berlin), p. 149
Scoville, N. Z., Sanders, D. B., Sargent, A. I., Soifer, B. T., & Tinney, C. G. 1989, ApJ, 345, L25
Simkin, S. M., Su, H. J., & Schwarz, M. P. 1980, ApJ, 237, 404
Soifer, B. T., *et al.* 1987a, ApJ, 320, 238
Sparks, W. B., Wall, J. V., Thorne, D. J., Jordan, P. R., van Breda, I. B., Rudd, P. J., & Jorgensen, H. E. 1985, MNRAS, 217, 87
Telesco, C. M., Decher, R., & Gatley, I. 1985, ApJ, 299, 896
Telesco, C. M., & Harper, D. A. 1980, ApJ, 235, 392
Thomson, R. C. 1991, MNRAS, 253, 256
Thronson, H. A., & Bally, J. 1987, ApJ, 319, L63
Toomre, A., & Toomre, J. 1972, ApJ, 178, 623
Tully, R. B. 1988, in Nearby Galaxies Catalog (Cambridge University Press, Cambridge)
Ulvestad, J. S., & Wilson, A. S. 1984, ApJ, 278, 544
Ulvestad, J. S., Wilson, A. S., & Sramek, R. A. 1981, ApJ, 247, 419
Vader, J. P. 1986, ApJ, 306, 390
Vader, J. P., Frogel, J. A., Terndrup, D. M., & Heisler, C. A. 1993, AJ (in press) (Paper I)
Vader, J. P., & Simon, M. 1987, AJ, 94, 854
van den Bergh, S. 1980, PASP, 92, 122
Veron-Cetty, M. P., & Veron, P. 1988, A&A, 204, 28
Wikland, T., & Henkel, C. 1989, A&A, 225, 1
Williams, R. E., & Christiansen, W. A. 1985, ApJ, 291, 80
Wilson, A. S., & Willis, A. G. 1980, ApJ, 240, 429
Wolstencroft, R. D., Savage, A., Clowers, R. G., MacGillivray, H. T., Leggett, S. K., & Kalafi, M. 1986, MNRAS, 223, 279

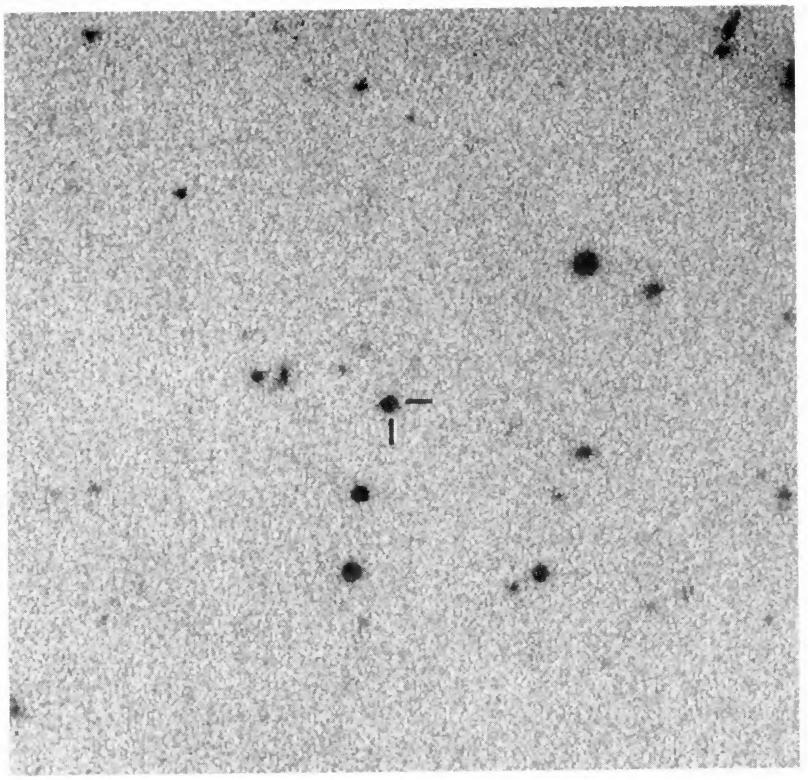

(a)

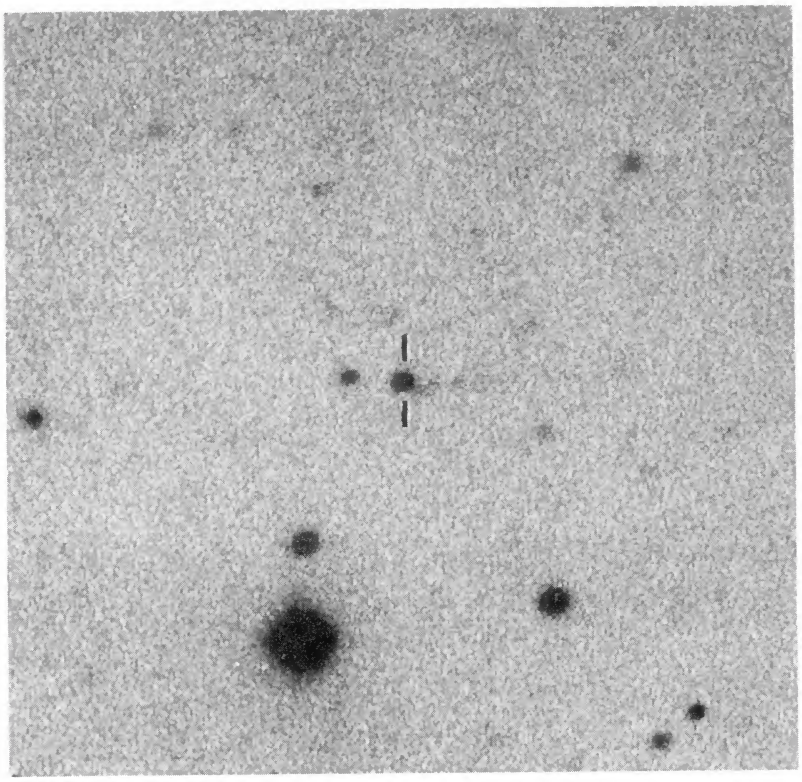

(b)

FIG. 4. (a) A 900 s Gunn-*r* exposure of BRI 1013+00 taken at the Palomar 60 in telescope on UT 1993 May 14. (b) A 900 s Johnson-*R* exposure of BRI 1050−00 taken at the Palomar 60 in telescope on UT 1993 April 22. Note the faint galaxies directly West of the quasar. Both images are 2 arcmin square with N up and E to the left.

Smith *et al.* (see page 26)

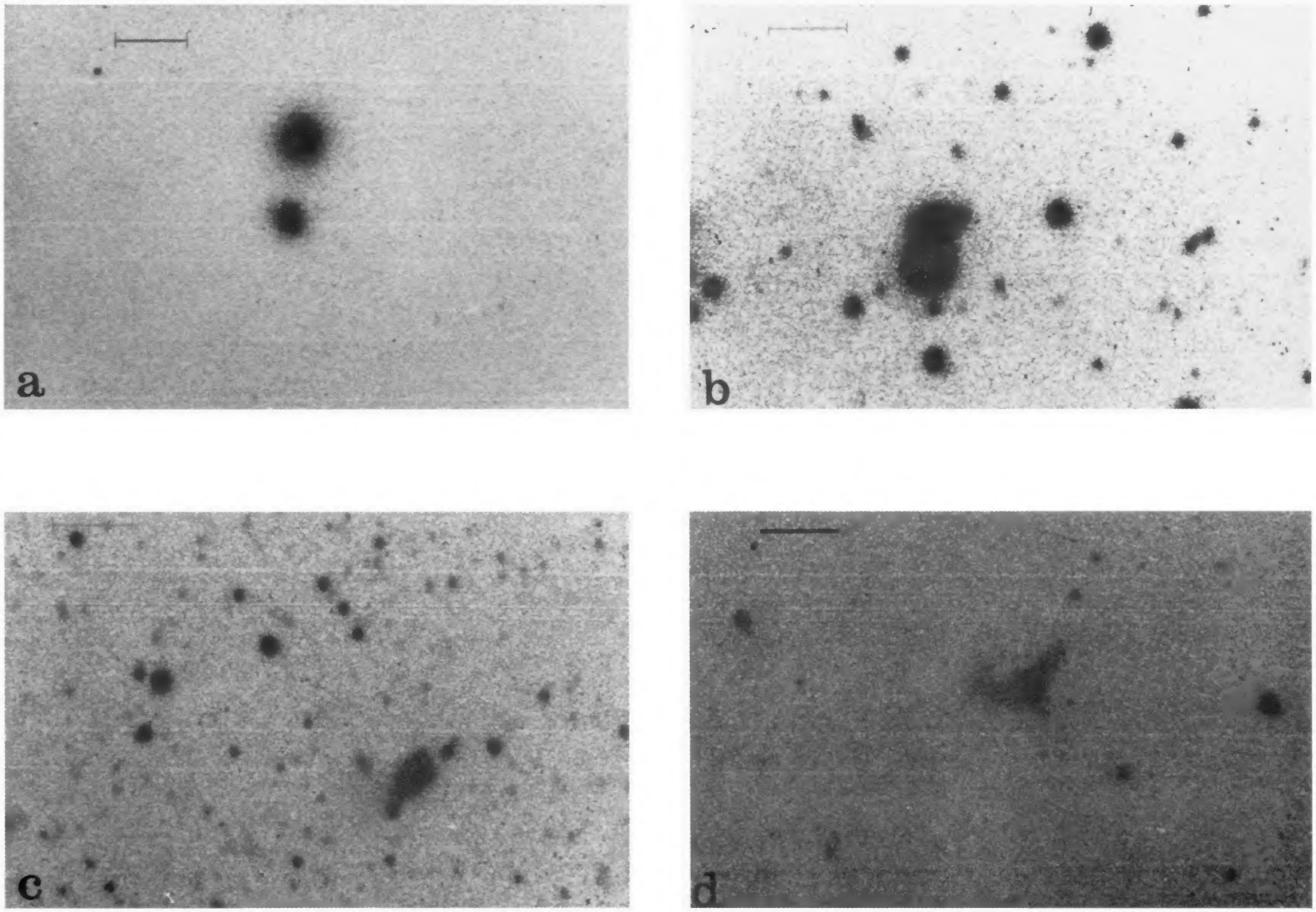

FIG. 1. CCD images of previously unidentified 60PKs. The length of the bar is 25 arcsec and it is located in the NE portion of the image. The *IRAS* name is listed followed by the exposure time (in seconds) and the filter through which the observation was made. (a) 00160-0719 300 s exposure in *B* filter; (b) 00198-7926 3600 s exposure in *B* filter; (c) 00521-7054 600 s exposure in *R* filter; (d) 00153+2147 1200 s exposure in *R* filter.

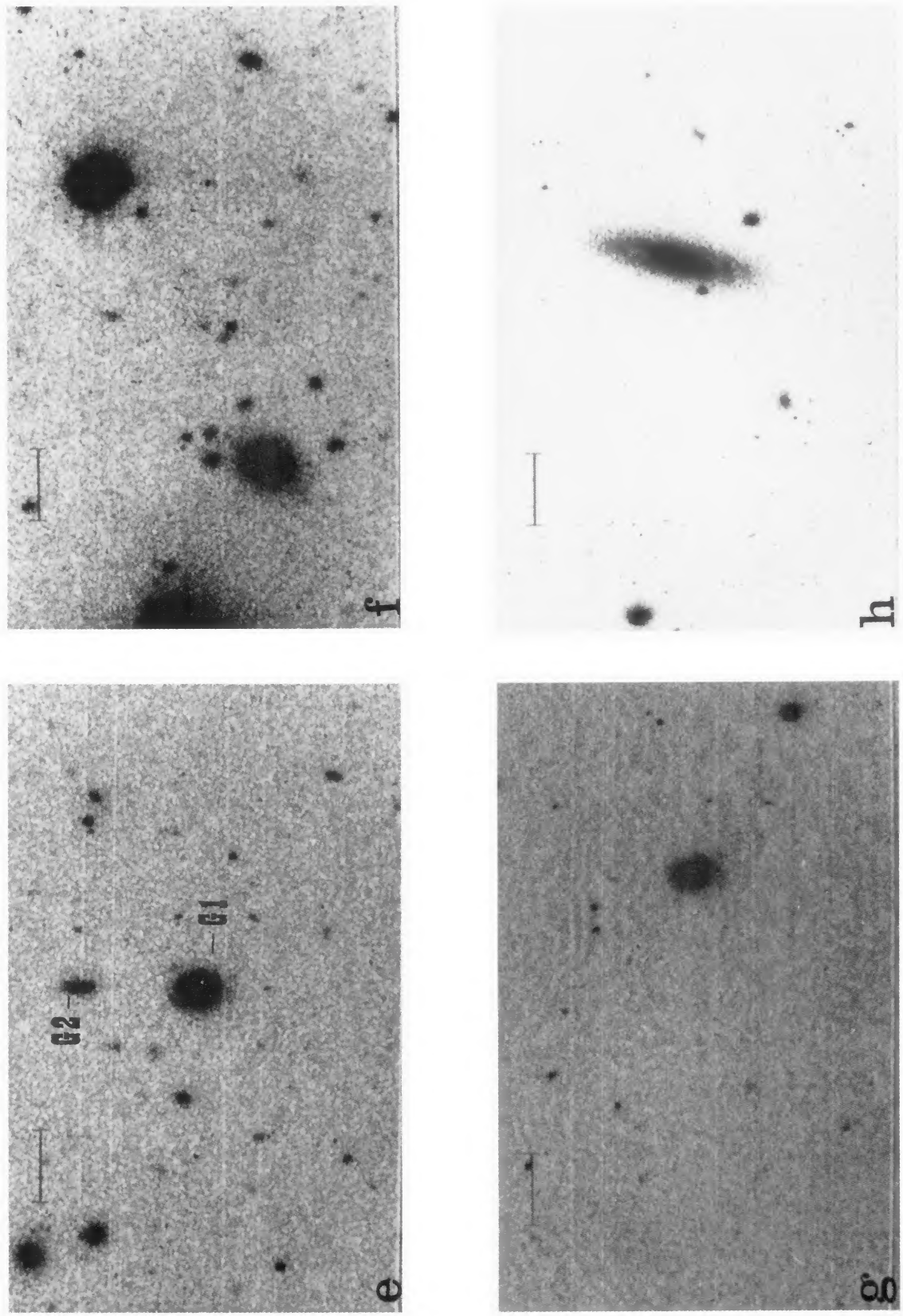

FIG. 1. (continued)

(e) 01072-0348 1800 s exposure in *B* filter; (f) 01475-0740 3600 s exposure in *B* filter; (g) 02530+0211 900 s exposure in *R* filter; (h) 03106-0254 900 s exposure in *B* filter.

C. A. Heisler and J. P. Vader (see page 37)

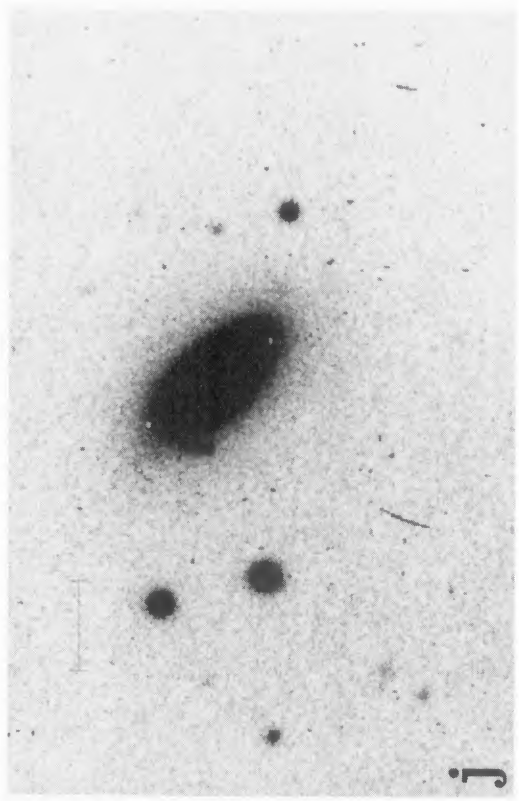

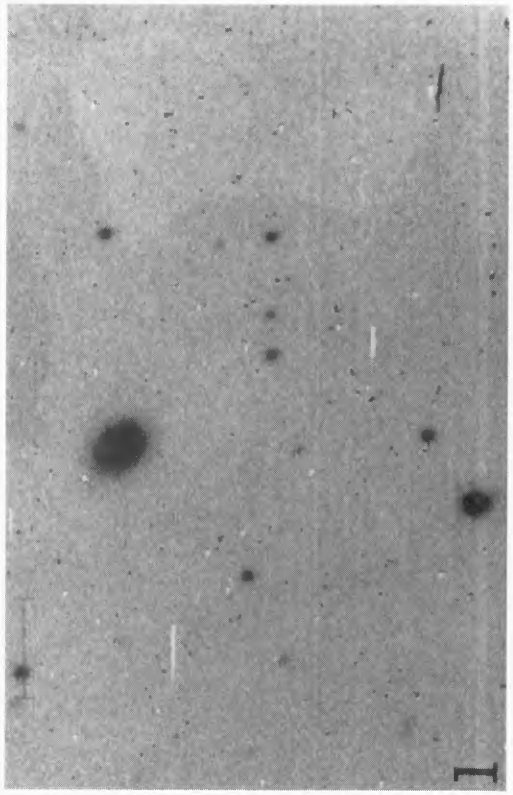

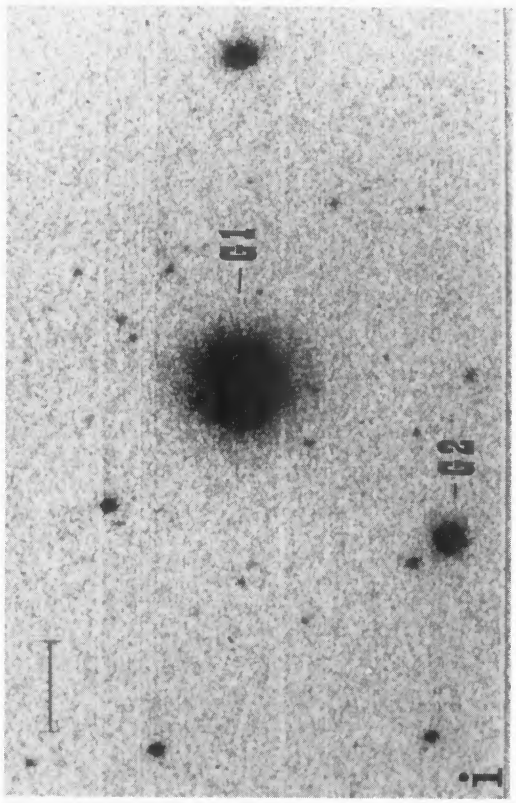

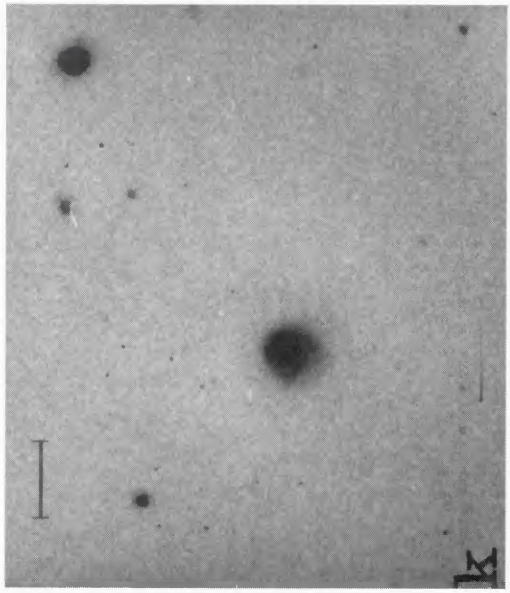

FIG. 1. (continued)

(i) 04259-0440 700 s exposure in *R* filter; (j) 04285-0828 3600 s exposure in *U* filter; (k) 05189-2524 300 s exposure in *B* filter; (l) 05570-8123 median of three 600 s exposures in *B* filter.

C. A. Heisler and J. P. Vader (see page 37)

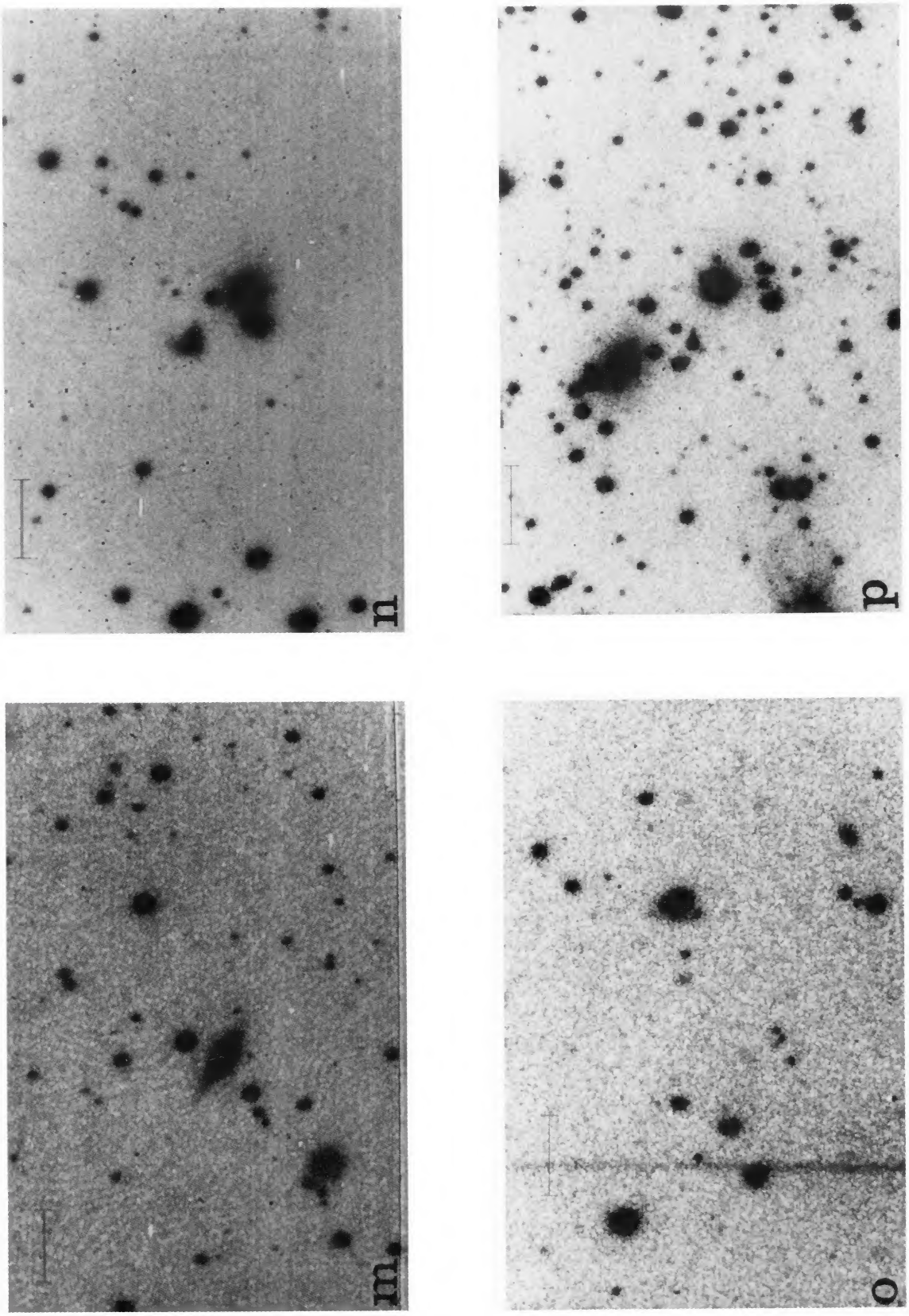

FIG. 1. (continued)

(m) 08007-6600 1200 s exposure in *R* filter; (n) 08170-1126 median of three 600 s exposures in *R* filter; (o) 10567-3323 1800 s exposure in *R* filter; (p) 14167-7236 median of three 600 s exposures in *R* filter.

C. A. Heisler and J. P. Vader (see page 37)

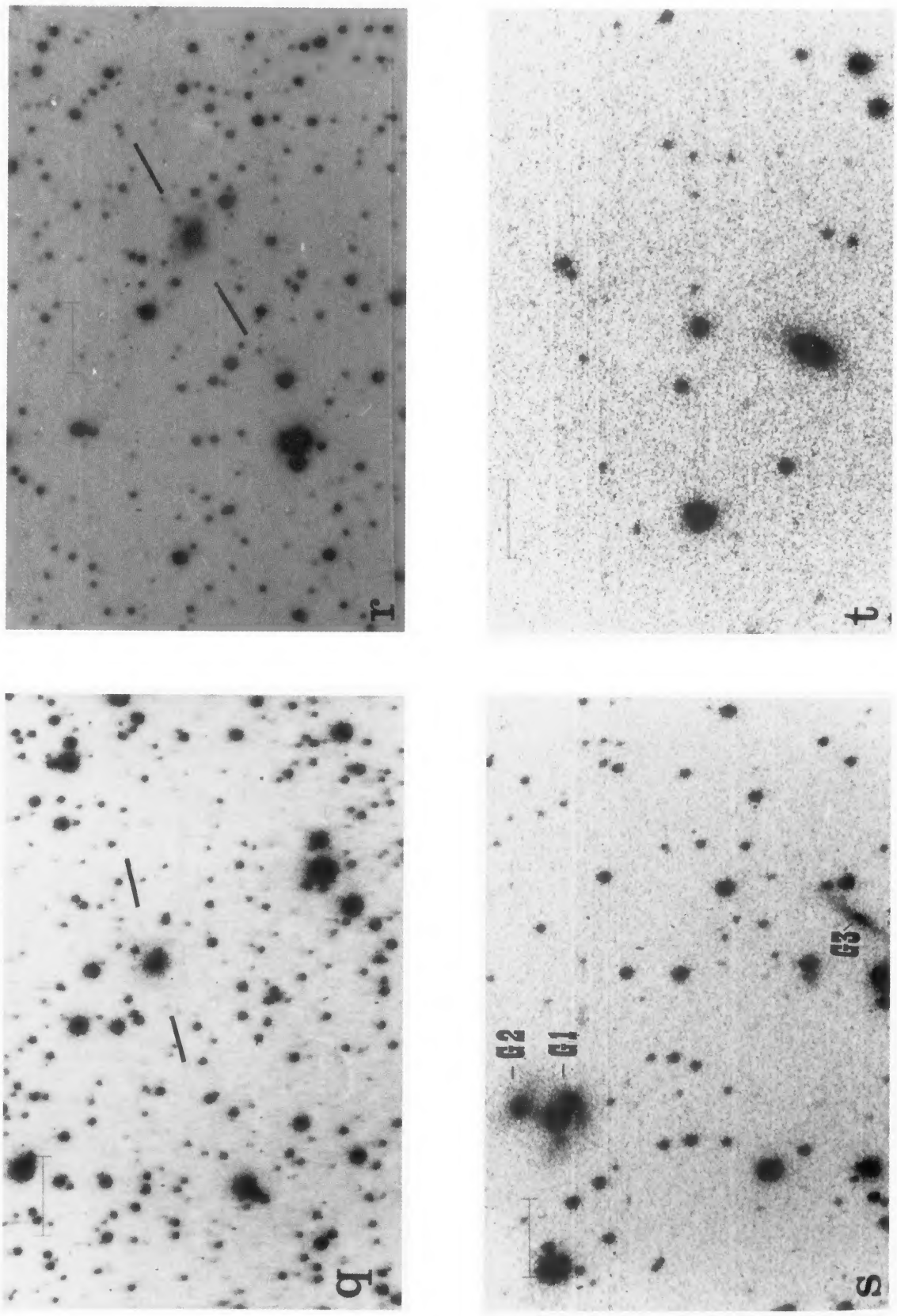

FIG. 1. (continued)

(q) 18526-7236 600 s exposure in *B* filter—not considered in analysis of this paper; (r) 19370-0131 2000 s exposure in *B* filter; (s) 20210+1121 median of three 300 s exposures in *R* filter; (t) 20253+1752 900 s exposure in *R* filter.

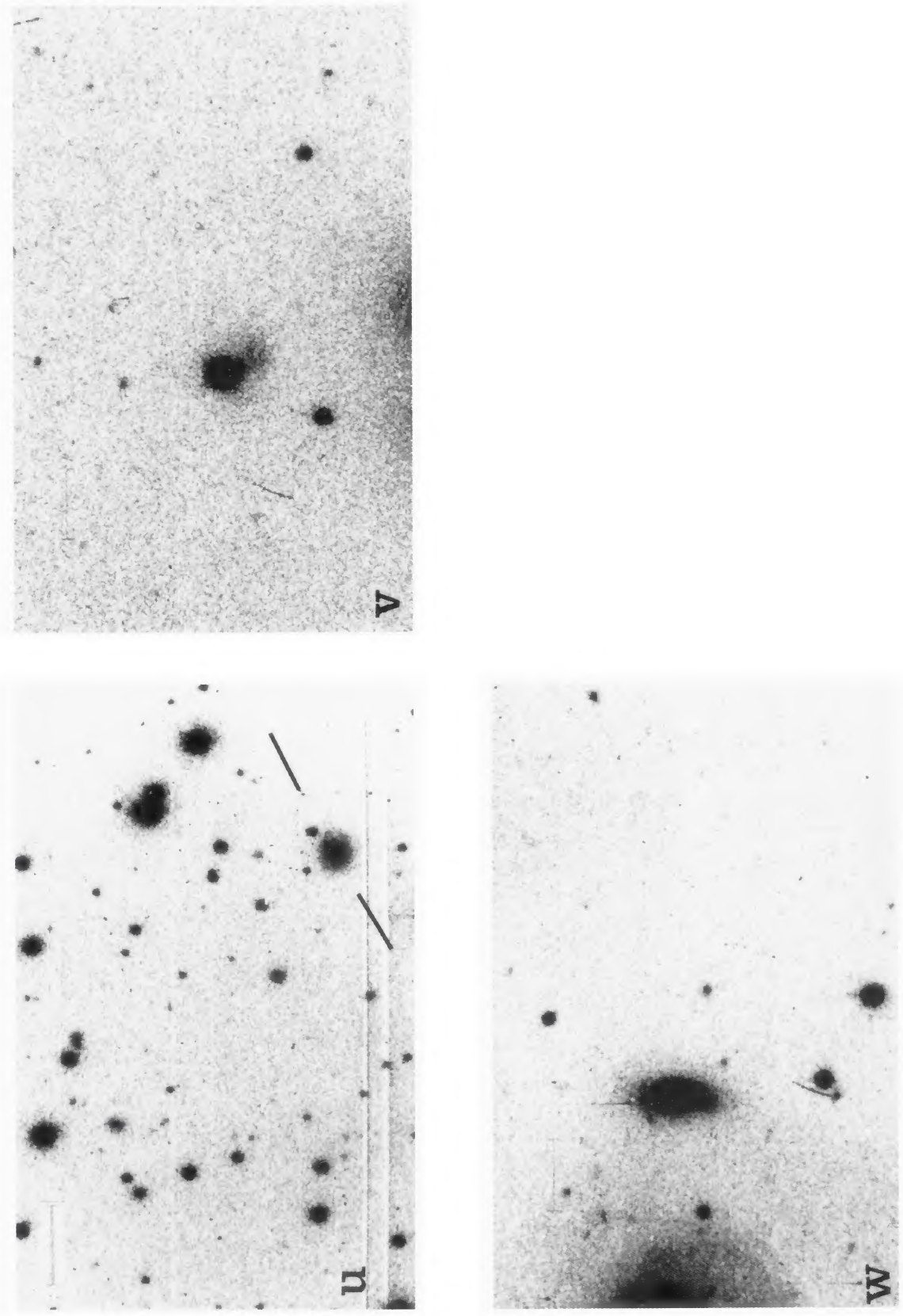

FIG. 1. (continued)

(u) 21062+1752 average of two 600 s exposures in *R* filter; (v) 23060+0505 600 s exposure in *V* filter; (w) 23547+1914 1200 s exposure in *B* filter.

C. A. Heisler and J. P. Vader (see page 37)

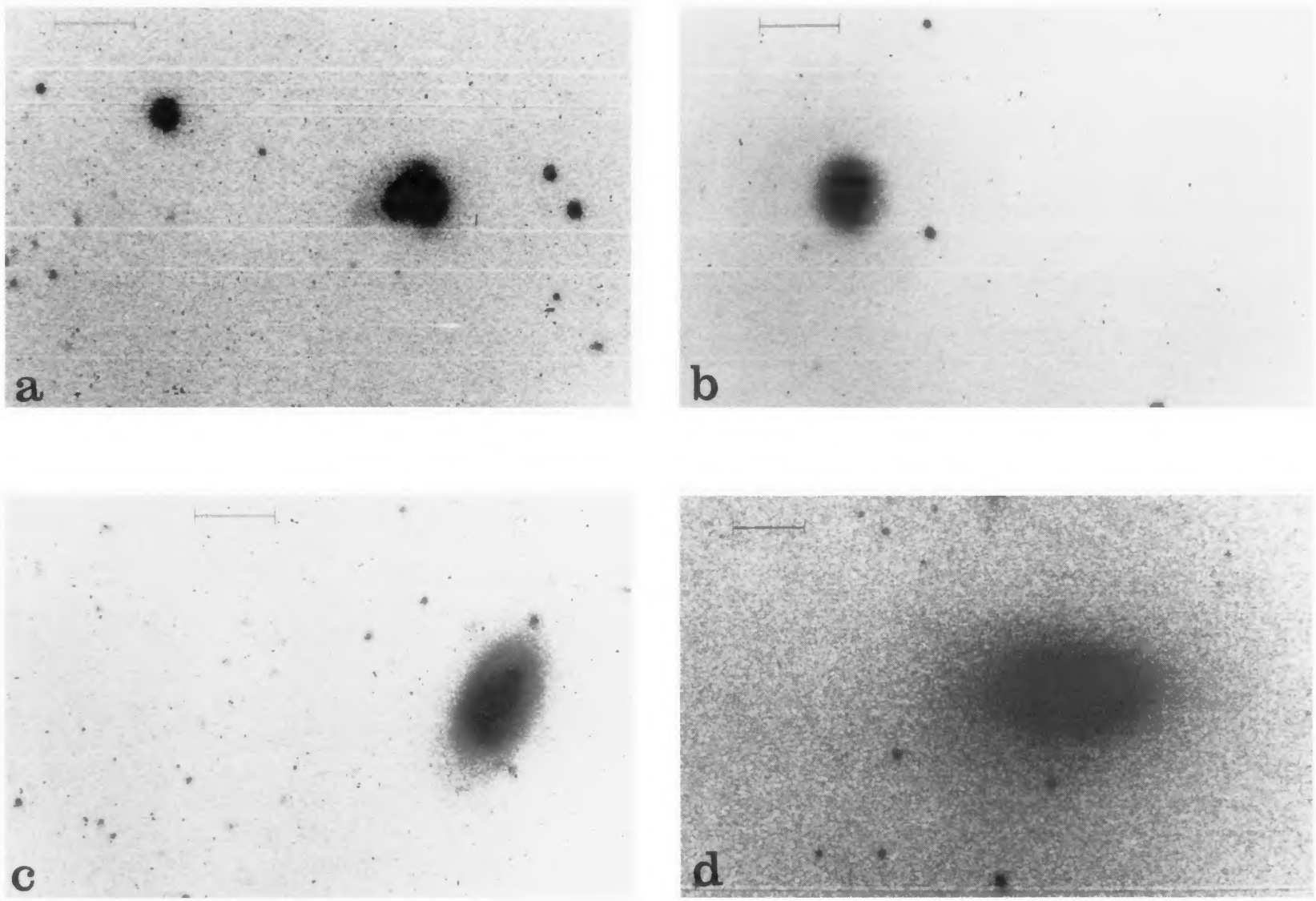

FIG. 2. CCD images of previously identified 60PKs. The length of the bar is 25 arcsec and it is located in the NE portion of the image. The *IRAS* name is listed together with its catalogue name, followed by the exposure time (in seconds) and the filter through which the observation. (a) 00344-3349/ESO 350-G38 median of three 600 s exposures in *B* filter; (b) 01413+0205/Mkn 573 median of three 240 s exposures in *R* filter; (c) 02304+0012/UGC 2024 1800 s exposure in *B* filter; (d) 03344-2103/NGC 1377 450 s exposure in *R* filter.

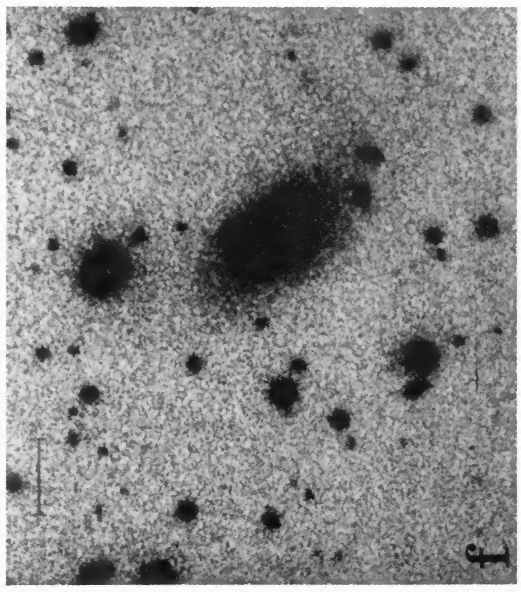

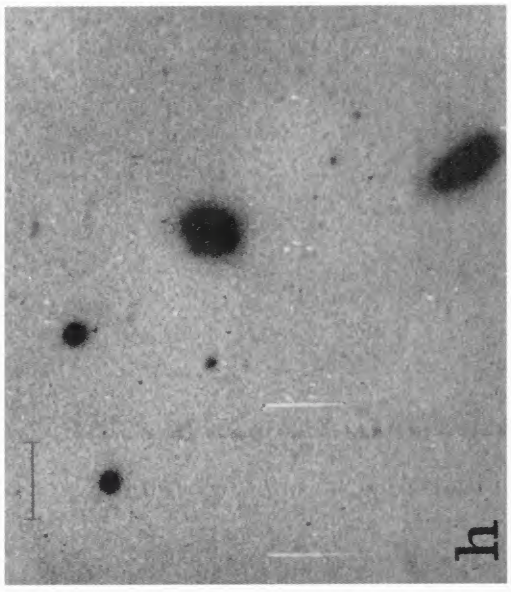

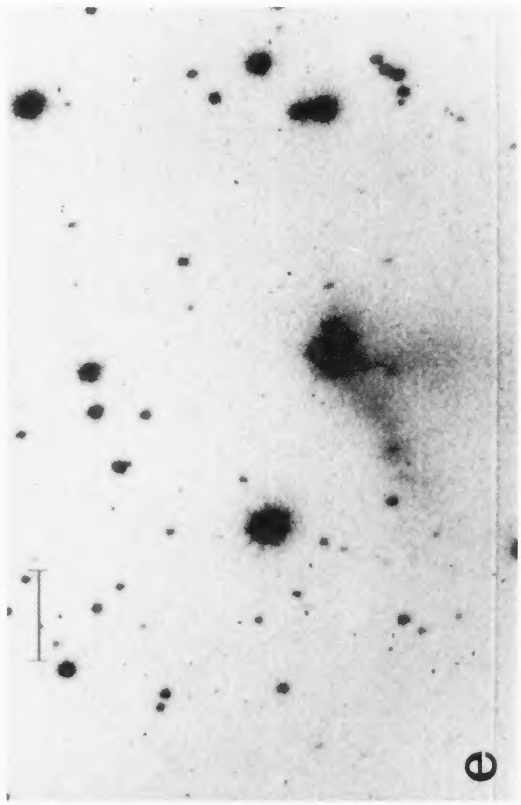

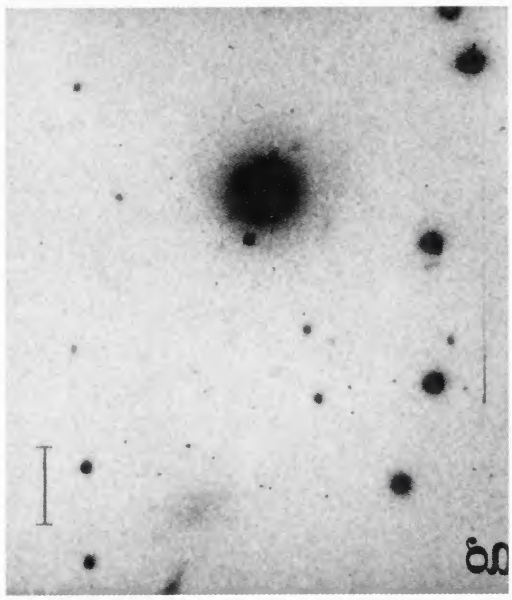

FIG. 2. (continued)
(e) 05530+0323/II Zw 40 600 s exposure in *R* filter; (f) 06488+2731/MCG+05-16-010 300 s exposure in *R* filter; (g) 08014+0515/Mkn 1210 450 s exposure in *B* filter; (h) 09497-0122/Mkn 1239 median of three 600 s exposures in *B* filter.

C. A. Heisler and J. P. Vader (see page 37)

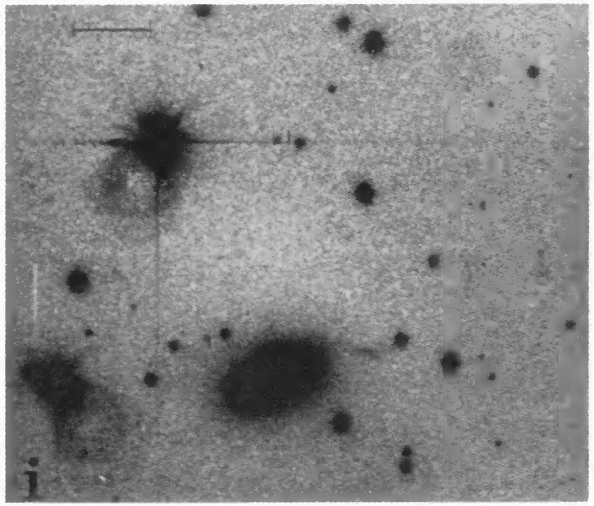

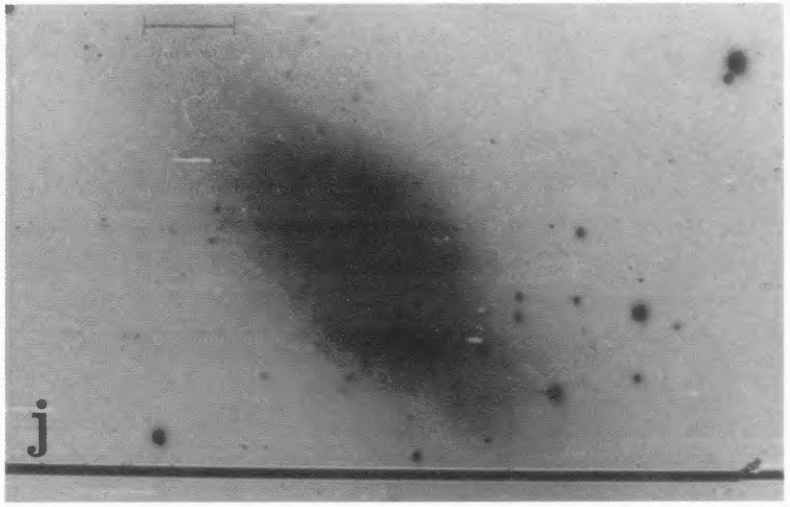

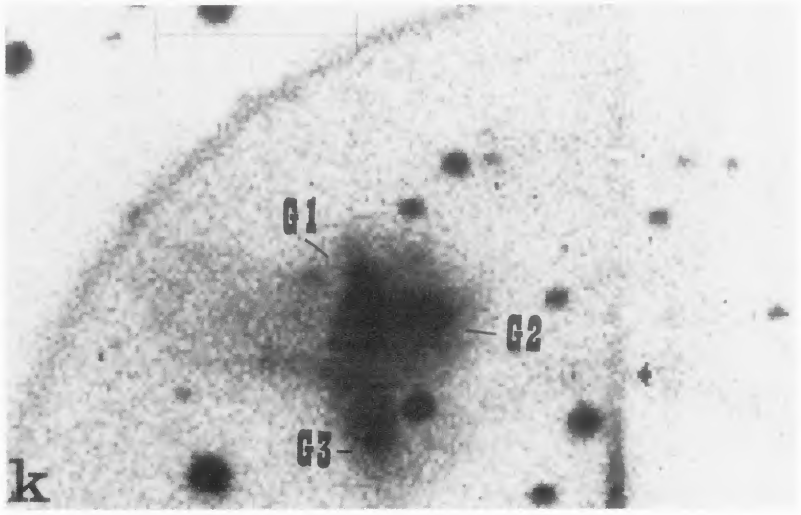

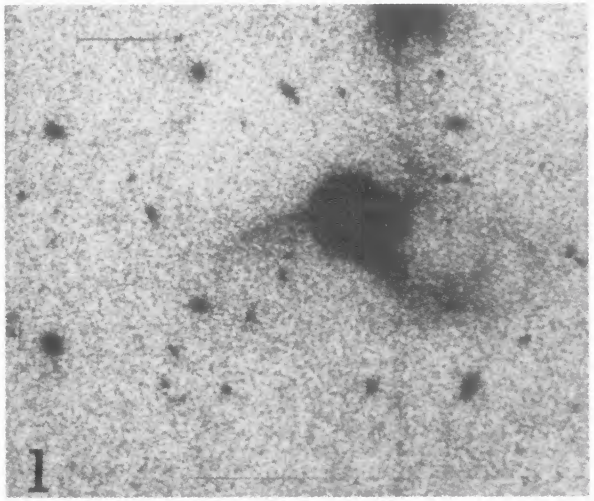

FIG. 2. (continued)

(i) 13329-3402/MCG-6-30-15/ESO 383-G35 median of three 240 s exposures in *R* filter; (j) 13370-3123/NCG 5253 median of three 180 s exposures in *R* filter; (k) 13452-4155/ESO 325-IG22 median of three 300 s exposures in *R* filter; (l) 13536+1836/Mkn 463 600 s exposure in *R* filter.

1994AJ....107...35H

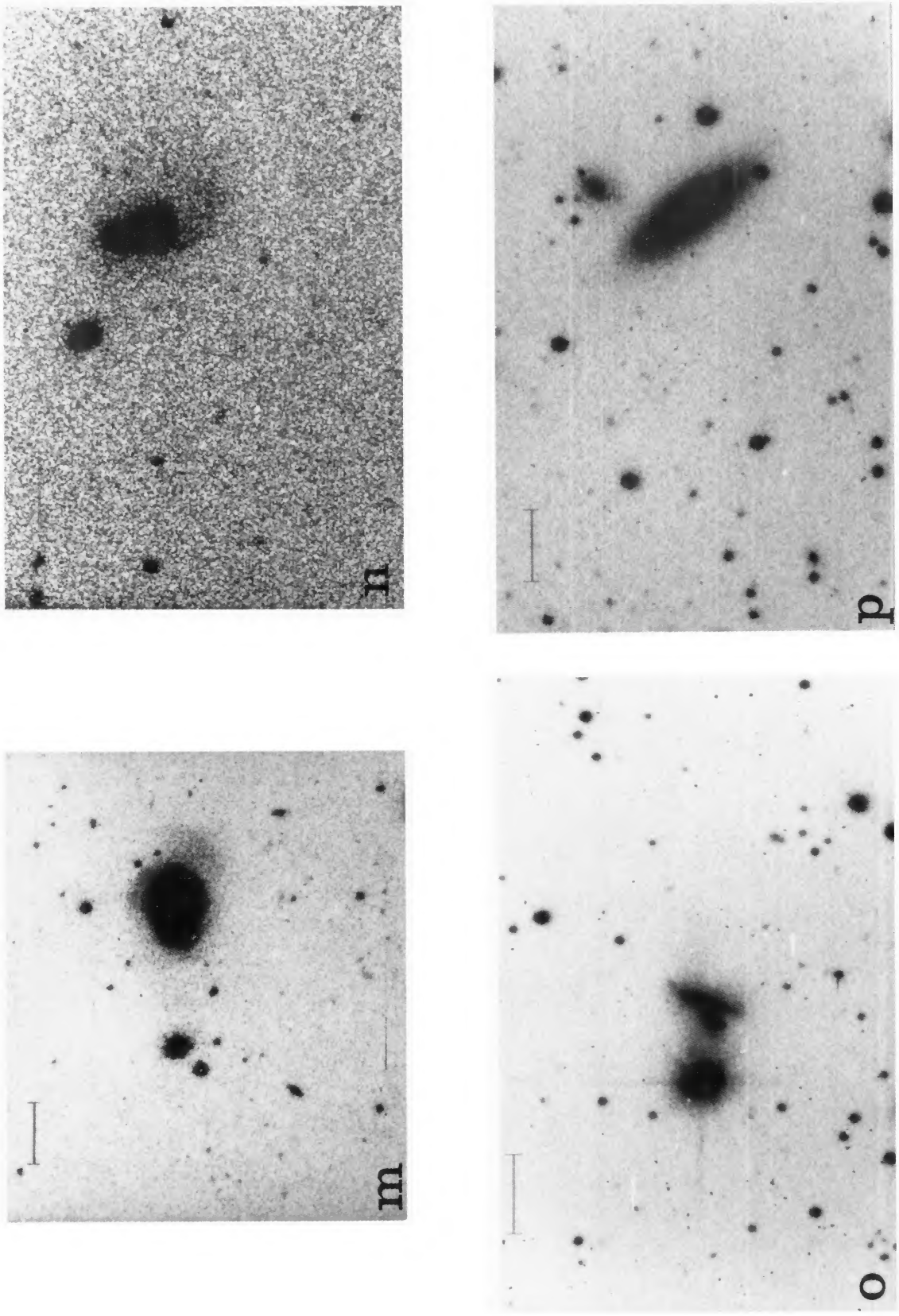

FIG. 2. (continued)

(m) 14082+1347/CGCG Zwicky 780 s exposure in *R* filter; (n) 15295+2414/3C 321 1200 s exposure in *B* filter; (o) 16380-8120/ESO 023-IG03 600 s exposure in *B* filter; (p) 18333-6528/ESO 103-G35 600 s exposure in *R* filter.

C. A. Heisler and J. P. Vader (see page 37)

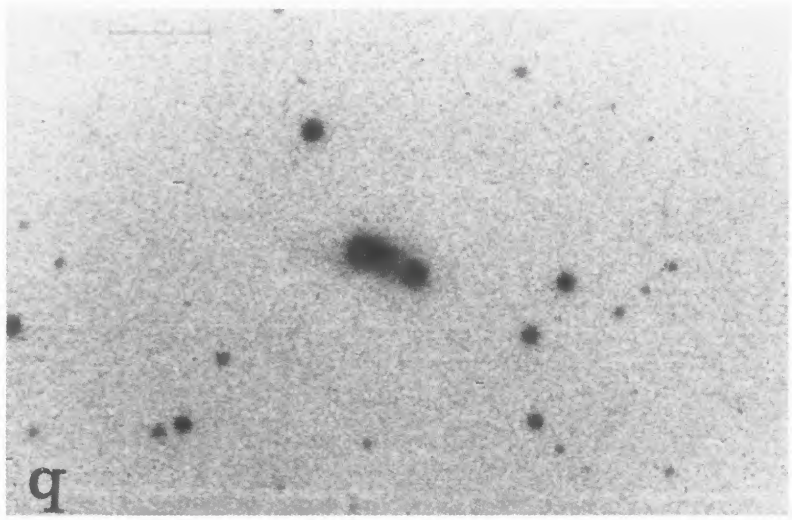

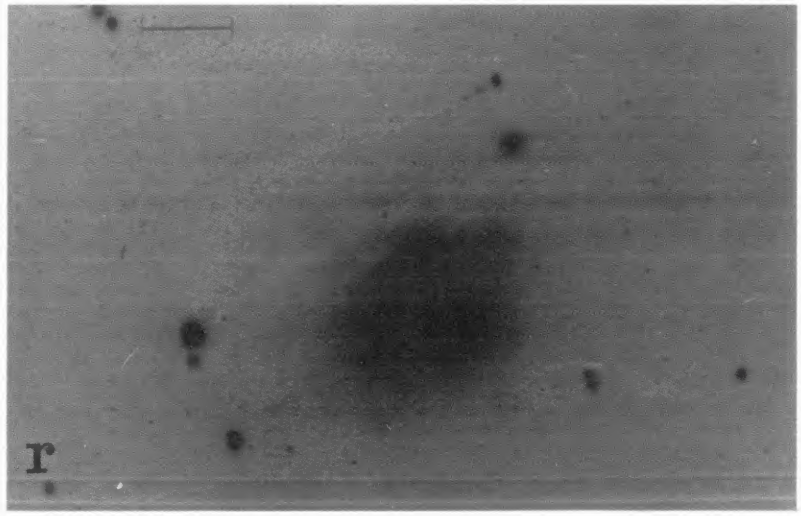

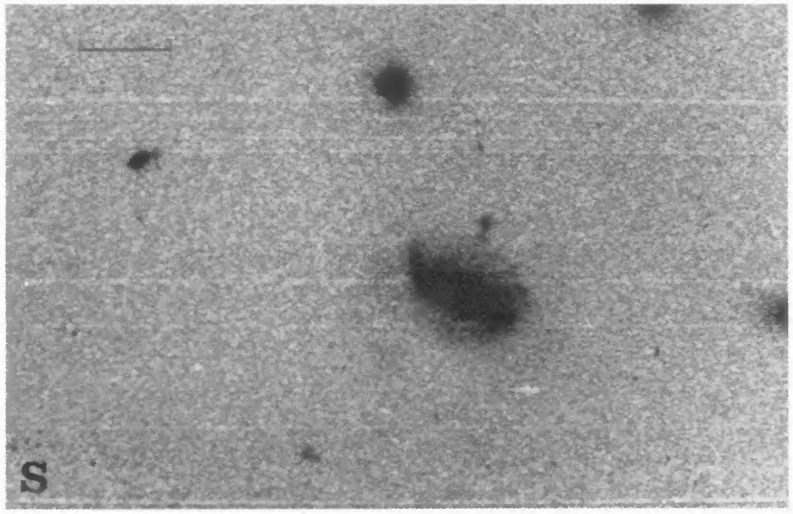

FIG. 2. (continued)

(q) 19245-4140/ESO 338-IG04/Tololo 19245 600 s exposure in *B* filter; (r) 20481-5715/IC 5063/PKS2048-57 median of three 300 s exposures in *R* filter; (s) 23446+1519/MCG+02-60-01 450 s exposure in *B* filter.

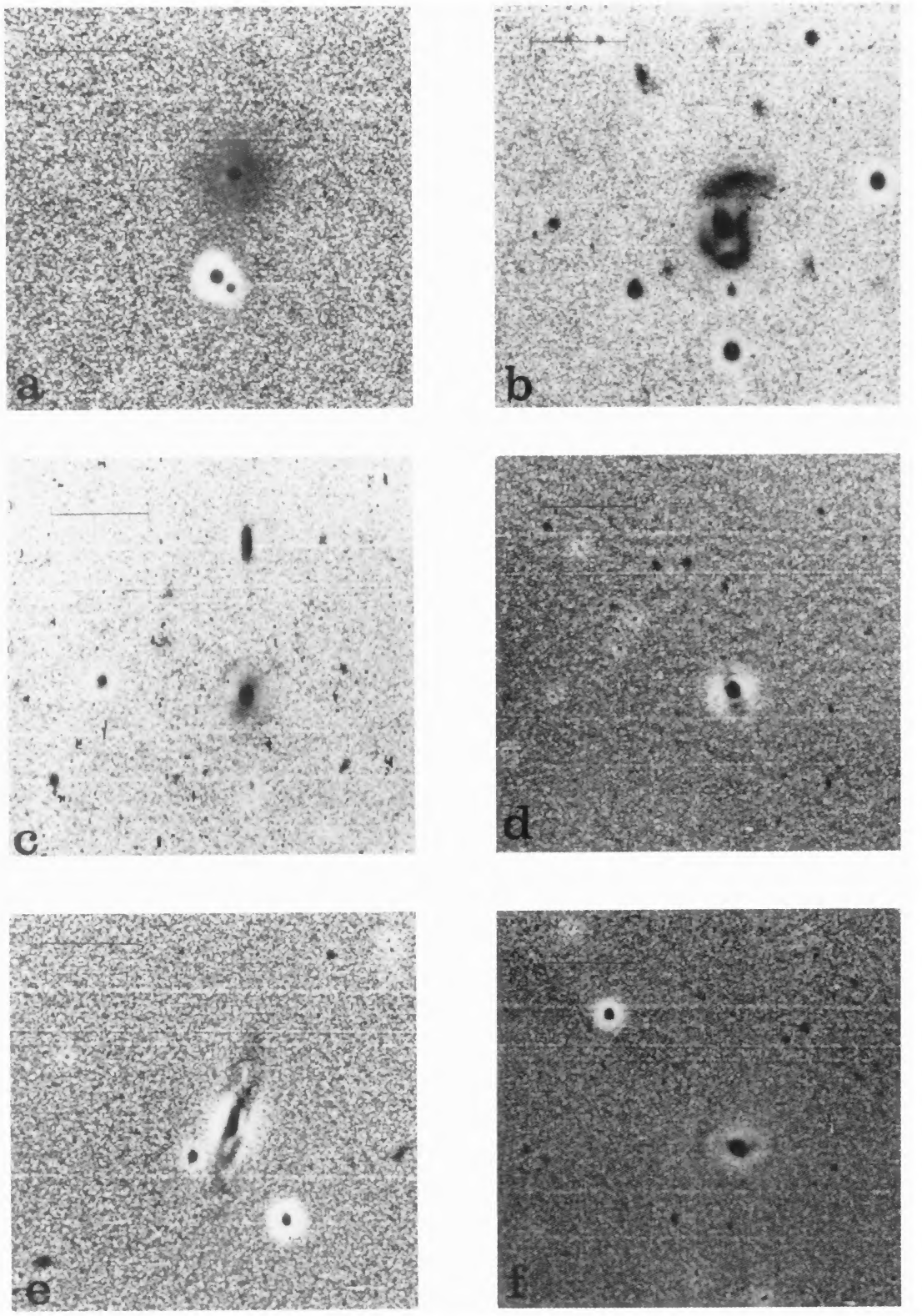

FIG. 3. Digitally enhanced CCD images of previously unidentified 60PKs. The length of the bar is 25 arcsec and it is located in the NE portion of the image. The *IRAS* name is listed followed by the type of digital enhancement used. (a) 00160-0719 $B-R$ color map revealing circumnuclear dust patches. (b) 00198-7926 $B-R$ color map revealing asymmetrical nucleus which is suggestive of a second nucleus, along with bright tidal tails. (c) 01072-0348 $B-R$ color map showing inner shells. (d) 02530+0211 Unsharp masked frame (900 s in R filter) reveals shells. (e) 03106-0254 Unsharp masked frame (900 s in B filter) displays central dust lane encircling nucleus. (f) 04259-0440 Unsharp masked frame (700 s in R filter) reveals shells.

C. A. Heisler and J. P. Vader (see page 39)

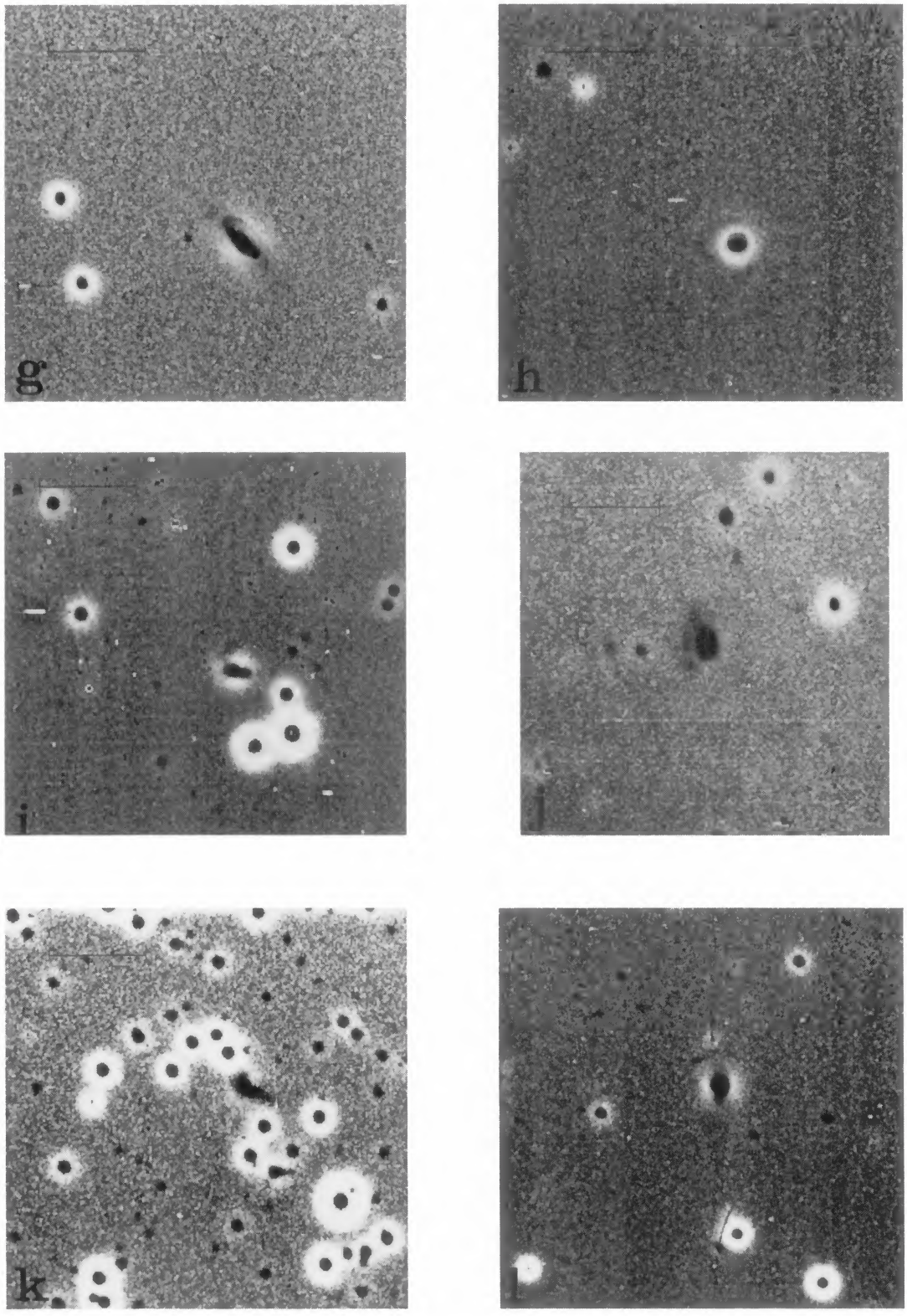

FIG. 3. (continued)

(g) 04385-0828 Unsharp masked frame (300 s in *V* filter) shows bright knots (presumably H II regions) and central arms or tidal features. (h) 05189-2524 Unsharp masked frame (300 s in *B* filter) reveals faint circular plumes surrounding galaxy. (i) 08170-1126 Unsharp masked frame (1200 s in *R* filter) displays two nuclei and a tail emanating from the brighter nucleus in the north direction. (j) 10567-3323 $B-I$ color map displays plume containing three bright knots east of the galaxy. (k) 14167-7236 Unsharp masked frame of a (1200 s in *B* filter) shows tidal tail feature in SW direction. (l) 23547-1914 Unsharp masked frame (1200 s in *B* filter) uncovers inner shells, and asymmetric nucleus which strongly suggests a second nucleus.

C. A. Heisler and J. P. Vader (see page 39)

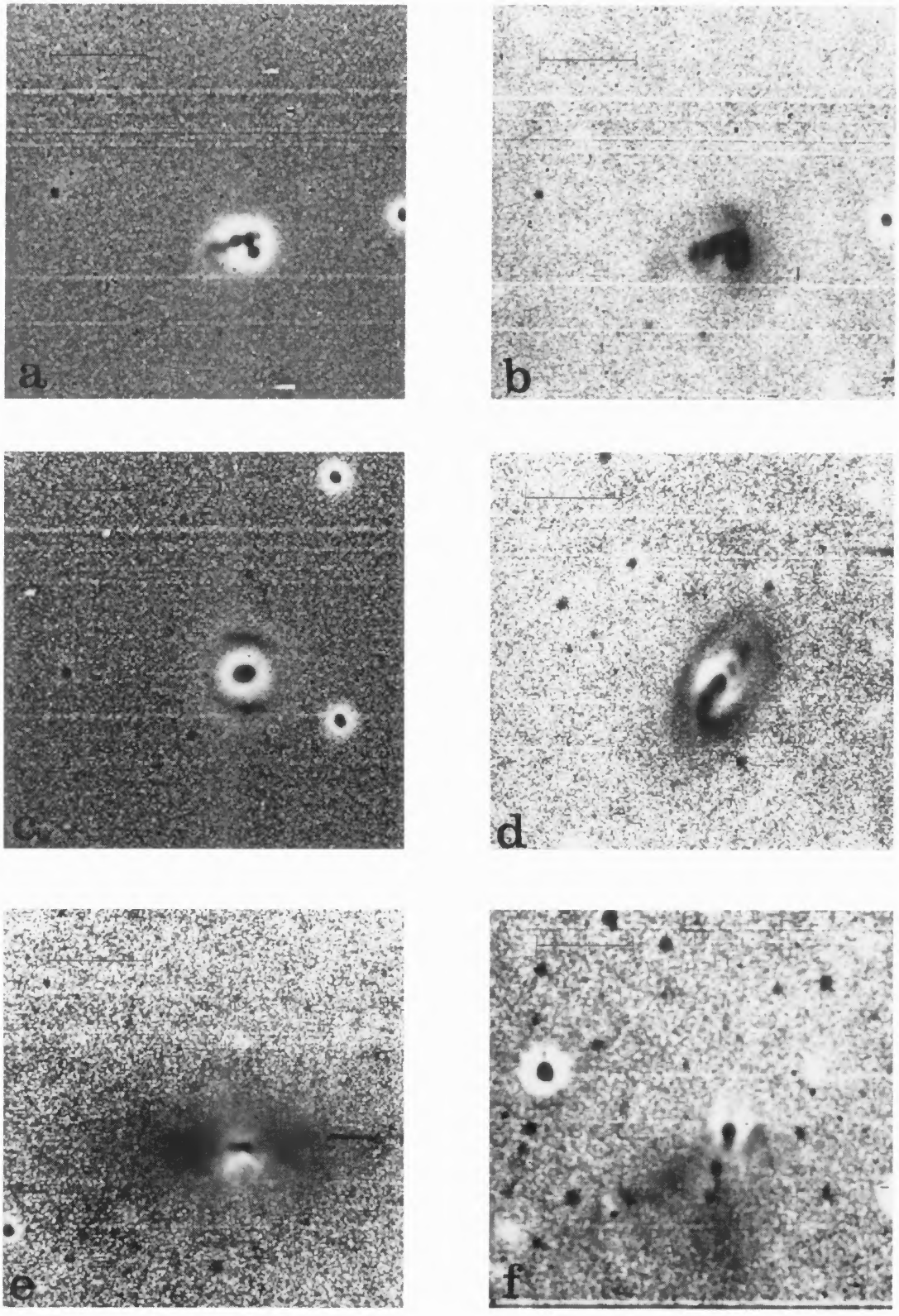

FIG. 4. Digitally enhanced CCD images of previously identified 60PKs. The length of the bar is 25 arcsec and it is located in the NE portion of the image. The *IRAS* name is listed together with its catalogue name, followed by the type of digital enhancement used. (a) 00344-3349 Unsharp masked frame (median of three 600 s in *B* filter) clearly shows three nuclei and a plume extending from the eastern nucleus in the SE direction. (b) 00344-3349 $B-I$ color map displays dust patches (white regions) and regions of enhanced star formation (relatively darker regions). (c) 01413+0205 Unsharp masked frame (median of three 240 s in *R* filter) clearly shows arcs with bright knots embedded in them. (d) 02304+0012 $B-R$ color map reveals bright knots (H II regions) at either side of the nucleus along the same line as the spiral arms. (e) 03344-2103 $B-I$ color map prominently displays central dust lane along the minor axis direction. (f) 05530-0323 $B-R$ color map shows dust and blue tidal tails are clearly visible. This digitally enhanced frame also reveals an asymmetry of the nucleus suggesting a possible second nucleus.

C. A. Heisler and J. P. Vader (see page 39)

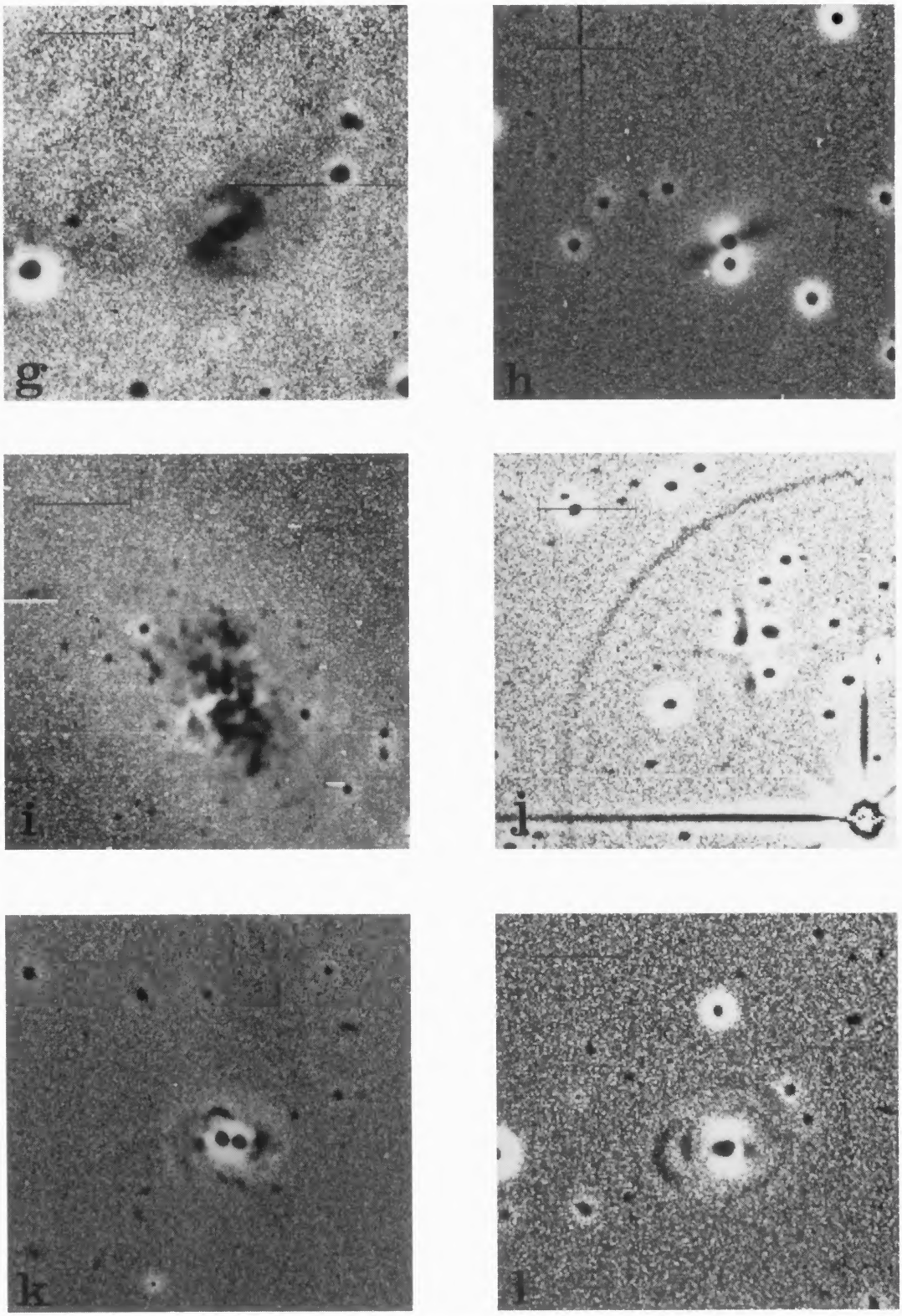

FIG. 4. (continued)

(g) 06488+2731 $B-I$ color map clearly reveals shells, tidal tails, and patches of dust. (h) 13329-3402 Unsharp masked frame of 600 s exposure in B filter uncovers disklike structure. (i) 13370-3123 $B-R$ color map clearly display numerous dust patches and bright central condensations believed to be H II regions. (j) 13452-4155 Unsharp masked frame (median of three 300 s in R filter) reveals tidal tail extending towards the north. (k) 13536+1836 Unsharp masked frame (600 s exposure in B filter). (l) 14082+1347 Unsharp masked frame (780 s exposure in R filter) clearly shows shell features.

C. A. Heisler and J. P. Vader (see page 39)

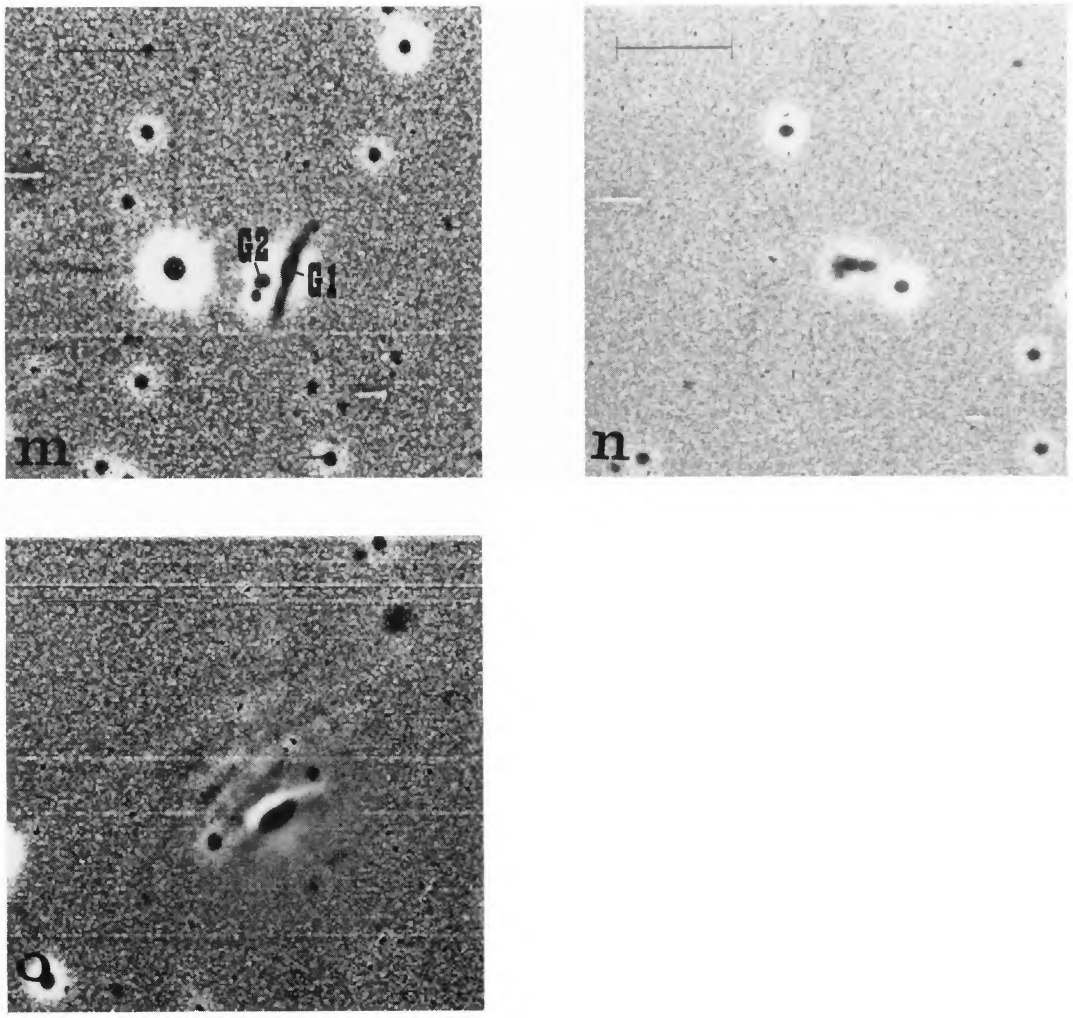

FIG. 4. (continued)

(m) 16380-8120 Unsharp masked frame (600 s exposure in *B* filter) shows that the northern portion of the disk is warped, while the small companion shows no features. (n) 19245-4140 Unsharp masked frame (median of three 500 s in *B* filter) clearly displays the second faint nucleus and a plume emanating from the brighter nucleus. (o) 20481-5715 Unsharp masked frame (median of three 600 s exposures in *B* filter) uncovers numerous dust lanes running parallel to the major axis of the galaxy.

C. A. Heisler and J. P. Vader (see page 39)

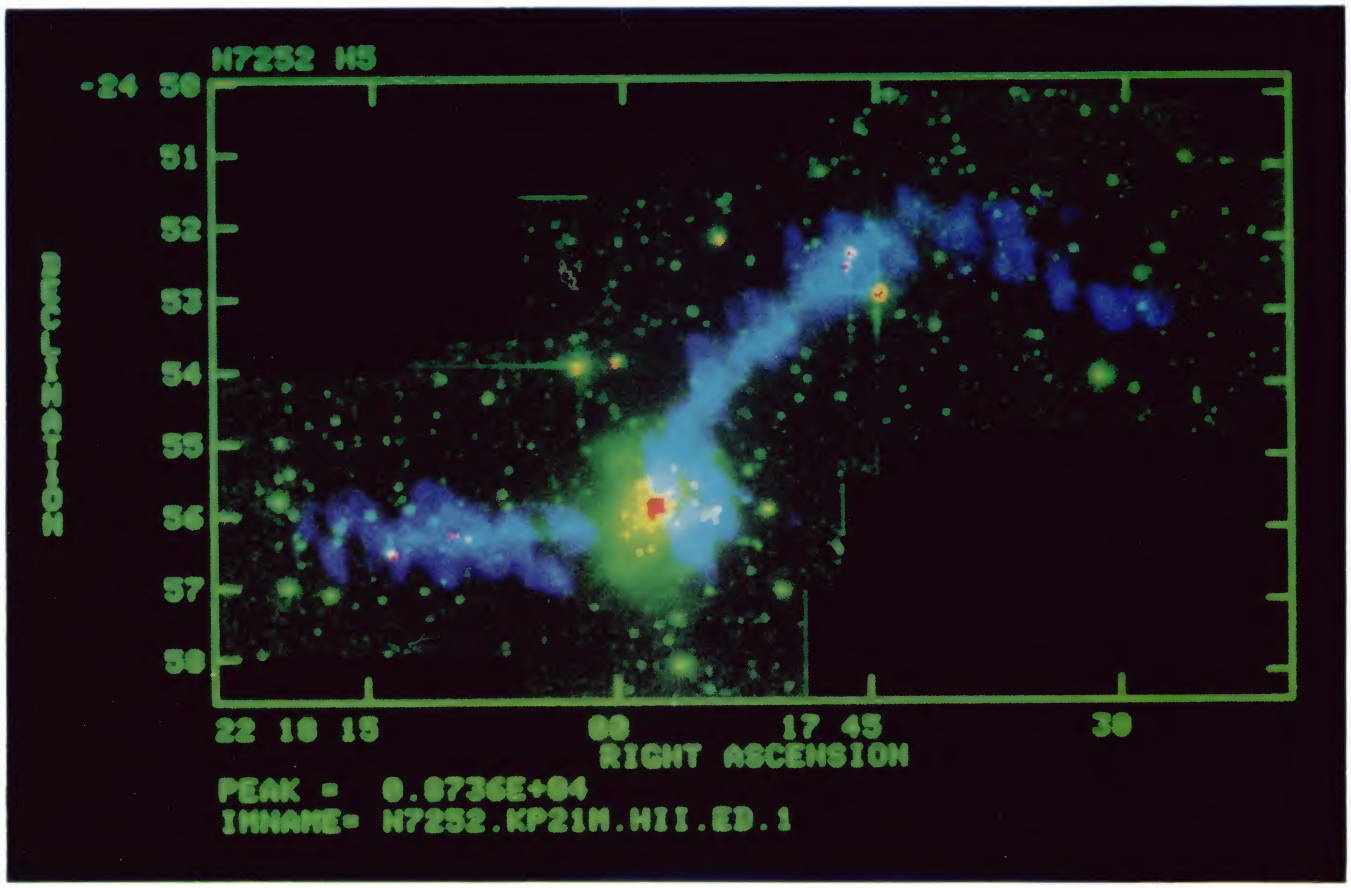

FIG. 1. False-color composite image of the late-stage merger NGC 7252 showing: the summed $B+R$ CCD mosaic image obtained using the CTIO 4 m (green); the VLA C+D map of the integrated H I emission (blue); and KPNO 2.1 m observations of the Hα line emission (red). The Hα data consist of three 4.'6×4.'6 CCD frames, one centered on the nucleus of NGC 7252 and one on the H II region in each of the two tidal tails. The line emission has been continuum-corrected using an R-band image and stars which are saturated on this CCD frame appear red in the color image. The H I is located almost entirely in the outer tidal regions and extends beyond the end of the optical tails, particularly in the northwest.

Hibbard *et al.* (see page 72)